Fortschritt-Berichte VDI

VDI

Reihe 3

Verfahrenstechnik

Dipl.-Ing. Bernhard Eckl,
Burghausen

Nr. 912

Development of Molecular Models of Real Fluids for Applications in Process Engineering

Fortschritt-Berichte VDI

Reihe 3

Verfahrenstechnik

Dipl.-Ing. Bernhard Eckl,
Burghausen

Nr. 912

Development of Molecular Models of Real Fluids for Applications in Process Engineering

VDI verlag

Eckl, Bernhard
Development of Molecular Models of Real Fluids for Applications in Process Engineering
Fortschr.-Ber. VDI Reihe 3 Nr. 912. Düsseldorf: VDI Verlag 2010.
152 Seiten, 61 Bilder, 15 Tabellen.
ISBN 978-3-18-391203-2, ISSN 0178-9503,
€ 49,00 / VDI-Mitgliederpreis € 44,10.

Keywords: Thermophysical properties – Molecular modeling – Molecular simulation – Quantum mechanics – Vapor-liquid equilibrium – Ethylene oxide – Mixture – Humid air – Hydrogel

Molecular modeling and simulation shows great promise for the prediction of a variety of thermophysical properties over wide ranges of state. The broad application to problems in process engineering is, however, hindered by the scarcity of reliable molecular models. In the present work, a method for the rapid development of accurate molecular models for real fluids is presented. It combines results from quantum mechanics and further optimization of the models to experimental vapor-liquid equilibrium data. This method is applied to develop 13 new molecular models. The excellent accuracy and outstanding predictive power of the models is presented in different applications, like in the calculation of 17 different fluid properties of ethylene oxide, of the vapor pressure of binary and ternary mixtures, or of the dew point of humid air. It is shown that the present molecular models predict the various thermophysical properties in general more reliably than standard methods, like equations of state. Finally, an outlook on the application of molecular modeling and simulation to hydrogels is given.

Bibliographische Information der Deutschen Bibliothek
Die Deutsche Bibliothek verzeichnet diese Publikation in der Deutschen Nationalbibliographie; detaillierte bibliographische Daten sind im Internet unter http://dnb.ddb.de abrufbar.

Bibliographic information published by the Deutsche Bibliothek
(German National Library)
The Deutsche Bibliothek lists this publication in the Deutsche Nationalbibliographie (German National Bibliography); detailed bibliographic data is available via Internet at http://dnb.ddb.de.

D 93

© VDI Verlag GmbH · Düsseldorf 2010

Alle Rechte, auch das des auszugsweisen Nachdruckes, der auszugsweisen oder vollständigen Wiedergabe (Fotokopie, Mikrokopie), der Speicherung in Datenverarbeitungsanlagen, im Internet und das der Übersetzung, vorbehalten.

Als Manuskript gedruckt. Printed in Germany.
ISSN 0178-9503
ISBN 978-3-18-391203-2

Vorwort

Die vorliegende Arbeit entstand in der Zeit von Oktober 2003 bis März 2008 während meiner Tätigkeit als wissenschaftlicher Mitarbeiter von Prof. Dr.-Ing. H. Hasse am Institut für Technische Thermodynamik und Thermische Verfahrenstechnik der Universität Stuttgart. Herr Prof. Dr.-Ing. H. Hasse hat die Arbeit angeregt und gemeinsam mit Herrn Prof. Dr.-Ing. J. Vrabec betreut. Herzlich danken möchte ich Herrn Prof. Dr.-Ing. H. Hasse für die sehr gute fachliche und persönliche Zusammenarbeit. Mit seinem wertvollen Rat in zahlreichen Diskussionen über wissenschaftliche Fragestellungen und seiner engagierten Förderung in allen Phasen dieser Arbeit trug er entscheidend zu deren Gelingen bei. Überdies ermöglichte er es, durch den hohen wissenschaftlichen Anspruch einerseits und die großen persönlichen Freiheiten andererseits ein für die Erstellung dieser Arbeit sehr motivierendes Umfeld zu schaffen.

Herr Prof. Dr.-Ing. J. Vrabec leitete mit großem Engagement die Arbeitsgruppe Molekulare Simulation am Institut. Mein aufrichtiger Dank gilt ihm für seine tägliche Diskussionsbereitschaft, die den Austausch von Fachwissen ermöglichte, der für das Gelingen der vorliegenden Arbeit unverzichtbar war. Daneben schuf er durch seine Art ein kreatives Umfeld, aus dem viele neue Ideen zum Fortgang dieser Arbeit entstanden.

Herrn Prof. Dr. rer. nat. M. Resch danke ich für die freundliche Übernahme des Koreferats und die kritische Durchsicht der Ergebnisse.

Der Deutschen Forschungsgemeinschaft danke ich für die finanzielle Förderung dieser Arbeit im Rahmen des Schwerpunktprogramms 1155 "Molekulare Modellierung und Simulation für Anwendungen in der Verfahrenstechnik". Neben der finanziellen Förderung ermöglichte das Schwerpunktprogramm auch einen intensiven Austausch mit Forschern anderer Universitäten. Weiterhin danke ich dem Höchstleistungsrechenzentrum der Universität Stuttgart (HLRS) und dem Rechenzentrum der Technischen Universität Karlsruhe für die sehr gute Zusammenarbeit. Große Teile dieser Arbeit wurden auf dem Bundeshöchstleistungsrechner NEC SX-8 und den Landeshöchstleistungsrechnern XC4000 und XC6000 durchgeführt.

Darüber hinaus möchte ich mich bei allen Studentinnen und Studenten bedanken, die mit ihrer Begeisterung und ihrem Engagement als Diplom- und Studienarbeiter oder als wissenschaftliche Hilfskräfte zu der vorliegenden Arbeit beitrugen. Namentlich sollen hier Inga Utz, Sandhyarani Sahoo, Yahia Derbali, Stefan Deublein, Christian Schauz,

Hendrik Frentrup und Christian Berreth genannt werden.

Bei allen Kolleginnen und Kollegen am Institut bedanke ich mich herzlich für die freundschaftliche Atmosphäre und den guten, über den Arbeitstag hinausgehenden Zusammenhalt. Auch durch die wöchentliche "Joggingrunde" bleibt die Zeit in Stuttgart in guter Erinnerung. Stellvertretend möchte ich hier Jadran Vrabec, Thorsten Schnabel, Oliver Ryll, Sebastian Hoch, Frank Schaal und Ralf Notz nennen.

Mein besonderer Dank gilt nicht zuletzt meiner Frau und meiner Tochter, die mich während der Anfertigung dieser Arbeit in jeder Hinsicht unterstützten.

Burghausen, im Januar 2010 Bernhard Eckl

Contents

List of Symbols

Latin Letters

A	arbitrary macroscopic property
$\mathcal{A}$	arbitrary microscopic property
c	concentration
c_p	isobaric heat capacity
c_v	isochoric heat capacity
C	constant
e	electronic charge: $e = 1.6021 \cdot 10^{-19}$ C
f_W	vapor pressure enhancement factor
F	Helmholtz energy
$\mathcal{F}$	fitness function
g_W	vapor concentration enhancement factor
G	Gibbs enthalpy
h	enthalpy
Δh_v	enthalpy of vaporization
$\mathcal{H}$	microscopic Hamiltonian
k_B	Boltzmann constant: $k_\mathrm{B} = 1.3806 \cdot 10^{-23}$ J K^{-1}
l	distance
m	model parameter, mass
N	number of molecules
p	pressure
P_acc	probability of acceptance
q	partial charge
Q	partition function, quadrupole momentum
r_{ij}	intermolecular center of mass distance
r_{ijab}	intermolecular site-site distance
T	temperature
t	time
u	internal energy
U	intermolecular interaction energy
V	(macroscopic) volume

$\mathcal{V}$	microscopic volume
w	weighting factor
x	liquid phase mole fraction
y	gas phase mole fraction
Z	compressibility factor

Greek Letters

β	Boltzmann factor
β_T	isothermal compressibility
γ	state point, surface tension
ϵ	Lennard-Jones energy parameter
ε_0	permittivity of vacuum: $\varepsilon_0 = 8.8541 \cdot 10^{-12}$ $C^2J^{-1}m^{-1}$
η	shear viscosity
θ	inclination angle
λ	thermal conductivity
μ	dipole momentum
μ_i	chemical potential of component i
ξ	binary interaction parameter
π	fluctuating particle
ρ	density
σ	Lennard-Jones size parameter
τ	integration time
ϕ	azimuthal angle
ψ	potential energy of test or fluctuating particle

Vector and Tensor Properties

$\boldsymbol{I}$	angular momentum of inertia tensor
$\boldsymbol{J}$	microscopic stress tensor, heat flow vector
$\boldsymbol{M}$	model parameter vector
$\boldsymbol{v}$	velocity vector
$\boldsymbol{w}$	angular velocity vector
$\boldsymbol{\Gamma}$	phase space, torque vector
$\boldsymbol{\omega}$	orientation vector

Subscripts and Superscripts

c	critical
ens	ensemble average
exp	experimental data
i	related to molecule or component i
id	ideal
l	liquid
res	residual
sim	simulation data
test	test particle
time	time average
σ	saturation
$'$	property of the saturated liquid phase
$''$	property of the saturated vapor phase

Abbreviations / Chemical Formulae

CH	methine group
CH_2	methylene group
CH_3	methyl group
DFT	density functional theory
EOS	equation of state
LJ	Lennard-Jones
MC	Monte Carlo
MD	molecular dynamics
NIPAM	poly-n-isopropyl acrylamide
PAA	polyacryl amide
Prob	probability
PVA	polyvinyl alcohol
QM	quantum mechanics
VLE	vapor-liquid equilibrium

Abstract

One of the major challenges in thermodynamics is the quantitative description and prediction of thermophysical properties for industrial applications. Particularly in energy and process engineering, the thermophysical properties are the basis for the development of new techniques and the optimization of existing plants. As an experimental determination of all required data may often be very expensive and time consuming, a theoretical description is of particular significance.

Molecular modeling and simulation provides a promising approach to modeling of thermophysical properties. This method describes the interactions at the molecular level by a so-called molecular model. Molecular simulation then is used to calculate the desired thermophysical properties from the molecular interactions. With this approach, it is possible to consistently describe the behavior of pure substances and mixtures over a wide range of states on a sound physical basis.

In the present work, the capabilities of molecular modeling and simulation for applications in process engineering are demonstrated. In addition to a good description of experimental fluid behavior, the method shows an outstanding predictive power, which is presented for various examples.

The further application of molecular modeling and simulation is still restricted by the scarcity of molecular models, which are optimized for a quantitative prediction of thermophysical properties. Thus, a modeling strategy is developed in the present work, which allows a rapid parametrization of new molecular models. This strategy uses results from quantum mechanical *ab initio* calculations to significantly reduce the number of free model parameters. The modeling effort is perceptibly reduced by a direct transfer of the location of model sites and electrostatic interaction parameters from quantum mechanics. A set of few, here two to four, parameters is subsequently optimized to experimental pure vapor-liquid equilibrium data.

With the presented strategy, a total of 13 new molecular models of pure substances is developed. The molecular models are optimized to experimental data on vapor pressure, saturated liquid density, and enthalpy of vaporization along the whole range of the vapor-liquid equilibrium. In most cases, a very good representation of the experimental data is reached, and in all cases, a significant improvement is achieved compared to molecular models from the literature.

These models are used subsequently to demonstrate the predictive capability of molecular modeling and simulation. Very good predictions are found for pure substance properties like second virial coefficient, structural quantities, thermal, caloric, and transport properties, as well as thermophysical properties of mixtures.

Ammonia is well investigated experimentally due to its technical importance. Besides macroscopic properties over a wide range of states, experimental results on structural properties are available. Thus, radial distribution functions from molecular simulation are compared to experimental data from neutron diffraction. Although the molecular model is solely optimized to vapor-liquid equilibrium properties, an excellent agreement is found.

Taking ethylene oxide as an example, a total of 17 different pure substance properties are determined. Thermal properties are predicted among caloric properties, transport properties, and surface tension with satisfactory accuracies by molecular modeling and simulation.

A substancial part of technical processes deals with mixtures. In the present work, the applicability of molecular modeling and simulation on the prediction of mixture properties is demonstrated on two examples. For the binary mixture R227ea + ethanol, the special phase behaviour is predicted very well from pure substance properties without further adjustments.

Furthermore, an application on the multi-component system humid air is presented. The dew point of humid air is an important technical property for new processes like compressed air storage. In the present work, a new method is developed for the determination of the dew point from molecular simulations. The results agree very well with recent experimental data and reproduce the real fluid behaviour.

Finally, an outlook on the application of molecular modeling and simulation to hydrogels is given. Hydrogels are polymer networks, which can strongly swell or shrink in solvents dependent on external properties. In the present work, the focus is laid on the qualitative description of this swelling or shrinking process by molecular simulation. The applicability of the method is demonstrated as a starting point for further work towards a quantitative description.

Kurzfassung

Eine der großen Herausforderungen in der Thermodynamik ist die quantitative Beschreibung und Vorhersage von Stoffdaten für industrielle Anwendungen. Besonders in der Energie- und Verfahrenstechnik bilden die thermophysikalischen Stoffdaten die Grundlage für die Entwicklung neuer Verfahren und die Optimierung bestehender Anlagen. Da eine experimentelle Bestimmung der benötigten Stoffdaten teilweise sehr aufwändig ist, kommt einer theoretischen Beschreibung besondere Bedeutung zu.

Einen viel versprechenden Ansatz zur Modellierung von thermophysikalischen Stoffdaten stellt die molekulare Modellierung und Simulation dar. Dabei werden die Wechselwirkungen auf molekulare Ebene durch so genannte molekulare Modelle abgebildet. In der molekularen Simulation können dann die gewünschten thermophysikalischen Eigenschaften aus den molekularen Wechselwirkungen berechnet werden. Mit diesem Ansatz gelingt es auf Grund der exzellenten physikalischen Basis, das Verhalten von Reinstoffen oder Mischungen mit nur wenigen Parametern über einen weiten Zustandsbereich hinweg konsistent zu beschreiben.

In der vorliegenden Arbeit werden die Möglichkeiten eines Einsatzes der molekularen Modellierung und Simulation für Anwendungen in der Verfahrenstechnik aufgezeigt. Neben einer guten Beschreibung des experimentellen Stoffverhaltens ist dabei vor allem die hervorragende Vorhersagekraft der Methode hervorzuheben, wie sie an verschiedenen Beispielen präsentiert wird.

Eingeschränkt wird der weitergehende anwendungsorientierte Einsatz der molekularen Modellierung und Simulation bislang durch die nur begrenzte Anzahl an verfügbaren molekularen Modellen, die für die quantitative Bestimmung von Stoffdaten optimiert wurden. In der vorliegenden Arbeit wird daher eine Strategie entwickelt, die eine beschleunigte Parametrierung neuer molekularer Modelle erlaubt. Diese Strategie nutzt Ergebnisse aus quantenmechanischen *ab initio* Rechnungen um die Anzahl der freien Modellparameter stark zu reduzieren. Durch die direkte Übernahme der räumlichen Anordnung der Wechselwirkungszentren des molekularen Modells und der elektrostatischen Wechselwirkungsparameter aus der Quantenmechanik wird der Modellierungsaufwand deutlich reduziert. Eine weitere Optimierung des Modells erfolgt dann noch durch Anpassung weniger, hier zwei bis vier, Parameter an experimentelle Reinstoffdaten zum Dampf-Flüssigkeits Gleichgewicht.

Die vorgestellte Strategie wird genutzt um molekulare Modelle von insgesamt 13 Reinstoffen zu erstellen: iso-Butan, Cyclohexan, Formaldehyd, Dimethylether, Schwefeldioxid, Dimethylsulfid, Thiophen, Blausäure, Acetonitril, Ammoniak, Ethylenoxid und Heptaflourpentan. Die Modelle werden an experimentelle Werte von Dampfdruck, Siededichte und Verdampfungsenthalpie über den gesamten Temperaturbereich des Dampf-Flüssigkeits Gleichgewichts angepasst. Dabei wird meist eine sehr gute Beschreibung der experimentellen Daten, in allen Fällen aber eine deutliche Verbesserung bisheriger Modelle aus der Literatur erreicht.

Ein Vorteil der molekularen Modellierung und Simulation ist die herausragende Vorhersagekraft. Diese wird in der vorliegenden Arbeit an verschiedenen Beispielen aufgezeigt, unter anderen hinsichtlich des 2. Virialkoeffizienten B.

Ammoniak ist auf Grund seiner technischen Bedeutung experimentell sehr gut untersucht. Neben den makroskopischen Eigenschaften über weite Zustandsbereiche existieren hier auch Messungen zu Strukturgrößen. In Kapitel 4.2.1 werden radiale Paarverteilungsfunktionen aus der molekularen Simulation mit Daten aus Neutronenstreuexperimenten verglichen. Obwohl das molekulare Modell nur an Phasengleichgewichtsdaten angepasst wurde, liegt hier eine hervorragende Übereinstimmung vor.

Am Beispiel Ethylenoxid werden ausgehend von einer ausschließlichen Anpassung an das Phasengleichgewicht insgesamt 17 verschiedene Reinstoffeigenschaften berechnet. Neben thermischen Zustandsgrößen können mit der molekularen Modellierung und Simulation auch kalorische Größen, Transportgrößen und die Oberflächenspannung mit guten Genauigkeiten vorhergesagt werden.

Ein Großteil verfahrenstechnischer Prozesse beinhaltet Mischungen. An zwei Beispielen wird in dieser Arbeit die Anwendung der molekularen Modellierung und Simulation zur Vorhersage von Mischungseigenschaften aufgezeigt. Für die binäre Mischung Ethanol + R227ea kann das für ein Binärsystem spezielle Phasenverhalten sehr gut allein aus Reinstoffeigenschaften ohne weitere Anpassung vorhergesagt werden.

Weiterhin wird eine Anwendung auf das Mehrkomponentensystem feuchte Luft präsentiert. Eine wichtige technische Größe für neue Prozesse wie Druckluftspeicher ist der Taupunkt komprimierter feuchter Luft. In der vorliegenden Arbeit wird eine Methode zur Bestimmung des Taupunkts aus molekularen Simulationen entwickelt. Die Ergebnisse zeigen eine sehr gute Übereinstimmung mit aktuellen experimentellen Daten und geben das Realverhalten des Systems gut wieder.

Abschließend wird ein Ausblick auf die molekulare Modellierung und Simulation von Hydrogelen gegeben. Hydrogele sind makromolekulare Polymernetzwerke, die abhängig von äußeren Eigenschaften in Lösungsmitteln stark quellen bzw. schrumpfen können. Dabei wird kurz die Vorgehensweise bei der Modellierung der Makromoleküle aufgezeigt.

Weiter wird die Simulationsmethodik erläutert und erste Ergebnisse zur Simulation des Quell- bzw. Schrumpfvorgangs präsentiert. Das experimentelle Verhalten kann hier bisher nur qualitativ nachgestellt werden. Um eine quantitative Beschreibung zu erreichen, wären weitergehende Optimierungen des molekularen Modells nötig, die jedoch den Rahmen dieser Arbeit sprengen würden.

Zusammenfassend liefert die molekulare Modellierung und Simulation einen konsistenten Ansatz zur Korrelation und Vorhersage von thermophysikalischen Daten mit technisch relevanter Genauigkeit.

1 Introduction

Modern process engineering predominantly relies on a theoretical description of the regarded processes. In new industrial applications, this allows faster development cycles and reduced costs by skipping expensive experimental investigations. To handle this task, reliable theoretical models of the underlying processes, which are often governed by thermodynamics, are needed.

Molecular modeling and simulation allows to tackle issues in process engineering, for which classical phenomenological methods only give insufficient or even no answers. In addition to efficient simulation methods, excellent models of the intermolecular interactions of industrially relevant substances must be provided to yield quantitative statements with a desired accuracy. At a comparable number of parameters, these molecular models often reproduce the behavior of real substances much more realistically than phenomenological methods. Thus, a prediction of thermophysical data by molecular simulation is feasible. Another advantage of molecular modeling and simulation is its transferability to different applications as shown for some examples below.

1.1 Current Scientific State

In the literature, a broad variety of molecular models is available. A brief overview is given by [120, 186]. However, in many cases, the necessary accuracy for technical application is not reached. Furthermore, the molecular models are often incompatible with each other as they use different intermolecular potential types or combination rules, which disencourages their application to mixtures. Until today, the development of molecular models is mostly based on *ad hoc* assumptions and is thus very time-consuming. An important task in this field is a systematization and development of methods to short-cut the modeling effort to achieve an adequate time frame for industrial applications.

Using quantum mechanical (QM) methods, it is nowadays possible to calculate properties of almost arbitrary molecules *ab initio* with high accuracy and without the need of experimental data [51, 170]. Using the Born-Oppenheimer approximation, an energetically optimized molecular geometry can be determined with moderate effort by Hartree-Fock (HF) or density functional theory (DFT) methods. On top of this op-

timized geometry, electron density distributions can be calculated using methods like Møller-Plesset (MP) or Coupled-Cluster (CC) that account for electron-electron correlations. The electron density distribution, in combination with the positively charged nuclei, determine the electrostatic properties of a molecule. A simulation of molecule dimers in different configurations with respect to each other allows the determination of intermolecular pair interaction energies, i.e. dispersive and repulsive interactions as well as mutual polarization. Here, very sophisticated QM calculations are necessary to adequately describe these interactions, which are often weaker than the intramolecular interactions by several orders of magnitude. In the literature, mostly CC methods with large basis sets or an extrapolation to the basis set limit are used to achieve such accuracies, cf. [7]. It was found that also MP approaches yield acceptable results in numerous cases with a lower computational effort [205].

A direct method for calculating thermophysical properties from QM simulations was proposed by Car and Parinello [14]. Here, a molecular dynamics (MD) simulation is combined with a determination of the intermolecular forces by means of QM. Due to the extremely high computational effort, this method will not be accessible for engineering applications in the near future [203].

Approximating the intermolecular interactions to be used in molecular simulation by molecular models, also known as force fields, is computationally much more efficient. From these models, the desired macroscopic or microscopic thermophysical properties are determined in molecular simulation, e.g. by MD or by Monte-Carlo (MC) methods [3, 50, 167].

Different approaches exist for molecular modeling, which result in models with different levels of detail. The range reaches from molecular models that exclusively base upon QM calculations to models that are exclusively parametrized using phenomenological or experimental data:

Molecular models from QM calculations. The aim of this approach is to model the intermolecular (and sometimes intramolecular) interactions without recourse to any experimental thermophysical data. Typically, QM simulations are performed on monomers in vacuum and on dimers in different configurations [78]. The resulting interaction energy hyper surface is subsequently correlated by empirical functions so that a mathematical description of the interactions is available for molecular simulation [193]. Applying this procedure, an acceptable accuracy can be obtained with an adequate effort for noble gases or simple molecules [7, 72, 136, 195, 209, 210]. Due to the high level of detail, an application of the resulting models in molecular simulation, e.g. to determine the phase coexistence, is relatively expensive. Furthermore, sufficiently exact QM calculations are presently not feasible for more complex molecules with a reasonable computational ef-

fort. For the modeling of mixtures, the same work must be done again for the unlike dimer and for the re-correlation of the intermolecular interaction as this was done for the pure components [194]. An alternative to modeling strictly on the basis of *ab initio* is the transfer of QM results in the parametrization of semi-empirical potential functions, as discussed in more detail below.

Semi-empirical molecular models. Semi-empirical potential models are significantly more simplified compared to QM models (model reduction). Generally, only the substantial interaction contributions are considered explicitly. Due to a consistent separation of the interaction contributions, these models provide the opportunity of systematization of the development in new molecular models for pure substances. Mixtures can be modeled easily based on such pure substance models [189, 211, 220].

The interaction contributions, i.e. repulsion, dispersion, (static) polarities, and hydrogen bonding, are modeled separately using suitable potential functions, whose superposition yield the full intermolecular interaction potential. Dispersive interactions are typically modeled by Buckingham exp-6, Lennard-Jones 12-6, or Lennard-Jones 9-6 sites. These potentials also describe the repulsive forces caused by overlaps of the electron orbitals, in some cases supported by hard-sphere potentials.

Static polarities of the molecules are modeled by either partial charges or dipolar and/or quadrupolar potentials. Some models apply polarizable potentials to account for, e.g., different dipolar moments in gaseous and liquid states. Intramolecular interactions are modeled by torsional, angle, and bond stretching potentials. For hydrogen bonding, different modeling approaches are proposed in the literature, e.g. square well potentials [148] or a suitable arrangement of partial charges [34].

The different interaction parameters of the molecular models are substance specific constants, which are obtained depending on the modeling approach. They can be directly taken, e.g., from microscopic experimental data like dipolar moments or determined from QM methods. Another approach is the empirical adjustment of the microscopic parameters to macroscopic experimental data like bulk density or vapor pressure.

Besides a large number of molecular models developed *ad hoc* for individual substances, also transferable force fields were proposed in the literature, which are designed for the prediction of specific properties of numerous substances in a group contribution fashion: OPLS [82, 84], AMBER [21, 22, 223], CHARMM [13, 118], GROMOS [153], COMPASS [196], NERD [142], and TraPPE force fields [122]. Additional force fields are presented in [196]. These force fields are commonly optimized to cases, which are only partially relevant in process engineering. Thus, predictions of thermophysical properties, e.g. phase equilibrium properties, with these force fields are often insufficient [120].

The OPLS force field was optimized for simulations of the liquid phase and AMBER, CHARMM, GROMOS, and COMPASS force fields are predominantly used in biomolecular or macromolecular simulations, e.g. proteins in aqueous solutions. The NERD and TraPPE force fields yield comparably good results for vapor-liquid equilibria (VLE) [35, 122, 142, 226], but are available for a restricted class of substances only.

1.2 Contributions of the Present Work

The present work is based on a modeling approach residing on two branches, which was used to develop molecular models at the Institute for Technical Thermodynamics and Thermal Process Engineering (ITT), University of Stuttgart, Germany, prior to this work. Firstly, a systematic investigation on a particular model class, i.e. the two-center Lennard-Jones plus point dipole (2CLJD) or plus linear point quadrupole (2CLJQ) [187, 190], was performed. From these results, correlations for important thermophysical properties, i.e. vapor pressure, saturated liquid density, and enthalpy of vaporization, of the model fluids were developed as functions of the model parameters. Subsequently, model parameters for real substances were determined by adjusting the correlations to experimental data. This was done to parametrize molecular models for 78 real substances, mostly two-atomic molecules and short chain refrigerants [188, 219].

Secondly, Lennard-Jones based molecular models were individually optimized to experimental VLE data, i.e. saturated liquid density and vapor pressure. Here, an iterative method based on the sensitivities of the model parameters was used to develop molecular models for numerous substances [171, 186]. These molecular models not only outstandingly correlate experimental VLE data with typical deviations below 5, 1, and 5 % for vapor pressure, saturated liquid density, and enthalpy of vaporization, respectively. They also allow reliable extrapolations of thermal and caloric data over a wide range of states [216] and have proven their usefulness by applications to the prediction of transport properties and the surface tension [42–47, 215] as well as mixture properties [71, 189, 213, 214, 220].

For more complex molecules, the parametrization method based on phenomenological data alone is no more reasonable. The large number of model parameters does not allow for a purely empirical optimization. Here, the inclusion of results from QM calculations in the parametrization process provides valuable information. Many molecular parameters can be determined directly from QM or at least be initialized well for a subsequent optimization.

In the present work, a systematic strategy is developed to parametrize molecular models based on results from QM calculations. This approach is used to develop molecular

models for a set of pure substances. A detailed overview of the method and a summary of the proposed new molecular models and results is given in Chapter 3.

The new molecular models are subsequently applied to different real-life problems. Here, generally no further adjustments are made so that the results are strictly predictive to demonstrate the extrapolative power of the method. The results are summarized in Chapter 4.

Finally, in Chapter 5 an application of molecular modeling and simulation to hydrogels is presented. This preliminary study, where the applicability of the method is tested, gives hints for further research in this field.

The presented results were also published in a set of articles in international, peer-reviewed journals [27–31] and presented on various national and international conferences.

2 Fundamentals

In this chapter, a brief overview on the underlying theory is given. For a more detailed description, several textbooks are available. A good introduction into the matter is given by Allen and Tildesley [3] as well as Frenkel and Smit [50]. Together with an common overview, they present specific simulation approaches necessary to perform molecular simulations.

Here, the description of the theoretical background is restricted to topics that are extensively used in the present work. The focus is set on the determination of the VLE. The VLE properties were used for the parametrization of the molecular models as described later on. The theory and simulation methods for other properties, e.g. caloric or transport properties, will be presented together with their applications, cf. Chapter 4.

2.1 Molecular Modeling and Simulation

Based on statistical thermodynamics, molecular modeling and simulation yields thermophysical properties from studies on the molecular level. By solely defining the interactions between molecules, properties of pure substances as well as mixtures can be calculated. The description of the intermolecular interactions, usually given in terms of interaction energy, is hereby termed molecular model. This molecular model fully determines the thermophysical properties, which can be calculated by molecular simulation.

Many different approaches for molecular models are suggested in the literature. In the present work, the Lennard-Jones 12-6 type potential (LJ) [80, 81] plus superimposed electrostatics is used throughout. A detailed description of the setup and parametrization of the molecular models gives Chapter 3.

A set of molecules, typically in the order of 1000 molecules, is evaluated according to their interactions in molecular simulation. This is typically done in either of two different ways: molecular dynamics (MD) and Monte Carlo (MC) simulation. The goal of both simulation techniques is the generation of a representative set of molecular configurations, which allows the determination of the desired properties. Within a MD simulation, the forces (and torques) between the molecules are calculated from the intermolecular potential. The movement of the molecules simply follows Newton's laws of motion and is found from a time discretized numerical integration.

Alternatively, MC simulations use a stochastic approach to generate a set of representative molecular configurations. Random movements, e.g. translation or rotation, are applied to single molecules within the simulation to generate new arrangements. To sample energetically favoured arrangements with a higher probability, acceptance rules are applied for the moves.

A further description of the simulation methods can be found in the literature [3, 50]. There, also coding examples are given and practical issues are discussed.

2.2 Macroscopic Thermophysical Properties

All macroscopic observable thermophysical properties are averages of the corresponding microscopic properties, which can be obtained from molecular simulation on the molecular level. The conversion between the microscopic and macroscopic level is done by statistical thermodynamics.

Considering an arbitrary macroscopic observable A, it is obvious that, assuming a sufficiently large microscopic system, the macroscopic value is the time average of the microscopic property $\mathcal{A}(\mathbf{\Gamma})$ taken over a sufficiently long time interval t

$$A = \langle \mathcal{A}(\mathbf{\Gamma}(t)) \rangle = \lim_{t \to \infty} \frac{1}{t} \int_0^t \mathcal{A}(\mathbf{\Gamma}(\tau)) d\tau \ , \tag{2.1}$$

where $\mathbf{\Gamma}(\tau)$ indicates the phase space, i.e. the current state of the microscopic system, at time τ. The angular brackets denote an averaging, with respect to time here. The necessary size of the microscopic system depends on the desired property, but was found to be in the range of 1000 molecules for common thermophysical properties of the bulk. The time evolution in Equation (2.1) can directly be evaluated by MD simulation in a stepwise fashion. As averaging over an infinite time span is not possible, the integration is done over a finite time t. The length of this time span as well as the size of the regarded phase space $\mathbf{\Gamma}$ and the choice of the initial state $\mathbf{\Gamma}(0)$ have been subject to many publications, cf. [3], and should be chosen and tested sensibly for the desired property A.

Following the hypothesis of ergodicity, the time average can be substituted by an ensemble average

$$A = \langle \mathcal{A} \rangle_{ens} = \sum_{\mathbf{\Gamma}} \mathcal{A}(\gamma) \rho(\gamma) \ . \tag{2.2}$$

The microscopic property $\mathcal{A}(\gamma)$ observed at a specific microscopic state γ within the phase space $\mathbf{\Gamma}$ is weighted with the phase space density $\rho(\gamma)$, i.e. the probability of this

specific microscopic state to emerge. An (infinite) summation over the complete phase space is also not possible in this case. Instead, with MC simulation it is aimed to sample a representative part of the phase space. The phase space density is usually replaced by a weighting factor $w(\gamma)$, which leads to

$$\langle A \rangle_{ens} = \frac{\sum_\Gamma A(\gamma) w(\gamma)}{\sum_\Gamma w(\gamma)} \,. \tag{2.3}$$

Appropriate weighting functions w can be defined for the different ensembles, cf. [3]. For example, the weighting function for the isothermal-isobaric (NpT) ensemble is given by

$$w_{NpT} = e^{-\beta(\mathcal{H} + p\mathcal{V})} \,, \tag{2.4}$$

where $\mathcal{H}$ is the Hamiltonian and $\mathcal{V}$ the volume of the regarded microscopic system. $\beta = 1/(k_B T)$ denotes the Boltzmann factor, while T and p are the specified temperature and pressure of the ensemble. Analogously to the time average, questions on the necessary number of observed state points, extent of the regarded phase space, and choice of the initial microscopic state arise.

Definitions and equations for the corresponding microscopic properties of the common macroscopic observables are given in [3, 50]. Some of them are repeated in Section 4.3 as they were used for the prediction of different properties of ethylene oxide.

2.3 Chemical Potential

The chemical potential is an important property for the determination of phase equilibria. As it is extensively used throughout the present work, a more detailed discussion regarding its calculation is given here.

The microscopic definition of the chemical potential μ is given by [57]

$$\mu = \left(\frac{\partial G}{\partial N}\right)_{T,p} = \left(\frac{\partial F}{\partial N}\right)_{T,V} \,, \tag{2.5}$$

where G denotes the Gibbs enthalpy of a system containing N molecules and F its Helmholtz energy. Starting from this definition, different methods have been derived for the calculation of the chemical potential. In the present work, two methods were employed: the test particle insertion method by Widom [228] and the gradual insertion method [147, 178, 217].

2.3.1 Widom's Test Particle Method

Widom's test particle method is based on the introduction of test particles to a given system in a molecular simulation. For large N, the partial derivative can be approximated by

$$\mu \approx (G(N+1) - G(N))_{T,p} \ . \tag{2.6}$$

Considering an isothermal-isobaric system, $G(N)$ equals to $-k_\mathrm{B}T\ln(Q_{NpT})$ and the difference $\Delta G_{N+1,N} = G(N+1) - G(N)$ can be written as [228]

$$\Delta G_{N+1,N} = -k_\mathrm{B}T \ln\left(\frac{Q_{N+1}}{Q_N}\right) \ , \tag{2.7}$$

where k_B denotes the Boltzmann constant and Q_{NpT} is the partition function of the NpT ensemble. From this equation, an expression for the chemical potential can be obtained [228, 229]

$$\mu = \mu^{\mathrm{id}}(T) - k_\mathrm{B}T \ln\langle\rho\rangle - k_\mathrm{B}T \ln\left\langle \frac{V}{N} \exp\left\{-\beta\psi_{\mathrm{test}}\right\}\right\rangle \ , \tag{2.8}$$

where $\mu^{\mathrm{id}}(T)$ denotes the solely temperature dependent ideal part of the chemical potential. ρ is the density and V the volume of the simulation. ψ_{test} is the interaction energy of a test particle, upon addition to the system of N molecules. The test particle acts here as a ghost particle without influencing the other molecules. Finally, the angle brackets denote both, an ensemble average and an average over a (large) number of test particles.

Widom's test particle method gives a straightforward and computationally efficient route to calculate the chemical potential. Unfortunately, the method fails, when the probability of a successful insertion of a test particle, i.e. an insertion where no overlaps with other particles occur, becomes too low. This is predominantly the case in cold and strongly interacting liquids, where the densities are indeed very high.

2.3.2 Gradual Insertion

A more advanced method for the determination of the chemical potential, which solves most of the problems of Widom's method, is gradual insertion. Instead of inserting complete molecules, a fluctuating particle is introduced, which can appear in different states of coupling with all other molecules. In the decoupled state, the fluctuating particle is not present, while in the fully coupled state, it acts like a real molecule.

Between these states, a set of partially coupled states are defined, building up the real particle interaction in a stepwise manner, cf. Figure 2.1.

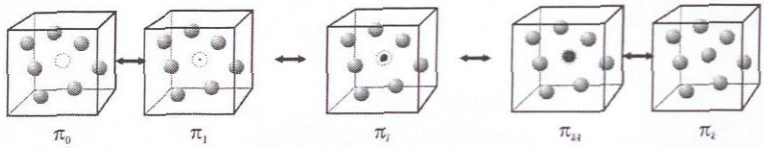

Figure 2.1: Illustration of the gradual insertion of a molecule. The fluctuating particle (dark gray) fluctuates between state 0 (fully decoupled) and state k (fully coupled).

The $N-1$ real molecules plus the fluctuating particle π_i in state of coupling i form a set of sub-ensembles, which can be depicted by the following scheme

$$[N+\pi_0] \leftrightarrow [N+\pi_1] \leftrightarrow \cdots \leftrightarrow [N+\pi_i] \cdots \leftrightarrow [N+\pi_{k-1}] \leftrightarrow [N+\pi_k] \; . \tag{2.9}$$

To switch between neighbouring sub-ensembles, an additional move is introduced into a standard MC simulation. The probability of accepting a change of the fluctuating particle from state of coupling i to state of coupling j is given by

$$P_{\text{acc}}(i \to j) = \min\left(1, \frac{w_j}{w_i} \cdot \exp\left\{-\beta(\psi_j - \psi_i)\right\}\right) \; , \tag{2.10}$$

where ψ_i denotes the interaction energy of the fluctuating particle in state of coupling i. The fluctuating states are weighted with weighting factors w_i to avoid an unbalanced sampling of the different states.

The chemical potential then can be calculated from [217]

$$\mu = \mu^{\text{id}}(T) - k_{\text{B}}T \cdot \ln\langle\rho\rangle - k_{\text{B}}T \cdot \ln\left\langle \frac{V}{N} \cdot \frac{w_0}{w_k} \cdot \frac{\mathrm{P}[N+\pi_k]}{\mathrm{P}[N+\pi_0]} \right\rangle \; , \tag{2.11}$$

where $\mathrm{P}[N+\pi_0]$ and $\mathrm{P}[N+\pi_k]$ are the probabilities to observe an ensemble with the fluctuating particle fully decoupled and fully coupled, respectively. The angle brackets denote the ensemble average.

Depending on the choice of the partially coupled states and the weighting factors, the gradual insertion method yields good results for the chemical potential in cases where Widom's test particle method fails. Disadvantages of the method are the significantly extended simulation time and the additional effort needed to define the fluctuating states and weighting factors [147, 217].

2.4 Determination of Vapor-Liquid Equilibria

Based on the chemical potential, the VLE of pure components and mixtures can be determined. Coexisting phases are in equilibrium if they are in thermal, mechanical, and chemical equilibrium, i.e. if the equations

$$T' = T'' \, , p' = p'' \, , \text{and } \mu_i' = \mu_i'' \, , \tag{2.12}$$

hold, where T, p, and μ_i are temperature, pressure, and chemical potential of component i, respectively, and the apostrophes denote the different phases. Of course, chemical equilibrium must hold for all components in a mixture.

Different approaches can be found in the literature, which are applicable to determine phase equilibria by molecular simulation. Predominantely applied are the NpT+test particle method proposed by Möller et al. [131, 132] or the Gibbs ensemble technique proposed by Panagiotopoulos [154]. In the present work, the Grand Equilibrium method proposed by Vrabec and Hasse [212] was used. It shows some advantages over other approaches [212] and works well with the systems studied in this work.

The Grand Equilibrium method separates the phase equilibrium simulation into two steps. Firstly, the liquid phase is simulated at specified temperature T and composition, which is given by the set of mole fractions $x_1, \ldots, x_n$, as well as a rough estimate of the vapor pressure p_0 in a NpT ensemble simulation. During this simulation, the liquid density ρ^l, the chemical potentials in the liquid phase μ_i^l, and the partial molar volumes v_i^l of all components i are determined. Note that in case of pure substances, the partial molar volume is simply the molar volume $v = 1/\rho$.

Subsequently, the vapor phase is simulated in a pseudo-μVT ensemble, where the temperature T is specified to be the same as for the liquid simulation and the simulation box volume is set sufficiently large for good statistics. While the simulation proceeds, the chemical potential μ_i is adjusted by insertions and deletions of particles to the first order pressure-corrected chemical potential of the liquid

$$\mu_i = \mu_{i,0}^l(T, p_0) + v_i^l \cdot (p - p_0) \, , \tag{2.13}$$

where p is the actual pressure in the vapor phase simulation.

Applying this simulation scheme, the vapor phase simulation converges to the dew point corresponding to the specified temperature and liquid composition in the first step. The vapor pressure p^σ as well as density ρ'' and enthalpy h'' of the saturated vapor are directly determined from the vapor phase simulation. The saturated liquid density ρ' and saturated liquid enthalpy h' are extrapolated by a first order Taylor series from the

results of the liquid simulation run at p_0

$$\rho' = \rho^{\mathrm{l}}(T, p_0) + \beta_T^{\mathrm{l}} \rho^{\mathrm{l}}(p^\sigma - p_0) \,, \tag{2.14}$$

and

$$h' = h^{\mathrm{l}}(T, p_0) + \left(\frac{\partial h}{\partial p}\right)_T^{\mathrm{l}} (p^\sigma - p_0) \,, \tag{2.15}$$

where β_T^{l} denotes the isothermal compressibility and $(\partial h/\partial p)_T^{\mathrm{l}}$ the partial derivative of the enthalpy with respect to the pressure at constant temperature and composition in the liquid phase.

3 Molecular Models of Real Fluids

As mentioned before, a central obstacle for a broader use of molecular methods in process engineering applications is the limited availability of molecular models of desired quality. A primary objective of the present work is the development of a systematic strategy for the development of new sufficiently accurate molecular models.

For many substances, transferable molecular models have been developed, i.e. force fields for classes of compounds like alkanes or alcohols. Thereby, it is assumed that the parameters for functional groups are valid for different molecular species. The main disadvantage of transferable models is that their parameters were adjusted for the whole substance class and may not be optimal for a specific substance. Furthermore, they do not cover substances outside the modeled class. An overview and assessment of some commonly used transferable potentials can be found in [120].

Molecular models that were optimized for specific substances are available only for selected compounds and, particularly older ones, sometimes do not show the desired quality needed for real-world applications. Therefore, from an engineering point of view, a method for the rapid development of new molecular models for specific substances is of great interest. Moreover, the molecular models should be accurate, simple, and computationally efficient.

The present work is restricted to rigid, non-polarizable models for comparatively small molecules. The molecular models have state-independent parameters throughout. For computational efficiency, the united-atom approach is used, i.e. hydrogen atoms bonded to other atoms are not modeled explicitly where possible.

The proposed strategy uses information from quantum mechanical (QM) *ab initio* calculations to include physically sound molecular properties and to reduce the number of adjustable parameters. A remaining subset of model parameters – typically two to four – is subsequently optimized by adjustment to experimental data on VLE of the pure substances. The aim is to achieve deviations to experimental values for the vapor pressure, saturated liquid density, and enthalpy of vaporization in the range from triple point to critical point of below 5, 1, and 5 %, respectively.

Such accurate models are known from prior work [42–45, 71, 173, 174, 189, 213, 214, 216, 218, 220] to have an excellent extrapolative and predictive power. This is also shown within the present work for some examples in Chapter 4.

Molecular models that were developed on the basis of QM calculations, like it is done here, stand between strictly *ab initio* models and fully empirical models. The present strategy is based on the idea to include substantial *ab initio* information to achieve a sound physical basis without giving up the freedom to reasonably optimize the model to important macroscopic thermodynamic properties. Thus, for the modeling process some experimental data is needed for optimization. All three chosen properties, i.e. vapor pressure, saturated liquid density, and enthalpy of vaporization, have the advantage to be well available for numerous engineering fluids and to represent dominant features of the fluid state and phase coexistence.

3.1 Modeling Strategy

The parameters of a molecular model can be separated into three groups. Firstly, geometric parameters specify the locations of the different interaction sites of the molecular model. Secondly, electrostatic parameters define the interactions of static polarities of single molecules. And finally, dispersive and repulsive parameters determine the attraction by London forces and the repulsion by overlaps of the electronic orbitals. Here, the Lennard-Jones 12-6 (LJ) potential [80, 81] was used to assure a straightforward compatibility with the majority of the molecular models in the literature.

To describe the intermolecular interactions, a varying number of LJ sites and superimposed ideal point dipoles and/or ideal linear point quadrupoles were used. Point dipoles or quadrupoles were employed for the description of the electrostatic interactions to reduce the computational effort significantly. A point dipole may, e.g. when a simulation program does not support this interaction site type, be approximated by two point charges $\pm q$ separated by a distance l. Limited to small l, one is free to choose this distance as long as $\mu = ql$ holds. Analogously, a point quadrupole can be approximated by three collinear point charges q, $-2q$, and q separated by l each, where $Q = 2ql^2$.

In case of hydrogen bonding fluids, the hydrogen bonding and electrostatic interactions are modeled by a common set of partial charges. This modeling approach was found to yield good results on a set of hydrogen bonding substances, e.g. methanol [173], ethanol [174], formic acid [172], or mono- and dimethylamine [176]. The strong interaction and directional dependence of hydrogen bonds is modeled by an eccentric positive partial charge on a negatively charged LJ site. An example is the molecular model for ammonia presented in Section 3.5.1.

The total intermolecular interaction energy of a system of N molecules modeled as described above writes as

$$U(N) = \sum_{i=1}^{N-1} \sum_{j=i+1}^{N} \left\{ \sum_{a=1}^{S_i^{\mathrm{LJ}}} \sum_{b=1}^{S_j^{\mathrm{LJ}}} 4\varepsilon_{ijab} \left[\left(\frac{\sigma_{ijab}}{r_{ijab}} \right)^{12} - \left(\frac{\sigma_{ijab}}{r_{ijab}} \right)^{6} \right] + \right.$$
$$\sum_{c=1}^{S_i^{\mathrm{e}}} \sum_{d=1}^{S_j^{\mathrm{e}}} \frac{1}{4\pi\epsilon_0} \left[\frac{q_{ic}q_{jd}}{r_{ijcd}} + \frac{q_{ic}\mu_{jd}}{r_{ijcd}^2} \cdot f_1(\boldsymbol{\omega}_j) + \frac{q_{ic}Q_{jd}}{r_{ijcd}^3} \cdot f_2(\boldsymbol{\omega}_j) + \right.$$
$$\frac{\mu_{ic}q_{jd}}{r_{ijcd}^2} \cdot f_3(\boldsymbol{\omega}_i) + \frac{\mu_{ic}\mu_{jd}}{r_{ijcd}^3} \cdot f_4(\boldsymbol{\omega}_i, \boldsymbol{\omega}_j) + \frac{\mu_{ic}Q_{jd}}{r_{ijcd}^4} \cdot f_5(\boldsymbol{\omega}_i, \boldsymbol{\omega}_j) +$$
$$\left. \left. \frac{Q_{ic}q_{jd}}{r_{ijcd}^3} \cdot f_6(\boldsymbol{\omega}_i) + \frac{Q_{ic}\mu_{jd}}{r_{ijcd}^4} \cdot f_7(\boldsymbol{\omega}_i, \boldsymbol{\omega}_j) + \frac{Q_{ic}Q_{jd}}{r_{ijcd}^5} \cdot f_8(\boldsymbol{\omega}_i, \boldsymbol{\omega}_j) \right] \right\}, \quad (3.1)$$

where r_{ijab}, ε_{ijab}, σ_{ijab} are the distance, the LJ energy parameter, and the LJ size parameter, respectively, for the pair-wise interaction between LJ site a on molecule i and LJ site b on molecule j. ϵ_0 is the permittivity of vacuum, whereas q_{ic}, μ_{ic}, and Q_{ic} denote the partial charge, the dipole moment, and the quadrupole moment of the electrostatic interaction site c on molecule i, and so forth. $f_x(\boldsymbol{\omega}_i)$ and $f_x(\boldsymbol{\omega}_i, \boldsymbol{\omega}_j)$ are expressions for the dependency of the electrostatic dipolar and quadrupolar interactions on the orientions $\boldsymbol{\omega}_i$ and $\boldsymbol{\omega}_j$ of the molecules i and j, cf. [3, 57]. Finally, the summation limits N, S_x^{LJ}, and S_x^{e} denote the number of molecules, the number of LJ sites, and the number of electrostatic sites, respectively.

Interactions between LJ sites of different type are determined here by applying the standard Lorentz-Berthelot combining rules [6, 112]

$$\sigma_{ijab} = \frac{\sigma_{iiaa} + \sigma_{jjbb}}{2}, \quad (3.2)$$

and

$$\varepsilon_{ijab} = \sqrt{\varepsilon_{iiaa}\varepsilon_{jjbb}}. \quad (3.3)$$

In case of mixtures, this combining rules are extended by one adjustable binary parameter ξ in the energy term

$$\varepsilon_{ijab} = \xi_{\mathrm{AB}} \sqrt{\varepsilon_{iiaa}\varepsilon_{jjbb}}. \quad (3.4)$$

This state-independent binary parameter ξ_{AB} is adjusted once per binary mixture A-B to a single reliable experimental VLE data point, e.g. to a vapor pressure. Subsequently, ξ_{AB} is applied to all interactions between a molecule of species A and a molecule of species B also in higher, e.g ternary or quarternary, mixtures. This approach was found to be superior to other approaches from the literature [175].

3.2 Molecular Properties from Quantum Mechanics

In a recent publication, Sandler et al. [168] give a brief overview on the use of QM for the calculation of thermophysical properties. By numerically solving Schrödinger's equation under some common consumptions, it is nowadays possible to calculate different molecular properties for technically relevant components in a quite standardized way. Many different QM codes are available for this task. For license reasons, the open source code GAMESS(US) [170] was used in the present work.

3.2.1 Geometry

The geometric data of the molecular models developed in the present work, i.e. bond lengths, angles, and dihedrals, were directly taken from QM calculations. Therefore, a geometry optimization, i.e. an energy minimization, was initially performed using GAMESS(US) [170]. The Hartree-Fock level of theory was applied with a relatively small (6-31G) basis set. Alternatively, density functional theory (DFT) methods, e.g. BLY3P, can be used, as they are known to give reasonable results for the molecular structure [104].

The resulting configuration of the atoms was taken without subsequent modification to specify the positions of the LJ sites in space, except for the hydrogen atoms. As the united-atom approach was used to obtain computationally efficient molecular models, the hydrogen atoms were modeled together with the atom they are bonded to. In case of methylene (CH_2) and methyl (CH_3) united atom sites, the LJ potential was located at the geometric mean of the nuclei, while the methine (CH) united atom site was located at 0.4 of the distance between carbon and hydrogen atom, cf. Figure 3.1. These empirical offsets are in good agreement with the results of Ungerer et al. [208], which were found by optimization of transferable molecular models for n-alkanes.

3.2.2 Electrostatics

Intermolecular electrostatic interactions mainly occur due to static polarities of single molecules that can well be obtained by QM. Here, the Møller-Plesset 2 level was used that considers electron correlation in combination with the polarizable 6-311G(d,p) basis set.

The purpose of the present task is the development of effective pair potentials with a state-independent set of model parameters. Obviously, the electrostatic interactions have a greater influence in the liquid state than in the gaseous state due to the higher density. Furthermore, they have a higher magnitude in the liquid. Thus, for the cal-

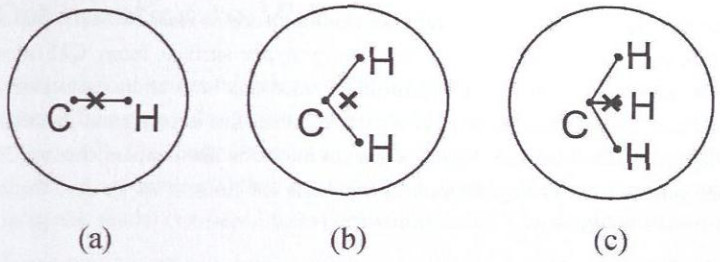

Figure 3.1: Geometry of the united-atom sites: (a) The methine (CH) site is located at 0.4 of the carbon-hydrogen distance, (b) the methylene (CH_2) site and (c) the methyl (CH_3) site are located at the geometric mean.

culation of the electrostatic moments by QM, a liquid-like state should be considered. This was done here by placing the molecule within a dielectric continuum and assigning the experimental dielectric constant of the liquid to it, as in the COSMO method [93].

From the resulting electron density distribution for the small symmetric molecules regarded here, ideal point dipoles and ideal linear point quadrupoles were estimated by simple integration over the orbitals. Magnitudes and orientations of these electrostatic interaction sites were passed on to the molecular models without any modification.

For other, more complex molecules, more sophisticated methods like CHELP [19], CHELPG [12], or the distributed multipole analysis [191] are available in the literature. These methods adjust a set of partial charges or higher order electrostatic sites to the electrostatic potential around the molecule as determined by QM. Although they are able to reflect the electrostatic interactions with higher accuracy, they are not considered here. As these models use, e.g., the nucleus sites to place partial charges and/or multipoles instead of trying to minimize the number of interaction sites by simultaneously optimizing the positions, they always yield a larger number of sites. Thus, they lead to computationally more expensive molecular models.

3.2.3 Dispersion and Repulsion

It would be highly desirable to also calculate the dispersive and repulsive interactions using *ab initio* methods as well. This approach was followed by different authors in the past, e.g. for neon [32, 52, 141, 210], argon [33, 141, 210], krypton [140], nitrogen [107], carbon dioxide [224], hydrogen chloride [136], acetonitrile [70], methanol [70], acetylene [53], and methanethiol [54]. However, from an engineering point of view, this leads to difficulties.

For an estimation of dispersive and repulsive interactions at least two molecules must be taken into account. To properly scan the energy hyper surface, many QM calculations at different molecular distances and mutual orientations have to be performed. As the dispersive, and partly also the repulsive, interactions are a very small fraction of the total energy calculated by QM, highly accurate methods like coupled cluster (CC) with large basis sets or even extrapolations to the basis set limit must be used for this task [168].

Due to the fact that this is computationally too expensive for engineering purposes, the parameters for the dispersive and repulsive interactions for an initial model are taken from similar sites of other molecular models. Some of these parameters were subsequently fitted in the optimization process to yield the quantitatively correct VLE behavior of the modeled substance.

3.2.4 Hydrogen Bonding

For the description of hydrogen bonds, an approach proposed by Schnabel et al. [172–174, 176] was used. Hydrogen bonding is modeled by eccentric partial charges located on a united-atom LJ site, which acts both as hydrogen bond donor and acceptor. Figure 3.2 illustrates such a hydrogen bonding model site. The position of the partial charges is specified according to the nuclei positions from QM, cf. Section 3.2.1, while the united-atom LJ site is located at the donor/acceptor position. This model potential interacts strongly with potentials of the same type within specific distances and orientations typically for hydrogen bonding [171].

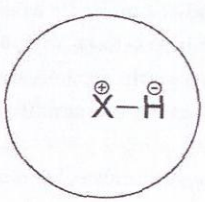

Figure 3.2: Model site for hydrogen bonds. X denotes the hydrogen bond donor/acceptor atom (e.g. O or N). The partial charges are located at the nucleus sites, while the sphere denotes the LJ potential located at the donor/acceptor atom site.

The magnitudes of the partial charges are specified to obtain the same overall polar moments as calculated by QM for an initial molecular model. These charges are optimized subsequently to achieve the correct description of the VLE properties of the considered substance.

3.3 Optimization to VLE Data

The optimization was performed using a Newton scheme as proposed by Stoll [186]. The applied method has many similarities with the one published by Ungerer et al. [207] and later on modified by Bourasseau et al. [8]. It relies on a least-square minimization of a weighted fitness function $\mathcal{F}$ that quantifies the deviations of simulation results from a given molecular model compared to experimental data. The weighted fitness function writes as

$$\mathcal{F} = \frac{1}{d} \sum_{i=1}^{d} \frac{1}{(\delta A_{i,\mathrm{sim}})^2} (A_{i,\mathrm{sim}}(\boldsymbol{M}_0) - A_{i,\mathrm{exp}})^2 \,, \tag{3.5}$$

wherein the n-dimensional vector $\boldsymbol{M}_0 = (m_{0,1}, ..., m_{0,n})$ represents the set of n model parameters $m_{0,1}, ..., m_{0,n}$ to be optimized. The deviations of simulation results with a given parameter set $A_{i,\mathrm{sim}}$ to experimental data $A_{i,\mathrm{exp}}$ are weighted with the expected simulation uncertainties $\delta A_{i,\mathrm{sim}}$. Equation (3.5) allows a simultaneous adjustment of the model parameters to different thermophysical properties A_i (saturated liquid density ρ', vapor pressure p_σ, and enthalpy of vaporization Δh_v at various temperatures in the present work).

The unknown functional dependence of the property A_i on the model parameters is approximated by a first order Taylor series developed around the initial parameter set $\boldsymbol{M}_0$

$$A_{i,\mathrm{sim}}(\boldsymbol{M}_{\mathrm{new}}) = A_{i,\mathrm{sim}}(\boldsymbol{M}_0) + \sum_{j=1}^{n} \frac{\partial A_{i,\mathrm{sim}}}{\partial m_j} \cdot (m_{\mathrm{new},j} - m_{0,j}) \,. \tag{3.6}$$

Therein, the partial derivatives of A_i with respect to each model parameter m_j, i.e. the sensitivities, are approximated by difference quotients

$$\frac{\partial A_{i,\mathrm{sim}}}{\partial m_j} \approx \frac{A_{i,\mathrm{sim}}(m_{0,1}, ..., m_{0,j} + \Delta m_j, ..., m_{0,n}) - A_{i,\mathrm{sim}}(m_{0,1}, ..., m_{0,j}, ..., m_{0,n})}{\Delta m_j} \,. \tag{3.7}$$

Assuming a sound choice of the model parameter variations Δm_j, i.e. small enough to ensure linearity and large enough to yield differences in the simulation results significantly above the statistical uncertainties, this method allows a step-wise optimization of the molecular model by minimization of the fitness function $\mathcal{F}$. Experience shows that an optimized set of model parameters was usually found within a few iterative steps when starting from a reasonable initial model.

Correlations for vapor pressure, saturated liquid density, and enthalpy of vaporization were used as "experimental data" for model adjustment and evaluation. These correlations are either based on reference quality equations of state (EOS) taken from [105], where available, or taken from the DIPPR database [165]. The latter was done even in

cases where the DIPPR correlations are based upon no or only few true experimental data points, as the correlations were regarded as best practice. The comparison between simulation results and experiment was done by using fits to the simulation data according to Lotfi et al. [114] that smooth out some scattering of the simulation results. These fits are discussed in greater detail in Section 4.3. The relative deviation between fit and correlation was calculated in steps of 1 K from 55 to 97 % of the critical temperature and is denoted by *mean unsigned error* in the following.

3.4 Application to Molecules from Different Substance Classes

For a test of the proposed modeling strategy, a set of ten molecules from different substance classes, i.e. iso-butane, cyclohexane, formaldehyde, dimethyl ether, dimethyl sulfide, thiophene, hydrogen cyanide, acetonitrile, and nitromethane, is selected to check the general applicability [31]. The present work is restricted to small molecules, where the internal degrees of freedom may be neglected. Thus, the molecular models are rigid, using the most stable configuration determined by QM.

The optimized parameter sets of the new molecular models are summarized in Table 3.1. Table 3.2 compares the critical properties from simulation to experimental data. The critical properties from simulation are obtained through fits to VLE simulation results as suggested by Lotfi et al. [114]. The estimated uncertainties of critical temperature, critical density, and critical pressure from simulation are 0.5, 2, and 2 %, respectively. A very good agreement between simulation and experiment is reached, being predominantly within the combined error bars.

In the following sections, substance specific details are briefly discussed. Furthermore, references to alternative models from the literature are given and the simulation results from the present models are compared to simulation data from the literature where available.

Table 3.1: Parameters of the new molecular models. LJ interaction sites are denoted by the modeled atoms (in boldface) with an additional bonding partner, if necessary. Electrostatic interaction sites are denoted by dipole or quadrupole, respectively. Coordinates are given with respect to the center of mass in a principal axes system. Orientations of the electrostatic sites are defined by standard Euler angles, where φ is the azimuthal angle with respect to the $x-z$ plane and θ is the inclination angle with respect to the z axis.

Interaction	x	y	z	σ	ε/k_B	θ	φ	μ	Q
Site	Å	Å	Å	Å	K	deg	deg	D	B
iso-butane									
CH	0	0	0.8179	3.360	51.00	—	—	—	—
CH_3(1)	1.7302	0	-0.1893	3.607	120.15	—	—	—	—
CH_3(2)	-0.8651	1.4984	-0.1893	3.607	120.15	—	—	—	—
CH_3(3)	-0.8651	-1.4984	-0.1893	3.607	120.15	—	—	—	—
dipole	0	0	0	—	—	0	0	0.1347	—
quadrupole	0	0	0	—	—	0	0	—	0.7236
cyclohexane									
CH_2(1)	0.0210	-0.3118	1.8052	3.497	87.39	—	—	—	—
CH_2(2)	1.5318	0.2989	0.8863	3.497	87.39	—	—	—	—
CH_2(3)	-1.5528	0.2983	0.9986	3.497	87.39	—	—	—	—
CH_2(4)	1.5318	-0.2989	-0.8863	3.497	87.39	—	—	—	—
CH_2(5)	-1.5528	-0.2983	-0.9986	3.497	87.39	—	—	—	—
CH_2(6)	0.0210	0.3118	-1.8052	3.497	87.39	—	—	—	—
quadrupole	0	0	0	—	—	90	90	—	0.8179
formaldehyde									
O	0	0	0.6721	3.010	112.61	—	—	—	—
CH_2	0	0	-0.7682	3.422	77.42	—	—	—	—
dipole	0	0	0.0480	—	—	180	0	2.6668	—
dimethyl ether									
O	0	0	0.6427	2.727	89.57	—	—	—	—
CH_3(1)	1.4041	0	-0.3086	3.607	120.15	—	—	—	—
CH_3(2)	-1.4041	0	-0.3086	3.607	120.15	—	—	—	—
dipole	0	0	0	—	—	180	0	1.7040	—

continued on next page

continued from previous page

Interaction	x	y	z	σ	ε/k_B	θ	φ	μ	Q
Site	Å	Å	Å	Å	K	deg	deg	D	B
sulfur dioxide									
S	0	0	0.3757	3.312	139.23	—	—	—	—
O(1)	1.2790	0	-0.3653	3.106	43.18	—	—	—	—
O(2)	-1.2790	0	-0.3653	3.106	43.18	—	—	—	—
dipole	0	0	0	—	—	0	0	1.9980	—
quadrupole	0	0	0	—	—	90	0	—	-5.3340
dimethyl sulfide									
S	0	0	0.2819	3.398	207.57	—	—	—	—
CH$_3$(1)	1.1583	0	-0.3868	3.607	120.15	—	—	—	—
CH$_3$(2)	-1.1583	0	-0.3868	3.607	120.15	—	—	—	—
dipole	0	0	0	—	—	90	180	2.3610	—
quadrupole	0	0	0	—	—	90	0	—	3.0740
quadrupole	0	0	0	—	—	0	0	—	2.7600
thiophene									
S	0	0	0.7359	4.292	95.65	—	—	—	—
CH(1)-S	1.2513	0	0.2067	3.590	48.49	—	—	—	—
CH(2)-S	-1.2513	0	0.2067	3.590	48.49	—	—	—	—
CH(3)-CH	0.7734	0	-1.2643	3.590	48.49	—	—	—	—
CH(4)-CH	-0.7734	0	-1.2643	3.590	48.49	—	—	—	—
dipole	0	0	0	—	—	180	0	1.8120	—
quadrupole	0	0	0	—	—	90	0	—	6.5389
hydrogen cyanide									
N	0	0	0.6380	3.233	39.69	—	—	—	—
CH	0	0	-0.9671	3.445	102.44	—	—	—	—
dipole	0	0	0.0589	—	—	180	0	3.4084	—
quadrupole	0	0	0.0589	—	—	0	0	—	2.1800
acetonitrile									
N	0	0	1.1507	3.368	53.00	—	—	—	—
C	0	0	0.0507	2.810	10.64	—	—	—	—
CH$_3$	0	0	-1.2868	3.835	163.04	—	—	—	—
dipole	0	0	0	—	—	180	0	4.1186	—
quadrupole	0	0	0	—	—	0	0	—	-3.1373

continued on next page

continued from previous page

Interaction Site	x Å	y Å	z Å	σ Å	ε/k_B K	θ deg	φ deg	μ D	Q B
nitromethane									
N	0	0	0.2199	3.321	34.90	—	—	—	—
O(1)	1.1045	0	0.7858	3.060	45.17	—	—	—	—
O(2)	-1.1045	0	0.7858	3.060	45.17	—	—	—	—
CH_3	0	0	-1.5135	3.501	158.79	—	—	—	—
dipole	0	0	0.2535	—	—	180	0	3.9901	—
quadrupole	0	0	0.2535	—	—	90	0	—	-4.7903

Table 3.2: Critical properties: present simulation results compared to recommended experimental data. The numbers in parentheses indicate the experimental uncertainty in the last digits.

	T_c^{sim} K	T_c^{exp} K	ρ_c^{sim} mol/l	ρ_c^{exp} mol/l	p_c^{sim} MPa	p_c^{exp} MPa	Ref.
iso-butane	407	407.8(5)	3.87	3.86(5)	3.65	3.64(5)	[23]
cyclohexane	556	553.8(2)	3.26	3.25(2)	4.23	4.08(3)	[23]
formaldehyde	406	408	8.38	8.70	5.95	6.59	[162]
dimethyl ether	403	400.2(1)	5.99	5.95(2)	5.69	5.34(5)	[102]
sulfur dioxide	425	430.7(1)	8.15	8.2 (8)	7.22	7.9 (4)	[123]
dimethyl sulfide	511	503 (1)	4.95	4.91(8)	5.46	5.53(10)	[204]
thiophene	586	580 (1)	4.46	4.57(18)	6.05	5.7 (1)	[204]
hydrogencCyanide	448	457 (1)	7.89	7.4 (1)	4.69	5.4 (1)	[119]
acetonitrile	540	545.5(1)	6.04	5.8 (1)	4.95	4.85(3)	[119]
nitromethane	587	588 (1)	5.87	5.8 (0)	5.98	6.3 (1)	[101]

3.4.1 Iso-Butane and Cyclohexane

The branched alkane iso-butane and the cyclic alkane cyclohexane show only very weak static polarities. Here, the main contributions to the intermolecular interaction are dispersion and repulsion. The electrostatic interactions have only a minor influence but should not be neglected completely.

Different molecular models for iso-butane can be found in the literature, which are based on force fields for branched alkanes. The well-known OPLS force field by Jorgensen et al. is available in two versions for iso-butane, one using the united-atom approach [87] and one using an all-atom description [88]. Both OPLS force fields were optimized to liquid

density and enthalpy of vaporization at 293 K only. The model of Poncela et al. [160] was adjusted the second virial coefficient. For a better applicability in a wider range of states, recent molecular models were optimized to experimental VLE data. Examples from this group are the force fields presented by Nath and de Pablo [142], Martin and Siepmann [121], Bourasseau et al. [10], or Chang and Sandler [17].

For the present iso-butane model, four LJ sites, one for each methyl group and one for the methine group, are used to describe dispersion and repulsion. The polarity is modeled by a single (weak) dipole (0.1347 D) located in the center of mass. Orientation and magnitude of the dipole are taken from QM. For the initial model, the LJ parameters are taken from Ungerer et al. [208]. It is sufficient to adjust a single parameter, the offset distance of the methine group. It is optimized to 0.4 of the carbon-hydrogen distance, cf. Figure 3.1 and hold constant subsequently. The parameters of the present model are given in Table 3.1.

VLE simulation results on the basis of the present iso-butane model and experimental data are given in Appendix B. Figures 3.3 to 3.5 show saturated densities, vapor pressure, and enthalpy of vaporization, respectively, from the present iso-butane model in comparison to experimental data [105].

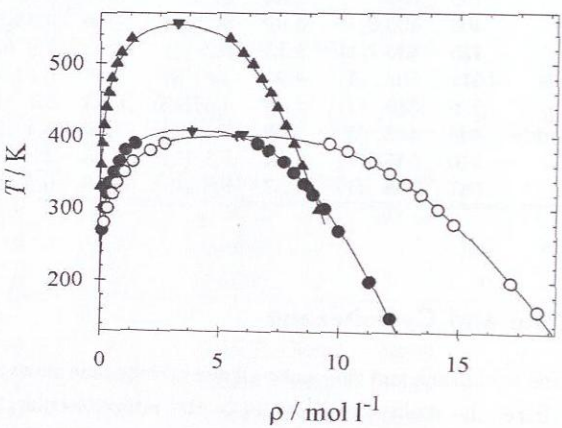

igure 3.3: Saturated densities. Present simulation data: ● iso-butane, ▲ cyclohexane, ○ dimethyl ether. — correlations of experimental data [105], ▼ critical points derived from simulation, + experimental critical points. Simulation uncertainties are within symbol size.

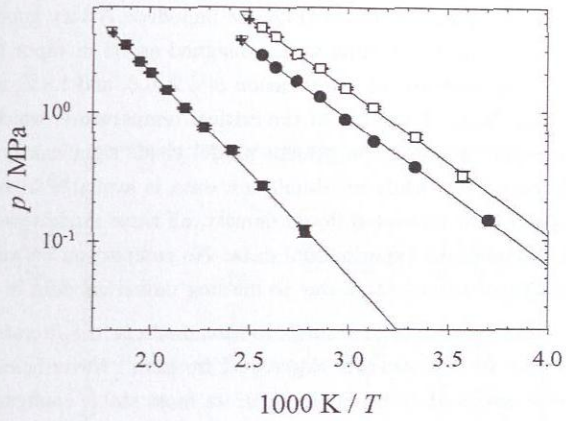

Figure 3.4: Vapor pressure. Present simulation data: ● iso-butane, ▲ cyclohexane, ○ dimethyl ether. — correlations of experimental data [105], ▼ critical points derived from simulation, + experimental critical points. Error bars indicate simulation uncertainties.

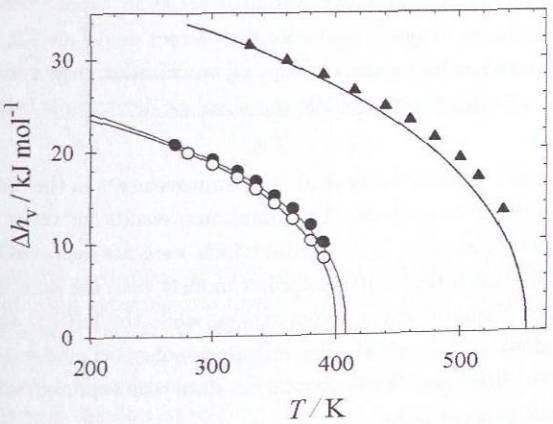

Figure 3.5: Enthalpy of vaporization. Present simulation data: ● iso-butane, ▲ cyclohexane, ○ dimethyl ether. — correlations of experimental data [105]. Simulation uncertainties are within symbol size.

Figure 3.6 shows a deviation plot between simulation and experimental data. In the deviation plot also simulation results from Martin and Siepmann [121], using their TraPPE force field, and from Nath and de Pablo [142] are included. A very good agreement is obtained for the present model yielding mean unsigned errors in vapor pressure, saturated liquid density, and enthalpy of vaporization of 4.2, 0.6, and 1.8 %, respectively, in the temperature range from 55 to 97 % of the critical temperature, which is about 225 to 395 K. For the vapor pressure, the present model yields significantly better results than the TraPPE force field, while no simulation data is available from Nath and de Pablo for this property. For saturated liquid density, all three models yield comparable results within 1 % deviation to experimental data. No comparison between the models is possible for enthalpy of vaporization due to missing numerical data in [121, 142].

For cyclohexane, different molecular models are available in the literature [9, 35, 41, 146] which all account for the internal degrees of freedom. Nevertheless, the present cyclohexane model is assumed to be rigid and in its most stable configuration, i.e. the saddle shape. The molecular model consists of six LJ sites, one for each methylene group. The static polarity is modeled by a single quadrupole parametrized according to QM. The two LJ parameters σ_{CH2} and ε_{CH2} are optimized to experimental VLE data. The parameters of the present model are given in Table 3.1.

Present simulation results and experimental data of VLE properties for cyclohexane are given in Appendix B. Figures 3.3 to 3.5 again show VLE simulation results in comparison to experimental data. Figure 3.7 shows the deviation plot including simulation results from Bourasseau et al. [10]. The mean unsigned errors in vapor pressure, saturated liquid density, and enthalpy of vaporization for the present model are 0.9, 0.5, and 5.6 %, respectively. Simulation results for the enthalpy of vaporization show systematic relative deviations towards the critical point, while the absolute deviation is below 2.5 kJ/mol, cf. Appendix B.

Compared to the model of Bourasseau et al. [10] improvements in the description of the saturated liquid density are achieved. The simulation results for vapor pressure agree within their assumed simulation uncertainties which were not reported by Bourasseau et al. An interesting point is that both molecular models yield the same deviations from experimental data on the enthalpy of vaporization, while the DIPPR database reports true experimental data up to 0.97 T_c. For all other molecular models for cyclohexane mentioned above, no numerical VLE simulation data was reported in the literature. Thus, no comparison is made here.

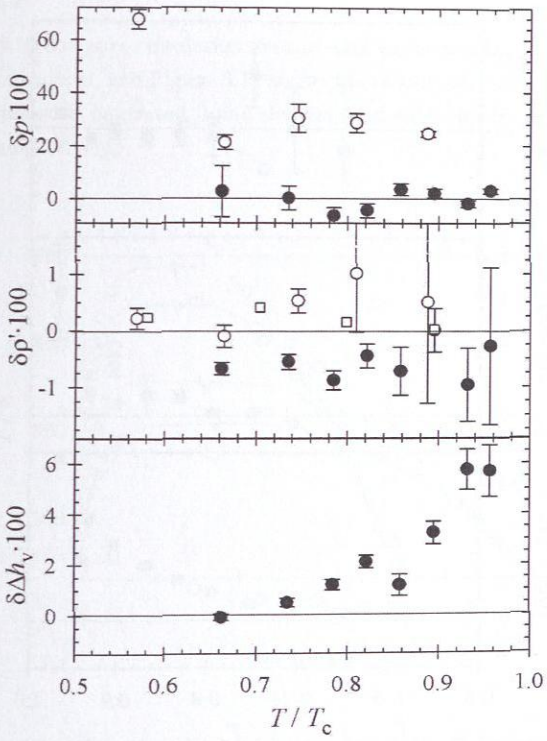

Figure 3.6: Relative deviations of VLE properties between simulation data and correlations of experimental data [105] ($\delta z = (z_{\text{sim}} - z_{\text{exp}})/z_{\text{exp}}$) for iso-butane: ● present model, ○ Martin and Siepmann [121], □ Nath and de Pablo [142]. Top: vapor pressure, center: saturated liquid density, bottom: enthalpy of vaporization. Error bars indicate simulation uncertainties, if given in the literature.

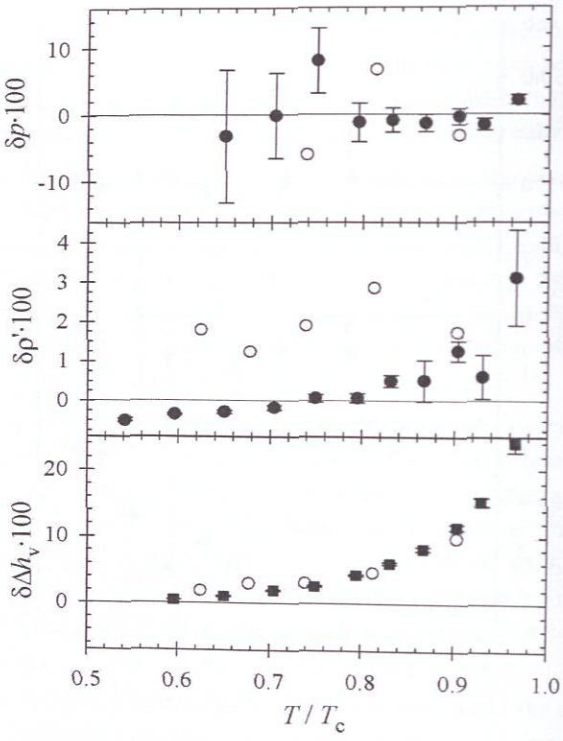

Figure 3.7: Relative deviations of VLE properties between simulation data and correlations of experimental data [165] ($\delta z = (z_{sim} - z_{exp})/z_{exp}$) for cyclohexane: ● present model, ○ Bourasseau et al. [10]. Top: vapor pressure, center: saturated liquid density, bottom: enthalpy of vaporization. Error bars indicate simulation uncertainties, if given in the literature.

3.4.2 Formaldehyde and Dimethyl Ether

The present molecular model for formaldehyde consists of two LJ sites, one for the oxygen atom and one for the methylene group, as well as one dipole. The dipole is located in the center of mass and its magnitude was specified according to QM results, cf. Table 3.1. All four LJ parameters are adjusted to experimental VLE data and are given in Table 3.1.

Figures 3.8 to 3.10 compare simulation results and experimental VLE data for formaldehyde, cf. Appendix B, and Figure 3.11 shows the relative deviations. Mean unsigned errors in vapor pressure, saturated liquid density, and enthalpy of vaporization are 4.3, 0.9, and 8.4 %, respectively.

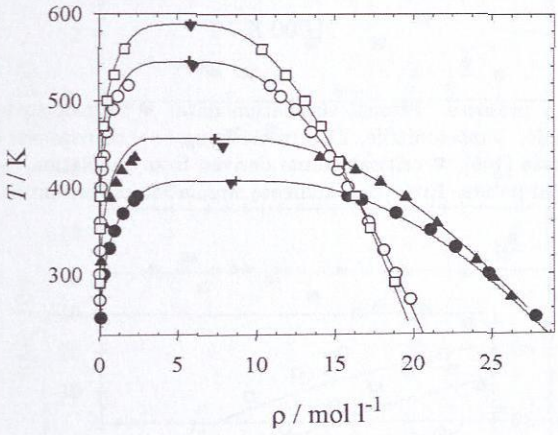

Figure 3.8: Saturated densities. Present simulation data: ● formaldehyde, ▲ hydrogen cyanide, ○ acetonitrile, □ nitromethane. — correlations of experimental data [165], ▼ critical points derived from simulation, + experimental critical points. Simulation uncertainties are within symbol size.

Note that, in contrast to iso-butane or cyclohexane, the available experimental data base is very weak here. In fact, for vapor pressure only a single data set from the year 1935 [183] is available. For saturated liquid density and enthalpy of vaporization, respectively, a single data point at 254 K is "accepted" by the DIPPR database [165]. Thus, no further optimization of the molecular model is attempted although the desired quality seems not to be fully reached. Hermida-Ramón and Ríos [63] published a molecular model based on QM calculations of formaldehyde dimers and trimers. They applied their

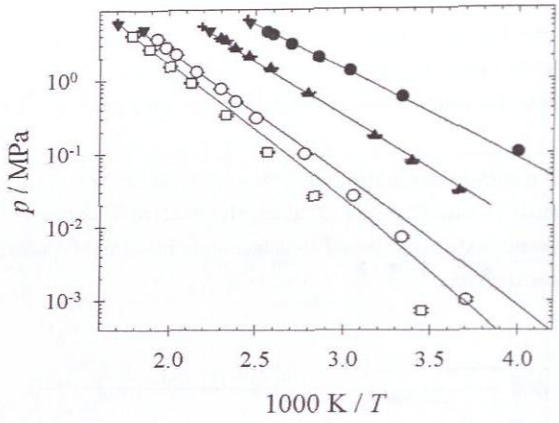

Figure 3.9: Vapor pressure. Present simulation data: ● formaldehyde, ▲ hydrogen cyanide, ○ acetonitrile, □ nitromethane. — correlations of experimental data [165], ▼ critical points derived from simulation, + experimental critical points. Error bars indicate simulation uncertainties.

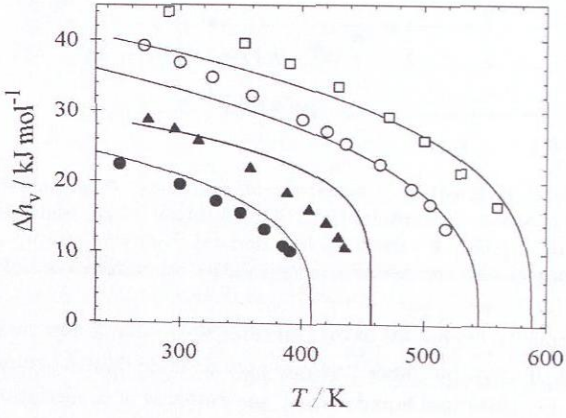

Figure 3.10: Enthalpy of vaporization. Present simulation data: ● formaldehyde, ▲ hydrogen cyanide, ○ acetonitrile, □ nitromethane. — correlations of experimental data [165]. Simulation uncertainties are within symbol size.

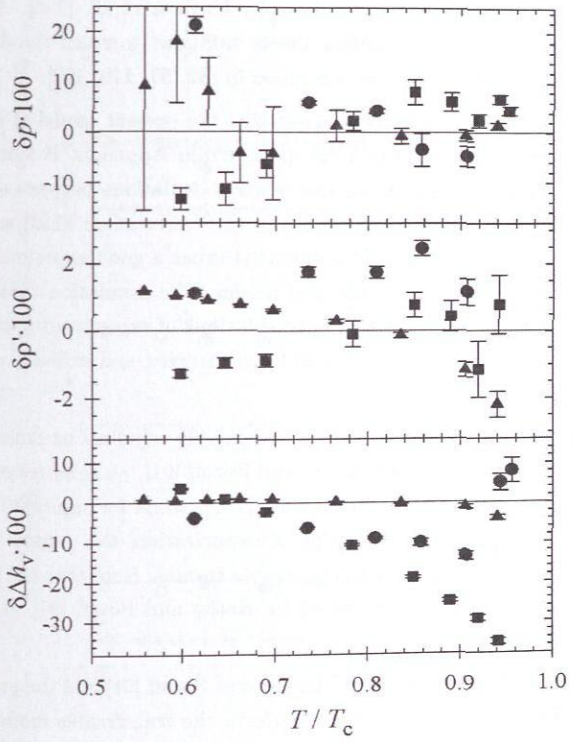

Figure 3.11: Relative deviations of VLE properties between simulation data and correlations of experimental data [165] ($\delta z = (z_{\text{sim}} - z_{\text{exp}})/z_{\text{exp}}$) for present models: ● formaldehyde, □ hydrogen cyanide, ▲ sulfur dioxide. Top: vapor pressure, center: saturated liquid density, bottom: enthalpy of vaporization. Error bars indicate simulation uncertainties.

model to liquid phase simulations but reported no results on VLE properties. Thus, no comparison was done here.

Dimethyl ether is modeled with three LJ sites in the present work, one for the oxygen atom and one for each methyl group. A dipole is located in the center of mass and oriented along the symmetry axis of the molecule, where the dipole moment is again taken from QM. For an initial model, the same LJ parameters of the methyl group are taken as for the iso-butane model, i.e. those by Ungerer et al. [208]. An adjustment of the two LJ parameters of the oxygen site is sufficient to reach the desired quality. Alternative models for dimethyl ether are given in [82, 91, 110, 192].

Figures 3.3 to 3.5 show the simulation results for the present model of dimethyl ether in comparison to the experimental VLE data, while Appendix B summarizes them in numerical form. Figure 3.12 shows the relative deviations between simulation and experiment also including simulation results from Stubbs et al. [192] and very recent results from Ketko and Potoff [91]. For dimethyl ether a good experimental data base is available for optimization of the molecular model. The simulation data of the present model is in very good agreement with the correlations of experimental data. The mean unsigned errors in vapor pressure, saturated liquid density, and enthalpy of vaporization are 2.6, 0.4, and 1.0 %, respectively.

For vapor pressure, both molecular models specifically adjusted to dimethyl ether, i.e. the present model and the model by Ketko and Potoff [91], yield better results than the transferable molecular model by Stubbs et al. [192], while for saturated liquid density all models perform similarly. For enthalpy of vaporization, the present model and the model by Ketko and Potoff also yield comparable results. Note that the parameters for the electrostatic interactions of the model by Ketko and Potoff [91] were adjusted to experimental VLE data as well.

It can be summarized that the model by Ketko and Potoff [91] and the present dimethyl ether model are of similar quality and outperform the transferable model by Stubbs et al. [192]. While Ketko and Potoff [91] adjusted four LJ parameters and the point charge magnitudes for their electrostatic interactions, following the proposed modeling strategy an optimization of only two LJ parameters is sufficient to reach the same quality.

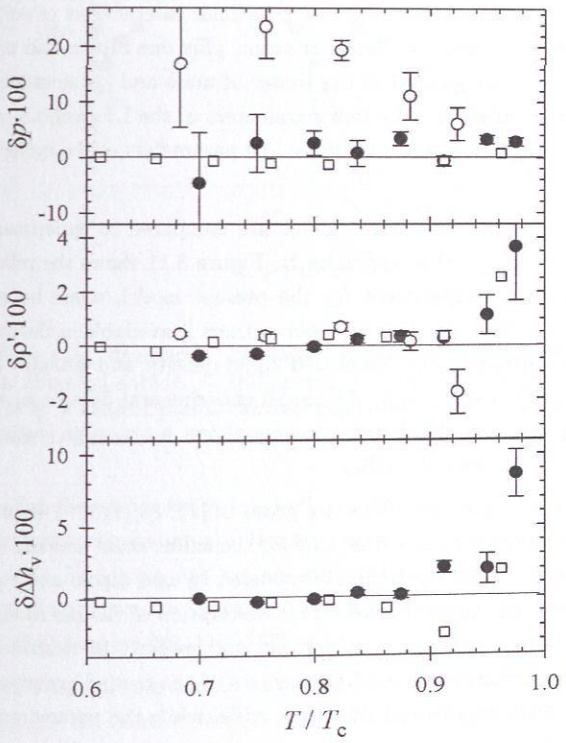

Figure 3.12: Relative deviations of VLE properties between *simulation* data and correlations of experimental data [165] ($\delta z = (z_{sim} - z_{exp})/z_{exp}$) for dimethyl ether: ● present model, ○ Stubbs et al. [192], □ Ketko and Potoff [91]. Top: vapor pressure, center: saturated liquid density, bottom: enthalpy of vaporization. Error bars indicate simulation uncertainties, if given in the literature.

3.4.3 Sulfur Dioxide, Dimethyl Sulfide, and Thiophene

For sulfur dioxide, a molecular model was published by Sokolić et al. [180, 181] which was optimized to total energy and pressure in the liquid state. It was recently reviewed by Ribeiro [163]. Alternatively, the commercial force field COMPASS [232] reports parameters for sulfur dioxide.

For the present molecular model, the intermolecular interactions of sulfur dioxide are modeled with three LJ sites, i.e. one per atom, plus one dipole and one quadrupole. The electrostatic sites are located in the center of mass and parametrized according to the results of QM calculation. The four parameters of the LJ sites, i.e. σ_S, ε_S, σ_O, and ε_O, are adjusted to experimental VLE data. All parameters of the molecular model are given in Table 3.1.

Present simulation results for sulfur dioxide are compared to experimental VLE data in Figures 3.13 to 3.15, cf. also Appendix B. Figure 3.11 shows the relative deviations between simulation and experiment for the present model, while no numerical VLE simulation data for sulfur dioxide from other authors is available in the literature. Mean unsigned errors in vapor pressure, saturated liquid density, and enthalpy of vaporization are 4.0, 0.9, and 1.6 %, respectively. The good experimental data base, with more than 60 individual experimental VLE data points, allows a thorough optimization of the molecular model to the desired quality.

Literature models for dimethyl sulfide are given in [25, 83, 115]. The present dimethyl sulfide model consists of three LJ sites, one for the sulfur atom and one for each methyl group. The electrostatic interactions are modeled by one dipole and two quadrupoles oriented perpendicularly to each other. This description of the electrostatics is chosen, as QM yields a charge distribution, which can not properly be described with a lower number of electrostatic sites. The LJ parameters of the methyl groups are assumed to be the same as for iso-butane and dimethyl oxide, while the parameters of the sulfide are adjusted to experimental VLE data.

Figures 3.13 to 3.15 show the present simulation results for dimethyl sulfide in comparison to experimental VLE data, while numerical results are given in Appendix B. Figure 3.16 shows the relative deviations between simulation and experiment for the present model and for the model of Lubna et al. [115]. Note that simulation results on enthalpy of vaporization were not included in [115]. For the present model of dimethyl sulfide, mean unsigned errors in vapor pressure, saturated liquid density, and enthalpy of vaporization are 4.0, 0.7, and 3.8 %, respectively. Particularly the vapor pressure is better described than by the model of Lubna et al.

Also thiophene is described in the present work by a rigid model in its most stable conformation, as for cyclohexane. Five LJ sites, one for each of the four methylene

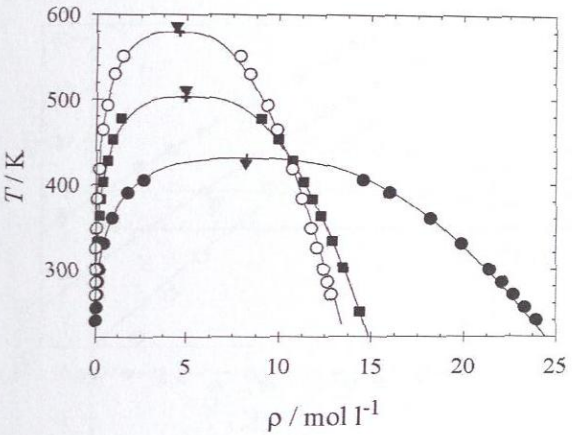

Figure 3.13: Saturated densities. Present simulation data: ● sulfur dioxide, ▲ dimethyl sulfide, ○ thiophene. — correlations of experimental data [165], ▼ critical points derived from simulation, + experimental critical points. Simulation uncertainties are within symbol size.

groups and one for the sulfur atom, as well as one dipole and one quadrupole are used. The electrostatic parameters are directly passed on from QM. A total of four LJ parameters, i.e. σ_{CH2}, ε_{CH2}, σ_S, and ε_S, are adjusted to experimental VLE data. The optimized parameters are given in Table 3.1. Alternative molecular models for thiophene can be found in the literature [89, 115, 157]

Figures 3.13 to 3.15 compare simulation results to experimental VLE data for thiophene, cf. Appendix B, while the relative deviations are shown in Figure 3.17. In the deviation plot also simulation results from Lubna et al. [115], Juárez-Guerra et al. [89], and Pérez-Pellitero et al. [157] are included. Mean unsigned errors of the present model in vapor pressure, saturated liquid density, and enthalpy of vaporization are 3.8, 1.2, and 3.2 %, respectively.

The thiophene model by Juárez-Guerra et al. [89] shows significant deviations in both vapor pressure and saturated liquid density while no simulation results for the enthalpy of vaporization were given by the authors. The anisotropic united atoms (AUA) potential by Pérez-Pellitero et al. [157] overpredicts the vapor pressure over the complete temperature range by up to 20 %. Simulation results for saturated liquid density and enthalpy of vaporization are in very good agreement with the DIPPR correlation for low temperatures but give noticeably higher values than the DIPPR correlation for

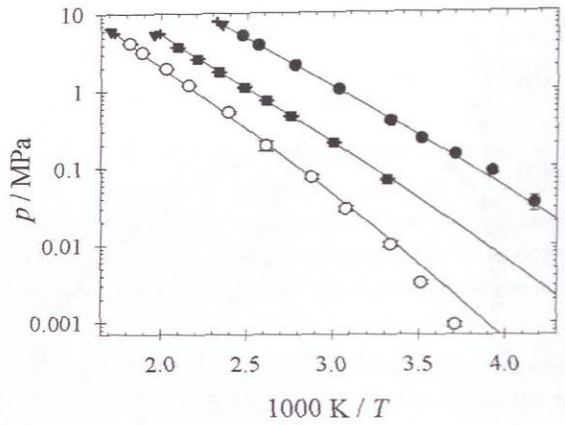

Figure 3.14: Vapor pressure. Present simulation data: ● sulfur dioxide, ▲ dimethyl sulfide, ○ thiophene. — correlations of experimental data [165], ▼ critical points derived from simulation, + experimental critical points. Error bars indicate simulation uncertainties.

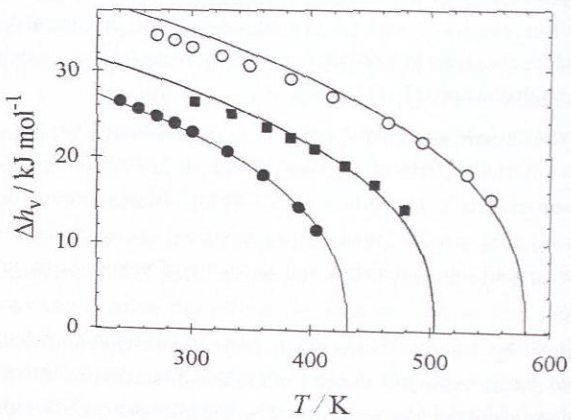

Figure 3.15: Enthalpy of vaporization. Present simulation data: ● sulfur dioxide, ▲ dimethyl sulfide, ○ thiophene. — correlations of experimental data [165]. Simulation uncertainties are within symbol size.

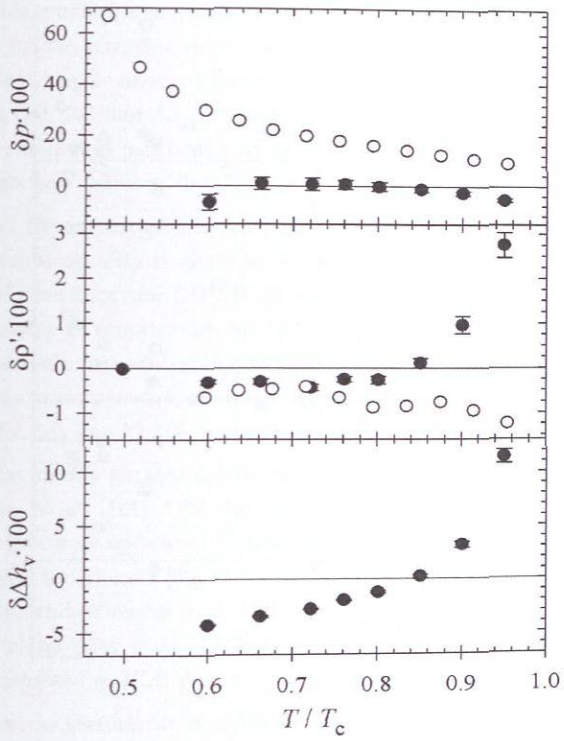

Figure 3.16: Relative deviations of VLE properties between simulation data and correlations of experimental data [165] ($\delta z = (z_{\text{sim}} - z_{\text{exp}})/z_{\text{exp}}$) for dimethyl sulfide: ● present model, ○ Lubna et al. [115]. Top: vapor pressure, center: saturated liquid density, bottom: enthalpy of vaporization. Error bars indicate simulation uncertainties, if given in the literature.

temperatures above 0.7 T_c. Finally, the TraPPE force field by Lubna et al. [115] yields vapor pressure results that agree well with the DIPPR correlation and the simulation results from the present model considering their scatter. However, saturated densities are higher than the correlation towards the critical point as for the other three molecular models regarded here. For enthalpy of vaporization, no numerical data were given by Lubna et al.

It should be noted that for thiophene experimental vapor pressure data is available for temperatures up to around 0.9 T_c, experimental saturated liquid densities and enthalpies

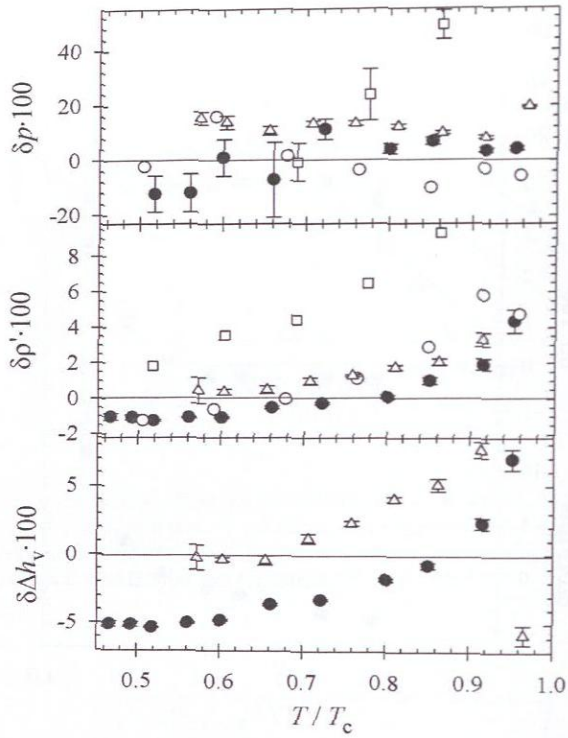

Figure 3.17: Relative deviations of VLE properties between simulation data and correlations of experimental data [165] ($\delta z = (z_{\text{sim}} - z_{\text{exp}})/z_{\text{exp}}$) for thiophene: ● present model, ○ Lubna et al. [115], □ Juárez-Guerra et al. [89], △ Pérez-Pellitero et al. [157]. Top: vapor pressure, center: saturated liquid density, bottom: enthalpy of vaporization. Error bars indicate simulation uncertainties, if given in the literature.

of vaporization are only available up to approximately 0.63 T_c. Thus, an assessment of the different molecular models regarding density and enthalpy of vaporization above 0.7 T_c on the basis of the DIPPR correlations is questionable.

3.4.4 Hydrogen Cyanide, Acetonitrile, and Nitromethane

Hydrogen cyanide is modeled in the present work with two LJ sites, one for the methine group and one for the nitrogen atom. Electrostatic interactions are modeled by one dipole and one quadrupole oriented along the symmetry axis, where the parameters are passed on from QM. All four LJ parameters are adjusted to experimental VLE data. The optimized parameters can be found in Table 3.1. For hydrogen cyanide no other molecular models were found in the literature.

Figures 3.13 to 3.15 compare simulation results and experimental VLE data for hydrogen cyanide. Numerical data is given in Appendix B. Figure 3.11 shows the relative deviations. Unfortunately, the DIPPR database [165] contains no true experimental data on the enthalpy of vaporization for hydrogen cyanide. Consequently, in the optimization process, only minor attention is paid to the enthalpy of vaporization. Mean unsigned errors in vapor pressure, saturated liquid density, and enthalpy of vaporization are nominally 7.2, 1.0, and 12.2 %, respectively.

Several molecular models for acetonitrile are available in the literature. Jorgensen and Briggs [84], Price et al. [161], Guárdia et al. [59], and Nikitin and Lyubartsev [149] present models that were optimized to the liquid density and enthalpy of vaporization at 293 K. Hloucha and Deiters [69] give a polarizable molecular model for simulations in the liquid state while Hloucha et al. [70] published a model that is based on *ab initio* calculations. Finally, Wick et al. [227] proposed an extension of their TraPPE force field that was optimized to VLE data to cover acetonitrile.

In the present work, acetonitrile is modeled using three LJ sites, one for the methyl group, one for the central carbon atom, and one for the nitrogen atom. The electrostatic interactions are modeled by one dipole and one quadrupole, located in the center of mass and parametrized strictly according to QM results. The parameters of the LJ sites of the methyl group and the nitrogen atom are adjusted to experimental VLE data. The LJ parameters of the central carbon atom are taken from unpublished work on carbon dioxide and excluded from optimization, as only a very weak sensitivity of the VLE simulation results on these parameters is found. All parameters of the molecular model are given in Table 3.1.

Simulation results for acetonitrile are compared to experimental VLE data Figures 3.8 to 3.10 and in Appendix B. The relative deviations between simulation and experiment are shown in Figure 3.18 besides results of the OPLS-UA force field by Jorgensen and Briggs [84] and the TraPPE force field by Wick et al., which were reported for both models in [227]. Despite the good experimental data base, the desired quality is not achieved by the present optimization. Only a fair description of the experimental VLE is reached. Mean unsigned errors in vapor pressure, saturated liquid density, and enthalpy

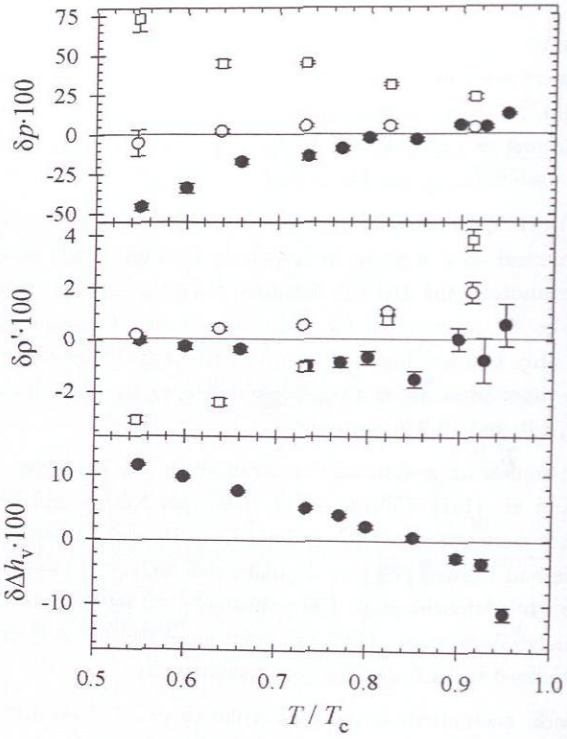

Figure 3.18: Relative deviations of VLE properties between simulation data and correlations of experimental data [165] ($\delta z = (z_{\text{sim}} - z_{\text{exp}})/z_{\text{exp}}$) for acetonitrile: ● present model, ○ Wick et al. [227], □ Jorgensen and Briggs [84, 227]. Top: vapor pressure, center: saturated liquid density, bottom: enthalpy of vaporization. Error bars indicate simulation uncertainties, if given in the literature.

of vaporization are 19.7, 0.9, and 5.4 %, respectively.

The large relative deviations in vapor pressure are a consquence of systematic underestimations at low temperatures. In this region also difficulties are encountered in the simulative calculation of the chemical potential in the liquid phase to determine the phase equilibrium. This is even the case when the more sophisticated gradual insertion method [212] is used, as described in Section 2.3.2.

The OPLS-UA force field by Jorgensen and Briggs [84] significantly overestimates the

vapor pressure of acetonitrile and shows deviations in the saturated liquid density up to 4 %, cf. Figure 3.18. Simulation results for vapor pressure obtained with the TraPPE force field by Wick et al. [227] show a very good agreement with the DIPPR correlation, while the saturated liquid density is slightly overpredicted towards the critical point. No comparison of the literature models for acetonitrile is possible regarding the enthalpy of vaporization due to the lack of numerical simulation results.

The present molecular model for nitromethane consists of four LJ sites, one for the methyl group, one for the nitrogen atom, and one for the two oxygen atoms each. The electrostatic interactions are modeled by one dipole and one quadrupole oriented along the symmetry axis, where the parameters are specified according to QM results. All six LJ parameters are adjusted to experimental VLE data. Alternative models are available in the literature [4, 161, 182, 227].

Figures 3.13 to 3.15 compare the present simulation results for nitromethane with experimental VLE data, cf. Appendix B. Figure 3.19 shows the relative deviations obtained with the present model, the OPLS-AA force field by Price et al. [161], and the TraPPE force field by Wick et al. [227]. For the present model of nitromethane, mean unsigned errors in vapor pressure, saturated liquid density, and enthalpy of vaporization are 18.7, 0.2, and 7.0 %, respectively. Again, a systematic underprediction of the vapor pressure at low temperatures is found, leading to the high relative deviations, as for acetonitrile.

The OPLS-AA force field [161] overpredicts the vapor pressure by about 100 % and underpredicts the saturated liquid density by up to 6 %. The TraPPE force field of Wick et al. [227] that was optimized to experimental VLE data, yields very good results in vapor pressure for low temperatures while the result for the highest simulated temperature deviates by +34 % from the DIPPR correlation. Regarding saturated liquid density, strong scatter and large statistical uncertainties of the simulation results are observed for both literature models.

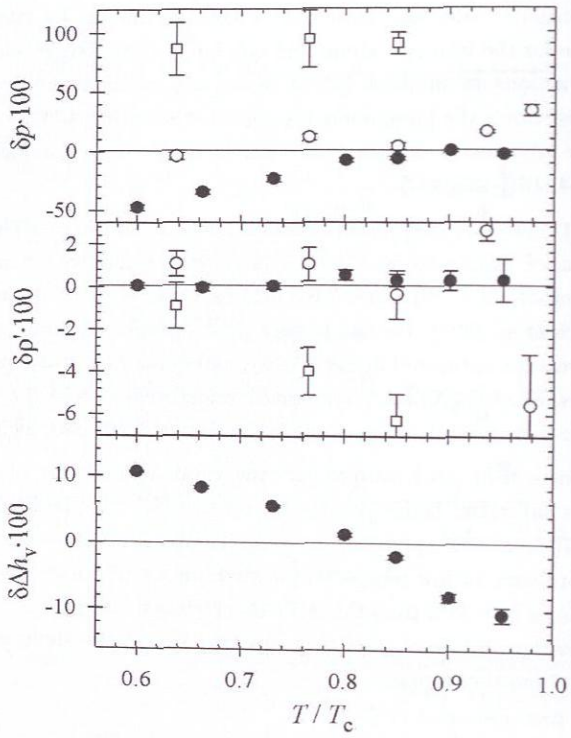

Figure 3.19: Relative deviations of VLE properties between simulation data and correlations of experimental data [165] ($\delta z = (z_{\text{sim}} - z_{\text{exp}})/z_{\text{exp}}$) for nitromethane: ● present model, ○ Wick et al. [227], □ Price et al. [161]. Top: vapor pressure, center: saturated liquid density, bottom: enthalpy of vaporization. Error bars indicate simulation uncertainties, if given in the literature.

3.5 Other Molecular Models

The applicability of the proposed modeling strategy was shown in the previous section. In this section, it is applied to develop molecular models for ammonia, ethylene oxide, and heptafluoropropane (R227ea). These models are subsequently used for the prediction of different thermophysical properties as described in Chapter 4.

3.5.1 Ammonia

Different approaches can be found in the literature to construct an intermolecular potential for ammonia to be used in molecular simulation. Jorgensen and Ibrahim [86] as well as Hinchliffe et al. [66] used experimental bond distances and angles to locate their interaction sites. Jorgensen and Ibrahim [86] fitted a 12-6-3 potential plus four partial charges to results from *ab initio* QM calculations they derived from 250 mutual orientations of the ammonia dimer using the STO-3G minimal basis set. To yield reasonable potential energies for liquid ammonia compared to experimental results, they had to scale their potential by a factor of 1.26.

Hinchliffe et al. [66] used a combination of exponential repulsion terms, an attractive Morse potential, and four partial charges to construct their intermolecular potential. The parameters were determined by fitting to a total of 61 points on the ammonia dimer energy surface at seven different orientations, which were calculated by QM using the 6-31G* basis set. Hinchliffe et al. have pointed out that the parametrization is ambiguous concerning the selection of dimer configurations and the utilized interaction potentials. Also the different models perform differently well on various properties.

In a later work, Impey and Klein [77] reparametrized the molecular model by Hinchliffe et al. [66]. They switched to an "effective" pair potential using one LJ site at the nitrogen nucleus position to describe the dispersive and repulsive interactions. The parameters were optimized to the radial distribution function g_{N-N} of liquid ammonia measured by Narten [139].

Kristóf et al. [99] used this model to predict VLE properties and found systematic deviations in both vapor pressure and saturated densities. So they decided to develop a completely new molecular model. Again, they used experimental bond distances and angles to locate the interaction sites. All further parameters of their model, i.e. the partial charges on all atoms and the parameters of the single LJ potential, were adjusted to vapor-liquid coexistence properties. With this model, Kristóf et al. reached a description of the VLE of ammonia of reasonable accuracy.

For their simulations, Kristóf et al. used the Gibbs ensemble Monte Carlo (GEMC) technique [154, 155] with an extension to the NpH ensemble [97, 98]. This method has

some difficulties simulating strongly interacting fluids, yielding relatively large statistical uncertainties.

The VLE of ammonia, as modeled by Kristóf et al. [99], is also simulated in the present work applying the methods gradual insertion and Grand Equilibrium, cf. Sections 2.3.2 and 2.4. Leading to much smaller statistical errors, results slightly outside the error bars of Kristóf et al. are obtained. Also systematic deviations to the experimental VLE properties are found, especially in the vapor pressure and critical temperature, cf. Figures 3.20 to 3.22.

In the present work, a new molecular model for ammonia is proposed [30]. This model is based on the work of Kristóf et al. [99], which is improved by including data on geometry and electrostatics from *ab initio* QM calculations. This *preliminary model* uses the LJ parameters by Kristóf et al., which are then adjusted to experimental VLE data until a desired quality is reached. The resulting model, denoted as *new model* in the following, is used subsequently to predict thermophysical properties apart from the phase coexistence curves, cf. Section 4.2.

For both present models, a single LJ site is used to describe the dispersive and repulsive interactions. The electrostatic interactions as well as hydrogen bonding are modeled by a total of four partial charges located at the nuclei positions obtained from QM. The parameters of the molecular models for ammonia are listed in Table 3.3.

VLE results for the new model are compared to data obtained from a reference quality EOS [202] in Figures 3.20 to 3.22. These figures also include the results from the preliminary model and the model of Kristóf et al. [99]. The present numerical simulation results together with experimental data [202] are given in Appendix B. Technical simulation details are given in Appendix A.

The reference EOS [202] used for adjustment and comparison here, was optimized to a set of 1147 experimental data points. It is based on two older EOS from the late 1970s [2, 61] and is recommended by the National Institute of Standards and Technologies (NIST) within their reference EOS database REFPROP [105]. The estimated uncertainties of the EOS are 0.2 % in density, 2 % in heat capacity, and 2 % in the speed of sound, except in the critical region. The uncertainty in vapor pressure is 0.2 %.

The model of Kristóf et al. [99] shows noticeable deviations from experimental data. The mean unsigned errors over the VLE range are 1.9 % in saturated liquid density, 13 % in vapor pressure and 5.1 % in enthalpy of vaporization. Even without any further adjustment to experimental data, a better description is found using the preliminary model. The deviations between simulation results and reference EOS are 1.5 % in saturated liquid density, 10.4 % in vapor pressure and 5.1 % in enthalpy of vaporization.

With the new model a significant improvement is achieved compared to the model

Table 3.3: Parameters of the molecular models for ammonia.

Interaction Site	x Å	y Å	z Å	σ Å	ε/k_B K	q e
preliminary model						
N	0	0	0.0757	3.385	170.00	-0.9993
H(1)	0.9347	0	-0.3164	—	—	0.3331
H(2)	-0.4673	0.8095	-0.3164	—	—	0.3331
H(3)	-0.4673	-0.8095	-0.3164	—	—	0.3331
new model						
N	0	0	0.0757	3.376	182.90	-0.9993
H(1)	0.9347	0	-0.3164	—	—	0.3331
H(2)	-0.4673	0.8095	-0.3164	—	—	0.3331
H(3)	-0.4673	-0.8095	-0.3164	—	—	0.3331

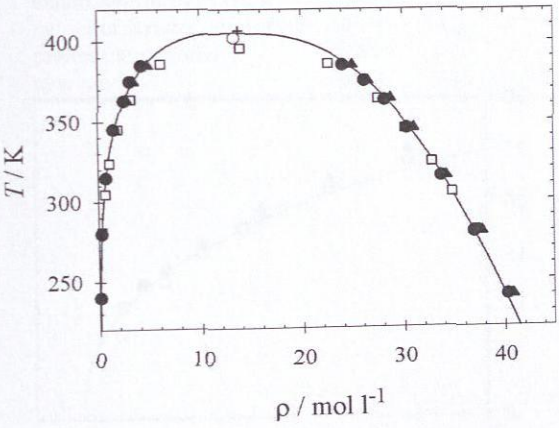

Figure 3.20: Saturated densities of ammonia. Present simulation data: ● new model, □ model of Kristóf et al. [99], ▲ preliminary model. — reference EOS [202]. Critical points derived from simulation: ○ new model, □ model of Kristóf et al. + experimental critical point [123]. Simulation uncertainties are within symbol size.

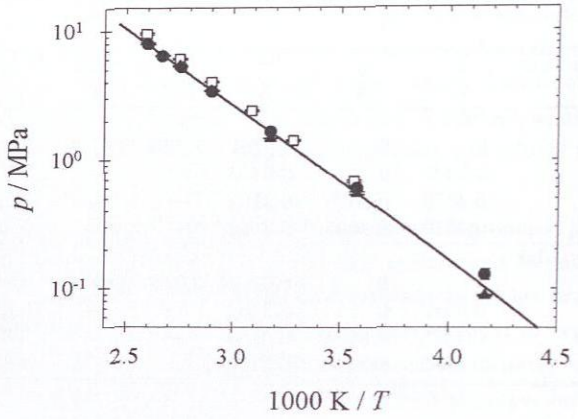

Figure 3.21: Vapor pressure of ammonia. Present simulation data: ● new model, □ model of Kristóf et al. [99], ▲ preliminary model. — reference EOS [202]. Error bars indicate simulation uncertainties.

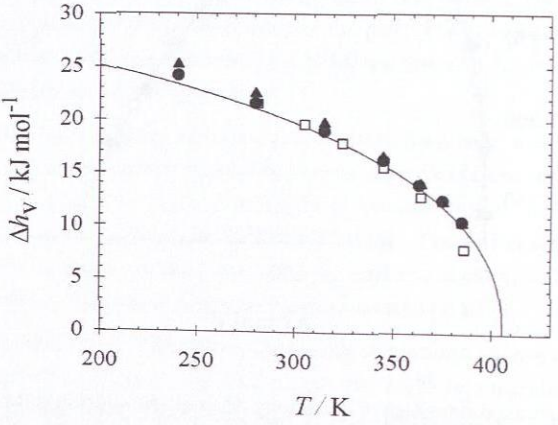

Figure 3.22: Enthalpy of vaporization of ammonia. Present simulation data: ● new model, □ model of Kristóf et al. [99], ▲ preliminary model. — reference EOS [202]. Simulation uncertainties are within symbol size.

of Kristóf et al. [99]. The description of the experimental VLE is very good, the mean unsigned deviations in saturated liquid density, vapor pressure and enthalpy of vaporization are 0.7, 1.6, and 2.7 %, respectively. Only at low temperatures, in the range of ambient pressure, a slightly worse description of the vapor pressure compared to the preliminary model is observed. In Figure 3.23 the relative deviations of the new model, the model of Kristóf et al., and the preliminary model are shown in the whole range of the VLE from triple point to critical point.

Mathews [123] gives experimental critical values of temperature, density and pressure for ammonia. In Table 3.4 these values are compared to the results obtained from simulation following the procedure suggested by Lotfi et al. [114]. The model of Kristóf et al. [99] underpredicts the critical temperature by 2.4 %. The latter two models give reasonable results for the critical temperature, while the new model underpredicts the critical pressure slightly.

Table 3.4: Critical data of ammonia. Experimental data compared to results from molecular models.

	T_c K	ρ_c mol/l	p_c MPa
experimental data [123]	406.65	13.8	11.28
model of Kristóf et al. [99]	395.82	14.0	11.26
preliminary model	403.99	14.1	11.67
new model	402.21	13.4	10.52

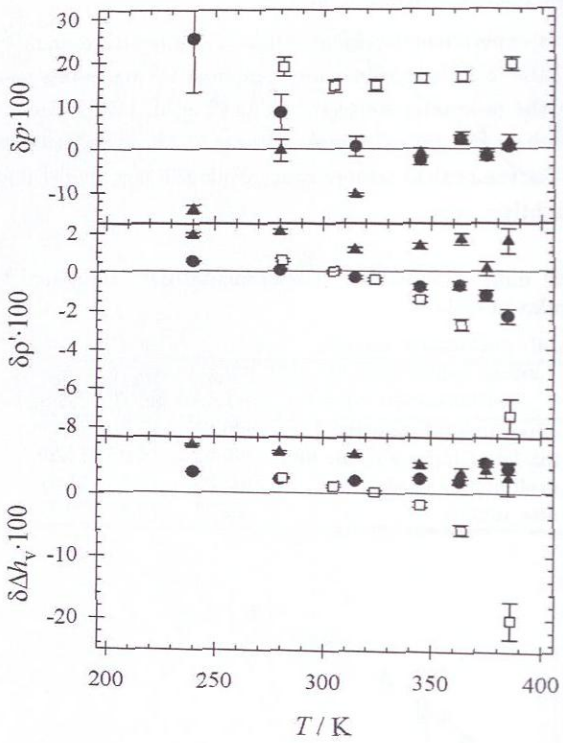

Figure 3.23: Relative deviations of VLE properties between simulation and reference EOS [202] ($\delta z = (z_{\text{sim}} - z_{\text{eos}})/z_{\text{eos}}$) for ammonia: ● new model, □ model of Kristóf et al. [99], ▲ preliminary model. Top: vapor pressure, center: saturated liquid density, bottom: enthalpy of vaporization. Error bars indicate simulation uncertainties.

3.5.2 Ethylene Oxide

In the present work, a new molecular model for ethylene oxide is developed [29]. This model is based on prior work of Stoll [186] and is further optimized to experimental VLE data, i.e. saturated liquid density, vapor pressure, and enthalpy of vaporization. The present model consists of three LJ sites (one for each methylene group and one for the oxygen atom) plus one static point dipole. Again, the united-atom approach is used and due to the fact that ethylene oxide is a small molecule, the internal degrees of freedom may be neglected and the model was assumed to be rigid. Here, experimental data on the molecular structure [117] is used to specify the location of the LJ sites, as this was done by Stoll [186].

A set of five adjustable parameters, i.e. the four LJ parameters σ_{CH2}, ε_{CH2}, σ_O, ε_O, and the dipole moment μ, is optimized. Correlations of experimental data are taken from the DIPPR database [165]. For ethylene oxide the correlations to saturated liquid density and vapor pressure are based on real experimental data points from 222 to 461 K and 213 to 469 K, respectively. Note that the correlation of the enthalpy of vaporization is based on three experimental data points in the range from 284 to 298 K only. Additionally, data points for enthalpy of vaporization come from predictions by various authors, mostly based on the Clausius-Clapeyron equation. Nevertheless, the DIPPR correlations are used as they are assumed as best practice. The saturated vapor density of ethylene oxide is calculated from the correlations for saturated liquid density, vapor pressure, and enthalpy of vaporization using the Clausius-Clapeyron equation. This data is only used in some figures here, but is not included in the model optimization process.

Following the optimization procedure presented in Section 3.3, an optimized paramet set is obtained after three iteration cycles. The geometry of the optimized model shown in Figure 3.24, while the model parameters are listed in Table 3.5.

In Figures 3.25 to 3.27, saturated densities, vapor pressure, and enthalpy of vaporization are shown for the present ethylene oxide model. In these figures also results are included, which are obtained with the molecular model for ethylene oxide proposed by Wielopolski and Smith [230]. Numerical simulation results for the VLE from both models are given in Appendix B.

The mean unsigned errors of the present model, i.e. the relative deviation from experimental data in vapor pressure, saturated liquid density, and enthalpy of vaporization, are 1.5, 0.4, and 1.8 %, respectively, cf. Figure 3.28. Please note that simulation data obtained with the model of Wielopolski and Smith are not included in Figure 3.28 as they are not within scale.

Individual VLE simulation results from the present model between 235 and 445 K deviate by less than 3 % in vapor pressure and heat of vaporization, and less than 0.5 % in

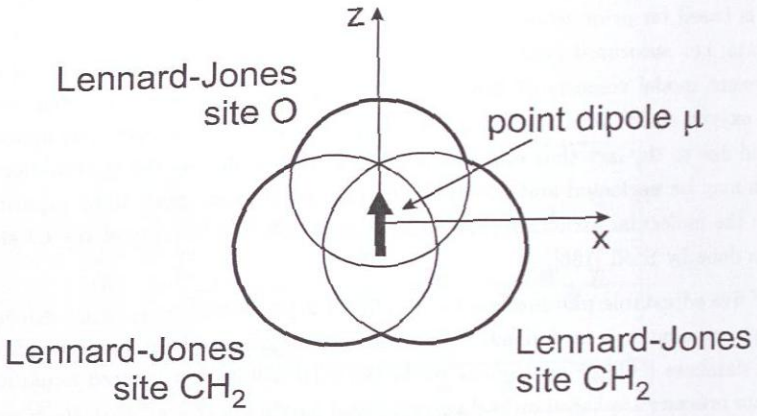

Figure 3.24: Geometry of the present model for ethylene oxide. Note that all sites of the present model are within the x-z-plane.

Table 3.5: Coordinates and parameters of the present molecular model for ethylene oxide. The three LJ sites are denoted by the molecular group which they represent, while the single dipolar site is denoted by dipole. All coordinates are in principal axes with respect to the center of mass. The orientation of the electrostatic site is defined in standard Euler angles, where φ is the azimuthal angle with respect to the x-y-plane and θ is the inclination angle with respect to the z-axis.

Interaction Site	x Å	y Å	z Å	σ Å	ε/k_B K	θ deg	φ deg	μ D
$CH_2(1)$	0.7800	0	-0.4843	3.527	84.74	—	—	—
$CH_2(2)$	-0.7800	0	-0.4843	3.527	84.74	—	—	—
O	0	0	0.7357	3.093	62.13	—	—	—
dipole	0	0	0	—	—	0	0	2.459

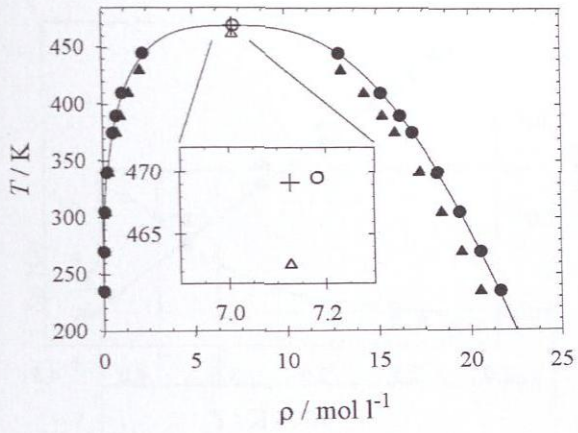

Figure 3.25: Saturated densities of ethylene oxide. Simulation data: ● present model, ▲ model of Wielopolski and Smith [230]. — Correlation of experimental data [165]. Critical points derived from simulation: ○ present model, △ model of Wielopolski and Smith. + experimental critical point [101]. Statistical uncertainties are within symbol size. The inset shows the critical region in greater detail.

saturated liquid density, cf. Figure 3.28. The only exception is the vapor pressure at the lowest simulated temperature, where the statistical uncertainty is large in relative terms (being 5 kPa in absolute terms).

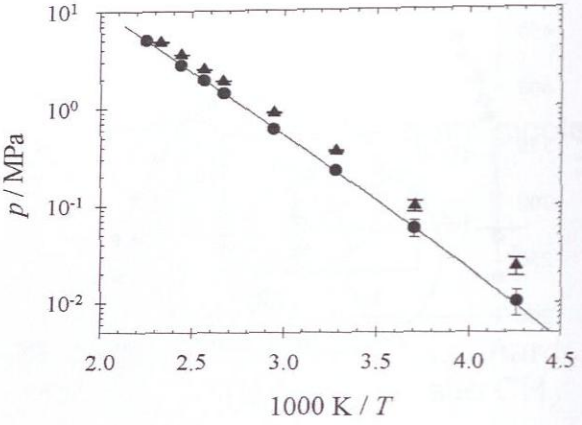

Figure 3.26: Vapor pressure of ethylene oxide. Simulation data: ● present model, ▲ model of Wielopolski and Smith [230]. — Correlation of experimental data [165]. Error bars indicate simulation uncertainties.

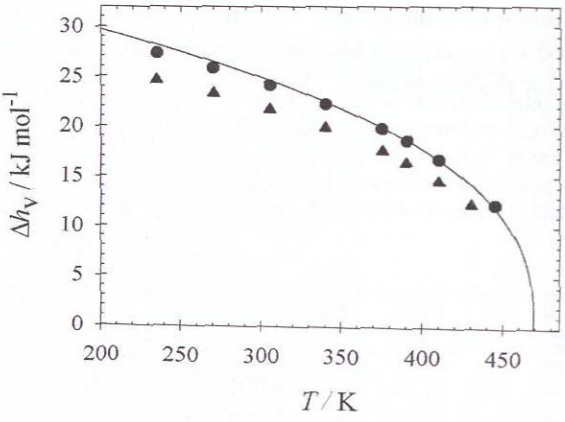

Figure 3.27: Enthalpy of vaporization of ethylene oxide. Simulation data: ● present model, ▲ model of Wielopolski and Smith [230]. — Correlation of experimental data [165]. Statistical uncertainties are within symbol size.

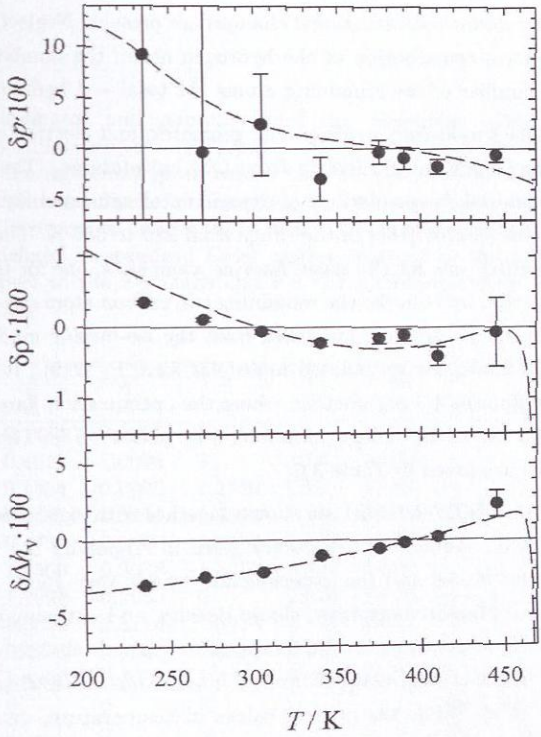

Figure 3.28: Relative deviations of VLE properties between simulation data and correlations of experimental data [165] ($\delta z = (z_{\text{sim}} - z_{\text{exp}})/z_{\text{exp}}$) for ethylene oxide: ● present model, – – fits of simulation data, *cf. Equations (4.2)* to (4.4). Top: vapor pressure, center: saturated liquid density, bottom: *enthalpy of vaporization*. Error bars indicate simulation uncertainties.

3.5.3 Heptaflouropropane (R227ea)

The new molecular model for 1,1,1,2,3,3,3-heptafluoropropane (R227ea, CF_3-CHF-CF_3) is developed based on QM calculations and optimized using experimental vapor pressure and saturated liquid density [27]. A rigid model with ten LJ sites plus one point dipole and one point quadrupole is chosen balancing between accuracy and simplicity of the model. The assumption of rigidity is reasonable due to the compact shape of the molecule, where only minor conformational changes are present. Neglecting the explicit repulsive and dispersive contribution of the hydrogen atom, the number of LJ sites is determined by the number of the remaining atoms (11 total − 1 hydrogen) here.

Following the proposed modeling strategy, the geometric and electrostatic parameters of the molecular model are taken directly from QM calculations. The parameters of the LJ sites are optimized to correlations of experimental saturated liquid density and vapor pressure of pure R227ea [165] in the range from 280 to 355 K. Three different LJ parameters sets are used: one for the seven fluorine atom sites, one for the united-atom methine (CH) group site, and one for the remaining two carbon atom sites. As a starting set for optimization, LJ parameters are taken from the iso-butane model, and for the fluorine sites from a model for its bonded molecular form F_2 [219]. It is sufficient to adjust only the two fluorine LJ parameters, where the optimization hardly changes the size parameter σ and varies the energy parameter ε by about +5 %. The parameters of the optimized model are listed in Table 3.6.

VLE data from the new R227ea model are shown together with experimental data [165] in Figures 3.29 to 3.31. Numerical results are given in Appendix B. The agreement between the molecular model and the experimental data is very good. The mean unsigned errors in vapor pressure, saturated liquid density, and enthalpy of vaporization are 1.1, 1.0, and 7.3 %, respectively, in the temperature range from 280 to 355 K, which is about 75 to 95 % of the critical temperature, cf. Figure 3.32. Following the procedure suggested by Lotfi et al. [114], the critical values of temperature, density and pressure are determined: T_c =375.22 (374.83) K, ρ_c =3.375 (3.650) mol/l, and p_c =2.833 (2.912) MPa. The numbers in parentheses are based upon experimental data and are taken from [138]. A good agreement for the critical properties is found, cf. Figures 3.29 and 3.30.

Table 3.6: Coordinates and parameters of the molecular model for 1,1,1,2,3,3,3-heptafluoropropane (R227ea). The ten LJ sites are denoted in boldface by the molecular group which they represent, while the electrostatic sites are denoted dipole and quadrupole. All coordinates are in principal axes with respect to the center of mass. The orientation of the electrostatic site is defined in standard Euler angles, where φ is the azimuthal angle with respect to the x-y-plane and θ is the inclination angle with respect to the z-axis.

Interaction Site	x Å	y Å	z Å	σ Å	ε/k_B K	θ deg	φ deg	μ D	Q B
C(1)	0.1434	-0.0095	-1.2789	2.81	10.64	—	—	—	—
C(2)-**H**	-0.4021	-1.0096	0	3.36	51.00	—	—	—	—
C(3)	0.1434	-0.0095	1.2789	2.81	10.64	—	—	—	—
F-C(1)	-0.0042	1.3214	-1.3514	2.826	54.79	—	—	—	—
F-C(1)	-0.4737	-0.5626	-2.3390	2.826	54.79	—	—	—	—
F-C(1)	1.4560	-0.3038	-1.3482	2.826	54.79	—	—	—	—
F-C(2)	-1.7998	-0.2655	0	2.826	54.79	—	—	—	—
F-C(3)	-0.0042	1.3214	1.3514	2.826	54.79	—	—	—	—
F-C(3)	-0.4739	-0.5626	2.3390	2.826	54.79	—	—	—	—
F-C(3)	1.4560	-0.3038	1.3482	2.826	54.79	—	—	—	—
dipole	0	0	0	—	—	90	278.48	2.209	—
quadrupole	0	0	0	—	—	90	8.48	—	6.440

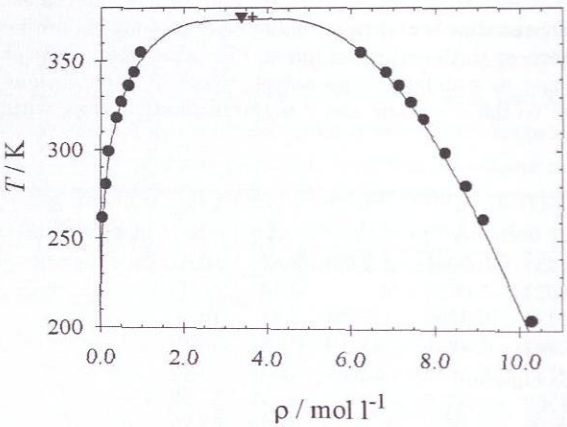

Figure 3.29: Saturated densities of R227ea: ● present simulation data, — correlation of experimental data [165], ▼ critical point derived from simulation data, △ experimental critical point [138]. Simulation uncertainties are within symbol size.

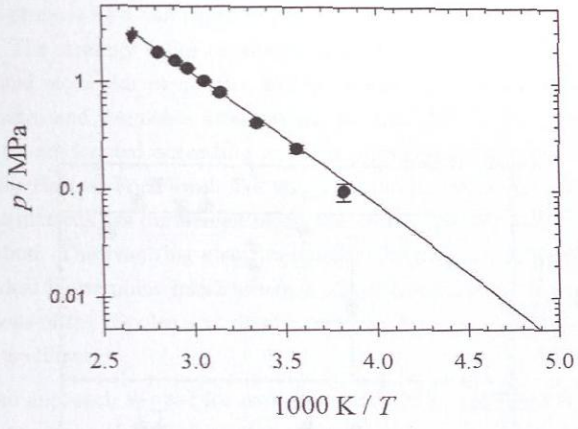

Figure 3.30: Vapor pressure of R227ea: ● present simulation data, — correlation of experimental data [165], ▼ critical point derived from simulation data, △ experimental critical point [138]. Error bars indicate simulation uncertainties.

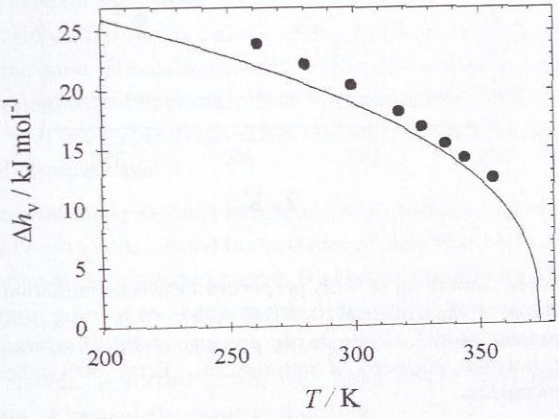

Figure 3.31: Enthalpy of vaporization of R227ea: ● present simulation data, — correlation of experimental data [165]. Simulation uncertainties are within symbol size.

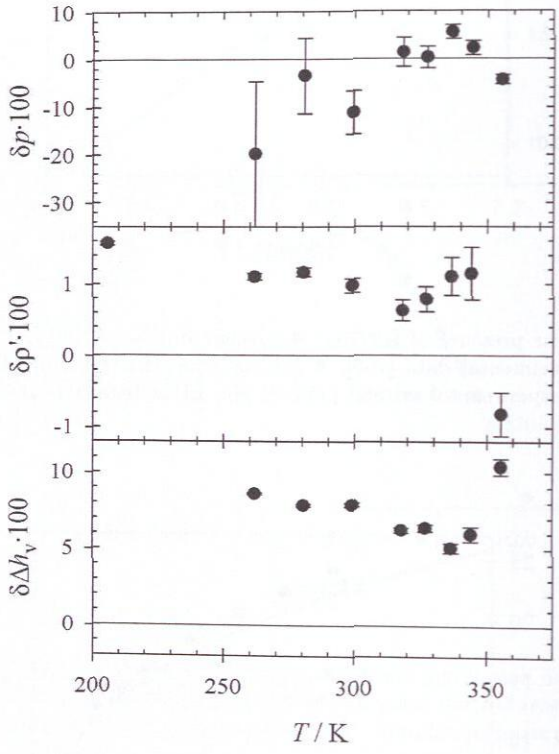

Figure 3.32: Relative deviations of VLE properties between simulation data and correlations of experimental data [165] ($\delta z = (z_{\text{sim}} - z_{\text{exp}})/z_{\text{exp}}$) for R227ea: ● present model. Top: vapor pressure, center: saturated liquid density, bottom: enthalpy of vaporization. Error bars indicate simulation uncertainties.

3.6 Conclusion

A strategy is proposed for the rapid development of molecular models for engineering applications. The strategy relies on results from QM *ab initio* calculations to include physically sound molecular properties and to reduce the number of adjustable parameters. Dispersive and repulsive interactions are modeled by LJ sites. Thus, the LJ interaction sites are located according to atom positions obtained by QM energy minimization on the Hartree-Fock level. For the parametrization of the electrostatic interactions, QM calculations are performed using the Møller-Plesset 2 level of theory and the COSMO method. The resulting electron density distribution is reduced to ideal point dipoles and ideal linear point quadrupoles located in the center of mass. The moments and orientations of the dipoles and quadrupoles are passed on to the molecular models without any modification.

A united-atom approach is used for methine, methylene, and methyl groups as well as for ammonia to reduce the total number of interaction sites. The parameters of the LJ sites are initially taken from similar sites of other molecular models and subsequently optimized to reproduce experimental VLE data, i.e. vapor pressure, saturated liquid density, and enthalpy of vaporization. It is aimed to achieve deviations between simulation and experiment of below 5, 1, and 5 % in vapor pressure, saturated liquid density, and enthalpy of vaporization, respectively.

As a case study, the new modeling strategy is successfully applied to a set of ten molecules from different substances classes, i.e. iso-butane, cyclohexane, formaldehyde, dimethyl ether, sulfur dioxide, dimethyl sulfide, thiophene, hydrogen cyanide, acetonitrile, and nitromethane. Simulation results for the different substances agree well with correlations of experimental data taken from reference quality EOS [105] or the DIPPR database [165], with noticeable deviations in the vapor pressure at low temperatures for acetonitrile and nitromethane.

For the two elongated molecules acetonitrile and nitromethane, the reduction of the electrostatic interactions to sites located in the center of mass may be an over-simplification, as the optimization of the molecular models is not fully satisfactory. Also an adjustment of the electrostatic parameters, while keeping the ratio of the polar moments constant (not reported here in detail), does not yield significant improvements in the quality of the molecular models. A further study, e.g. using two or more spatially distributed electrostatic sites, is beyond the scope of this work.

For all other molecules, a significant improvement compared to available molecular models from the literature is achieved. By an optimization to substance specific experimental VLE data, a very good description of the phase equilibrium is obtained. Furthermore, in case of dimethyl ether it is shown that with the proposed modeling strategy it is

possible to reach the same model quality by optimization of just two model parameters compared to five optimized parameters for the model by Ketko and Potoff [91]. This clearly illustrates the reduced modeling effort of the presented modeling strategy.

Finally, the modeling strategy is applied to other molecules. Molecular models for ammonia, ethylene oxide, and heptafluoropropane (R227ea) are developed. The proposed modeling strategy allows a reduction of the adjustable parameters to a reasonable number, which simplifies the optimization of the models to experimental VLE data. Besides a significantly accelerated parametrization, the new molecular models show very good results for VLE properties compared to experimental data. These models are subsequently used to predict other thermophysical properties of the modeled substances as described in the next chapter.

4 Applications in Process Engineering

A major advantage of molecular modeling and simulation is the very good extrapolative power and transferability due to its sound physical basis. For applications in process engineering, often properties at different and sometimes extreme state points are needed. The desired properties are not only VLE data of pure substances, but in most cases, e.g., thermal or caloric properties in the homogeneous fluid region, transport properties, surface tension, or thermophysical properties of mixtures.

In this chapter, some applications of the previously developed molecular models are presented. Besides a prediction of the second virial coefficient for all modeled substances, further results will be presented for selected cases. For ammonia, structural quantities are determined and compared to available experimental data. Also thermal and caloric properties are predicted over a wide range of state points and compared to a reference quality EOS. For ethylene oxide, the general transferability of molecular models is shown by predicting a total of 17 different thermophysical properties, including surface tension and transport properties. Finally, two applications to mixtures are given: The determination of the VLE for the binary mixture ethanol + heptafluoropropane (R227ea) is presented. Concluding the chapter, the simulation of properties of dry and humid air, including the prediction of the dew point, is shown.

4.1 Second Virial Coefficient

The virial expansion gives an EOS, which is often used for low density gases. Starting from the 1930s, it was shown that the virial coefficients can directly be derived from the intermolecular potential [124–126]. The second virial coefficient is related to the molecular model by [57]

$$B = -2\pi \int_0^\infty \left\langle \exp\left(-\frac{u_{ij}(r_{ij}, \boldsymbol{\omega}_i, \boldsymbol{\omega}_j)}{k_\mathrm{B} T}\right) - 1 \right\rangle_{\boldsymbol{\omega}_i, \boldsymbol{\omega}_j} r_{ij}^2 \mathrm{d}r_{ij}, \tag{4.1}$$

where $u_{ij}(r_{ij}, \boldsymbol{\omega}_i, \boldsymbol{\omega}_j)$ is the interaction energy between two molecules i and j, cf. Equation (3.1). k_B denotes Boltzmann's constant and the angle brackets indicate an average over the orientations $\boldsymbol{\omega}_i$ and $\boldsymbol{\omega}_j$ of the two molecules separated by the center of mass distance r_{ij}.

The second virial coefficient is calculated here by evaluating Mayer's f-function, i.e. the expression between the brackets, for about 350 radii up to 20 Å, averaging over 1000^2 random orientations at each radius. The random orientations are generated using a modified MC scheme [29, 133]. A cut-off correction is applied for distances larger than 20 Å for the LJ sites using angle averaging as proposed by Lustig [116]. The electrostatic interactions need no long-range correction as they vanish by angle averaging.

Figures 4.1 to 4.3 show the simulation results compared to correlations of experimental data taken from reference quality EOS [105] or the DIPPR database [165]. For iso-butane, cyclohexane, sulfur dioxide, and dimethyl sulfide, the predictions from simulation agree well with experimental correlations. Only for temperatures near the triple point, deviations of up to 20 % are found. For dimethyl ether and thiophene, the second virial coefficient is systematically overpredicted, despite a good description of the experimental VLE properties.

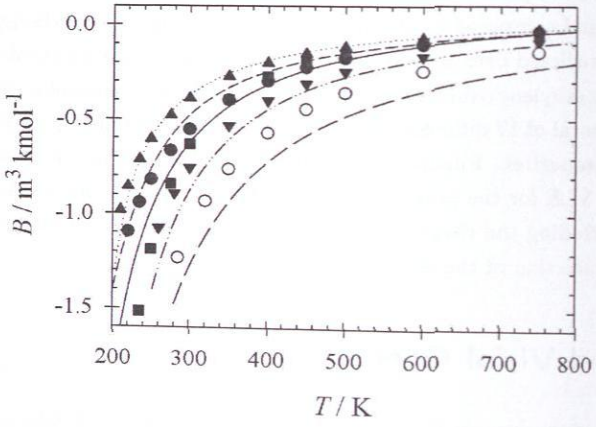

Figure 4.1: Second virial coefficient. Predictions from present molecular models: ● iso-butane, ■ formaldehyde, ▲ dimethyl ether, ▼ dimethyl sulfide, and ○ thiophene. Correlations of experimental data [165]: — isobutane, ··· formaldehyde, - - - dimethyl ether, - ·· - dimethyl sulfide, and – – thiophene.

The second virial coefficient of acetonitrile and nitromethane is underpredicted for temperatures of 500 K and below, cf. Figure 4.3. Like for the VLE properties, a deficiency in the description of the intermolecular potentials is observed here. On the other hand, vapor densities are very low in this temperature range and the second virial coefficient

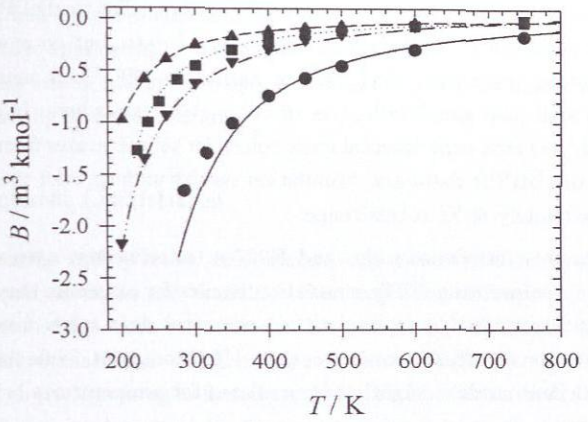

Figure 4.2: Second virial coefficient. Predictions from present molecular models: ● cyclohexane, ■ sulfur dioxide, ▲ ammonia, and ▼ R227ea. Correlations of experimental data [165]: — cyclohexane, ··· sulfur dioxide, - - - ammonia, and - ·· - R227ea.

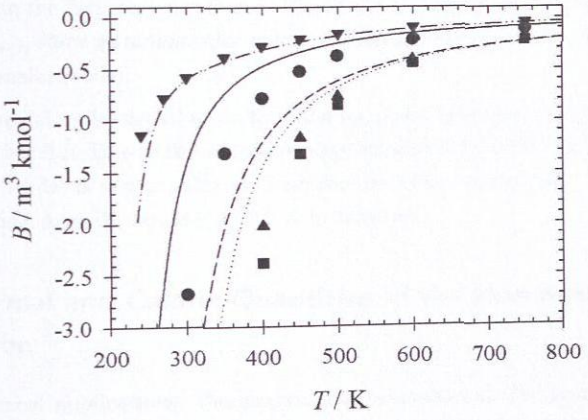

Figure 4.3: Second virial coefficient. Predictions from present molecular models: ● hydrogen cyanide, ■ acetonitrile, ▲ nitromethane, and ▼ ethylene oxide. Correlations of experimental data [165]: — hydrogen cyanide, ··· acetonitrile, - - - nitromethane, and - ·· - ethylene oxide.

only plays a minor role in applications.

For formaldehyde, simulation results substantially underpredict the DIPPR correlation. However, this correlation is not based on experimental data, but on an empirical correlation for ketones, aldehydes, alkyl nitriles, and ether [20]. It is assumed that the prediction from molecular simulation gives more reliable results here. In case of hydrogen cyanide, only five true experimental data points for temperatures from 303 to 383 K are reported in the DIPPR database. Simulation results underpredict the experimental values by approximately 80 % in this range.

Finally, for ammonia, ethylene oxide, and R227ea, an excellent agreement is found over the full temperature range. The simulation results for ammonia show a maximum deviation of -4.3 % at 300 K compared to experimental data taken from the DIPPR correlation. Deviations for R227ea are lower than 4 % throughout, while the second virial coefficient for ethylene oxide is slightly overpredicted for temperatures below 250 K, cf. Figure 4.3.

4.2 Properties of Ammonia

Ammonia is a well-known chemical intermediate, mostly used in fertilizer industries; another important application is its use as a refrigerant. Due to its simple symmetric structure and its strong intermolecular interactions it is also of high academic interest both experimentally and theoretically.

4.2.1 Structural Quantities

Due to its scientific and technical importance, experimental data on the microscopic structure of liquid ammonia are available. Narten [139] and Ricci et al. [164] applied X-ray and neutron diffraction, respectively. The results of Ricci et al. show a smoother gradient and are available for all three types of atom-atom pair correlations, namely nitrogen-nitrogen (N-N), nitrogen-hydrogen (N-H), and hydrogen-hydrogen (H-H), thus they are used for comparison here. In Figure 4.4, these experimental radial distribution functions for liquid ammonia at 273.15 K and 0.483 MPa are compared to present predictive simulation data based on the new ammonia model presented in Section 3.5.1 [30].

It is found that these structural properties are in very good agreement, although no adjustment is done in the parametrization process with respect to structural properties. The atom-atom distance of the first three layers is predicted correctly, while only minor overshootings in the first peak are found. Please note, that the first peak of experiment in g_{N-H} and g_{H-H} show intramolecular pair correlations, which are not considered in the employed molecular model.

In the experimental radial distribution function g_{N-H} the hydrogen bonding of ammonia can be seen at 2–2.5 Å. Due to the simplified approximation by eccentric partial charges, the molecular model is not capable to describe this effect completely. But even with this simple model a small shoulder at 2.5 Å is obtained.

4.2.2 Thermal and Caloric Quantities in the Homogeneous Fluid Region

In many technical applications, thermodynamic properties in the homogeneous fluid region are needed. Thus, the new molecular model for ammonia is tested on its predictive capabilities in this region [30].

Thermal and caloric properties were predicted with the new model in the homogeneous liquid, vapor and supercritical fluid region. In total, 70 state points are studied, covering

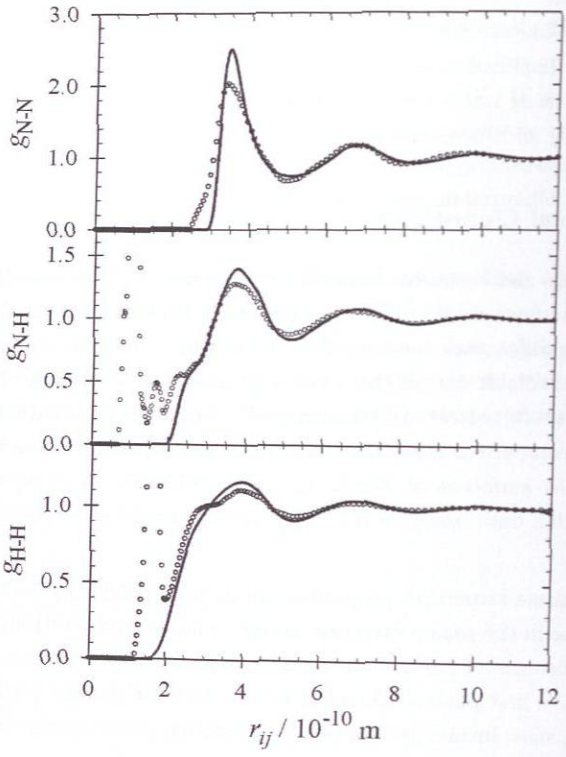

Figure 4.4: Radial distribution functions of ammonia: — simulation data of new model, ○ experimental data [164].

a large range with temperatures up to 700 K and pressures up to 700 MPa. In Figure 4.5, relative deviations between simulation data and reference EOS [202] in terms of density are shown. The deviations are typically below 3 %, with the exception of the extended critical region, where a maximum deviation of 6.8 % was found.

Figure 4.6 presents relative deviations between simulation data and reference EOS [202] for the enthalpy. In this case deviations are very low for low pressures and high temperatures (below 1–2 %). Typical deviations in the other cases are below 5 %.

These results confirm the modeling procedure. By adjustment to VLE data only, quantitatively correct predictions in most of the technically important fluid region can be obtained.

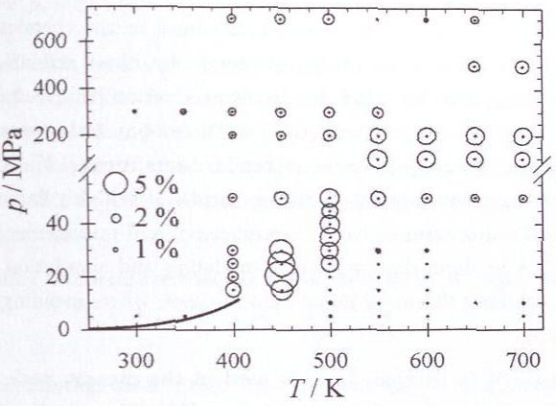

Figure 4.5: Relative deviations for the density of ammonia between simulation data and reference EOS [202] ($\delta\rho = (\rho_{\text{sim}} - \rho_{\text{eos}})/\rho_{\text{eos}}$) in the homogeneous region: o new model, — vapor pressure curve. The size of the bubbles denotes the relative deviation.

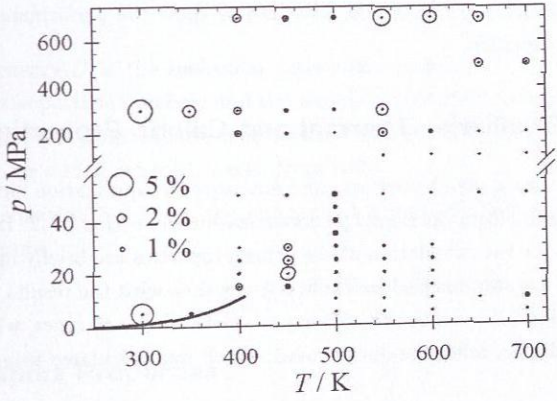

Figure 4.6: Relative deviations for the enthalpy of ammonia between simulation data and reference EOS [202] ($\delta h = (h_{\text{sim}} - h_{\text{eos}})/h_{\text{eos}}$) in the homogeneous region: o new model, — vapor pressure curve. The size of the bubbles denotes the relative deviation.

4.3 Properties of Ethylene Oxide

Ethylene oxide (C_2H_4O) is a widely used intermediate in the chemical industry. In 2006, 18 million metric tons were produced mostly by direct oxidation of ethylene, over 75 % of which were used for ethylene glycols production [26]. Despite its technical and economical importance, experimental data on thermophysical properties of ethylene oxide are rare, apart from basic properties at standard conditions [165]. This lack of data is mainly due to the hazardous nature of ethylene oxide. It is highly flammable, reactive, explosive at elevated temperatures, toxic, carcinogenic, and mutagenic. Therefore, it is an excellent example to show that molecular modeling and simulation can serve as a reliable route for obtaining thermophysical data in cases, where avoiding experiments is highly desirable [206].

The model, as specified in Section 3.5.2, is used in the present work for calculating other properties discussed in the subsequent sections [29]. The calculated properties are selected according to the requirements of the fourth International Fluid Properties Simulation Challenge (IFPSC) [16], which had a focus on the transferability of molecular models to different pure components properties of ethylene oxide. No further parameter adjustments are made on the present ethylene oxide model and thus all results for properties except p_σ, ρ', and Δh_v are fully predictive. All simulations are also performed using the molecular model for ethylene oxide proposed by Wielopolski and Smith [230]. This was done to allow for an evaluation of the applied simulation methods and comparison to other publications [29, 92, 109, 134] and to show the performance of molecular models of different quality.

4.3.1 Phase Equilibria, Thermal and Caloric Properties

The saturated densities, vapor pressure, and enthalpy of vaporization included for comparison here, are taken from the model parametrization in Section 3.5.2. In the following, the specific routes for the calculation of the other properties are briefly introduced. The simulation results are summarized in Table 4.2 together with the results on the basis of the model by Wielopolski and Smith and experimental data. In cases, where no experimental data is available, reference data is used, which was calculated using best-practice methods [152].

Critical Properties, Normal Boiling Temperature Critical temperature and pressure are calculated by fitting the Guggenheim equations [114]

$$\rho' = \rho_\mathrm{c} + C_1 \cdot (T_\mathrm{c} - T)^{1/3} + C_2' \cdot (T_\mathrm{c} - T) + C_3' \cdot (T_\mathrm{c} - T)^{3/2} \,, \tag{4.2}$$

and

$$\rho'' = \rho_c - C_1 \cdot (T_c - T)^{1/3} + C_2'' \cdot (T_c - T) + C_3'' \cdot (T_c - T)^{3/2} \,, \tag{4.3}$$

to the VLE simulation results at eight temperatures between 235 and 445 K for the present model, cf. Appendix B. For the model by Wielopolski and Smith [230], eight temperatures between 235 and 430 K are considered, cf. Appendix B, as this model has a lower critical temperature. Note that critical temperature T_c and critical density ρ_c are parameters of this fit and are thus extracted from the temperature dependence of the saturated densities.

The normal boiling temperature was calculated indirectly. A vapor pressure equation

$$\ln\, p_\sigma = C_4 + \frac{C_5}{T} + \frac{C_6}{T^4} \,, \tag{4.4}$$

is fitted to the simulation data. From this equation, the normal boiling temperature is calculated at $p_\sigma = 101.325$ kPa.

Heat capacity, isothermal compressibility The second derivatives of the Gibbs energy, namely isobaric heat capacity c_p and isothermal compressibility β_T, can be calculated from fluctuations in the NpT ensemble [3]. Fluctuations in the instantaneous residual enthalpy $h^{\text{res}} = U/N + pV/N - k_B T$ are related directly to the residual isobaric heat capacity

$$c_p^{\text{res}} = \frac{1}{k_B T^2} \left(\left\langle h^{\text{res}\,2} \right\rangle - \left\langle h^{\text{res}} \right\rangle^2 \right) \,. \tag{4.5}$$

The potential energy U is the molecular interaction energy, cf. Equation (3.1). V is the volume, N the particle number, and the angular brackets denote the NpT ensemble average. To obtain the total isobaric heat capacity c_p, the ideal part $c_p^{\text{id}} = 59.6$ J/(mol K) at 375 K has to be added, which is taken from [165].

An analogous equation holds for the isothermal compressibility, which is related to volume fluctuations

$$\beta_T = \frac{1}{\langle V \rangle k_B T} \left(\left\langle V^2 \right\rangle - \left\langle V \right\rangle^2 \right) \,. \tag{4.6}$$

4.3.2 Transport Properties

Transport properties are calculated by equilibrium MD simulation and the Green-Kubo formalism [58, 100]. In this formalism, transport coefficients are obtained by integrating time-autocorrelation functions of the corresponding microscopic fluxes.

The shear viscosity η is calculated by integration of the time-autocorrelation function of the off-diagonal elements of the stress tensor J_p^{xy} [60, 185]

$$\eta = \frac{1}{Vk_BT}\int_0^\infty \left\langle J_p^{xy}(t)\cdot J_p^{xy}(0)\right\rangle \mathrm{d}t\ . \tag{4.7}$$

The statistics of the ensemble average in Equation (4.7) are improved using all three independent off-diagonal elements of the stress tensor J_p^{xy}, J_p^{xz}, and J_p^{yz}. For a pure fluid, the component J_p^{xy} of the microscopic stress tensor $\mathbf{J}_p$ is given by [40]

$$J_p^{xy} = \sum_{i=1}^{N} m v_i^x v_i^y - \sum_{i=1}^{N-1}\sum_{j=i+1}^{N}\sum_{a=1}^{S_i}\sum_{b=1}^{S_j} r_{ij}^x \frac{\partial u_{ij}}{\partial r_{ijab}^y}\ . \tag{4.8}$$

Here the upper indices x and y denote the vector component, e.g., for velocity v_i^x or center of mass distance r_{ij}^x. S_i and S_j are the number of interaction sites on particle i and j, respectively, cf. Equation 3.1.

The thermal conductivity λ is calculated by integration of the time-autocorrelation function of the elements of the microscopic heat flow J_q^x and is given by [60, 185]

$$\lambda = \frac{1}{Vk_BT^2}\int_0^\infty \left\langle J_q^x(t)\cdot J_q^x(0)\right\rangle \mathrm{d}t\ . \tag{4.9}$$

The expression for the heat flow $\mathbf{J}_q$ in pure fluids is given by [40]

$$\mathbf{J}_q = \frac{1}{2}\sum_{i=1}^{N}\left(\left(m\mathbf{v}_i^2 + \mathbf{w}_i\mathbf{I}_i\mathbf{w}_i + \sum_{j\neq i}^{N} u_{ij}\right)\cdot \mathbf{v}_i\right) - \sum_{i=1}^{N-1}\sum_{j=i+1}^{N}\sum_{a=1}^{A}\sum_{b=1}^{B}\mathbf{r}_{ij}\cdot\left(\mathbf{v}_i\frac{\partial u_{ij}}{\partial \mathbf{r}_{ijab}} + \mathbf{w}_i\boldsymbol{\Gamma}_{ij}\right)\ , \tag{4.10}$$

where $\mathbf{w}_i$ is the angular velocity vector of molecule i, $\mathbf{I}_i$ its matrix of angular momentum of inertia. The torque $\boldsymbol{\Gamma}_{ij}$ refers to a reference frame with origin in the molecular center of mass. As for shear viscosity, all three independent heat flow directions J_q^x, J_q^y, and J_q^z are used to improve the statistics of Equation (4.9).

While the shear viscosity and diffusion coefficients are not appreciably affected by the internal degrees of freedom, there is a considerable contribution to the thermal conductivity in the gaseous state [68]. The heat flux on the molecular level splits up in one part due to intermolecular interactions and one due to the energy carried by the internal degrees of freedom of single molecules. As intermolecular interactions become weaker with decreasing density, the latter part plays a more significant role. From the Chapman-Enskog kinetic theory of gases and early work of Eucken [39], the so-called Eucken correction is derived [68]

$$\lambda = \lambda_0\left(\frac{4}{15}\frac{c_v}{k_B} + \frac{3}{5}\right)\ , \tag{4.11}$$

where λ_0 is the thermal conductivity from kinetic gas theory for molecules without

internal degrees of freedom and c_v denotes the isochoric heat capacity.

Equation (4.11) is used here to correct the thermal conductivity in the vapor, where the simulation results from the rigid molecular model are λ_0. The isochoric heat capacity is calculated from fluctuations in NVT ensemble simulations, analogously to those described in Section 4.3.1. At the simulated state points, correction factors of 2.50 (present model) and 2.36 (model of Wielopolski and Smith [230]) are obtained at 375 K. For the thermal conductivity in the saturated liquid no correction is applied, as the thermal conductivity is dominated by the intermolecular interactions at high densities. Assuming that the energy transport due to the internal degrees of freedom is temperature dependent only, the correction in the liquid should be in the range of $\lambda - \lambda_0$ from the vapor phase. As this correction is within the statistical uncertainty of the liquid simulation, it is neglected here.

4.3.3 Surface Tension

To calculate the surface tension, the VLE is directly simulated in an inhomogeneous system that exhibits two planar interfaces. MD runs are performed in an elongated cuboid shaped volume with periodic boundary conditions in all directions. The volume has a length of l in x and y direction and a length of $5l$ in z direction. It containes a vapor and a liquid phase forming two interfaces in the x, y-plane of the simulation volume. The liquid phase is chosen to have a thickness of approximately l so that the vapor phase has a thickness of $4l$. From this arrangement follows that two planar vapor-liquid interfaces with an area of $A = l^2$ are simulated.

Table 4.1 presents the saturated densities from both molecular models for different cut-off radii according to Appendix A.2, together with the respective data from homogeneous VLE simulations, cf. Table 4.2. With increasing cut-off radius, the bubble density monotonously increases, whereas the dew density and interfacial thickness monotonously decrease practically throughout. For the largest employed cut-off radius $r_c = 25$ Å, the saturated densities were sampled satisfactorily with deviations lower than -0.8 % for the liquid and +3 % for the vapor. The interfacial thickness is obtained to be approximately 12 Å as predicted by the present model, whereas the model of Wielopolski and Smith [230] yields a result that is roughly 10 % higher.

During these runs, the surface tension γ is calculated via the virial route [166]

$$\gamma = \frac{1}{2A} \left\langle \sum_{i=1}^{N-1} \sum_{j=i+1}^{N} \sum_{a=1}^{A} \sum_{b=1}^{B} \frac{\mathbf{r}_{ij}\mathbf{r}_{ijab} - 3z_{ij}z_{ijab}}{\mathbf{r}_{ijab}} \cdot \frac{\partial u_{ij}}{\partial \mathbf{r}_{ij}} \right\rangle_{r<r_c} . \tag{4.12}$$

Note that expression (4.12) holds for the explicitly evaluated intermolecular interactions, including LJ and electrostatic.

Table 4.1: Saturated densities, interfacial thickness and surface tension of ethylene oxide at 375 K from planar interface VLE simulations for different cut-off radii. Numbers in bold characters indicate saturated densities from homogeneous VLE simulations, cf. Table 4.2.

r_c Å	ρ_l mol/l	ρ_v mol/l	D Å	γ N/m
present model				
12	15.62	0.959	14.793	0.0058
14	16.16	0.775	13.236	0.0075
16	16.41	0.677	12.650	0.0080
18	16.56	0.615	12.446	0.0090
20	16.65	0.609	12.453	0.0093
25	16.75	0.566	11.983	0.0096
—	**16.86**	**0.554**	—	—
model of Wielopolski and Smith [230]				
12	14.55	1.298	16.736	0.0034
14	15.16	1.027	15.015	0.0053
16	15.42	0.886	14.124	0.0058
18	15.59	0.855	13.746	0.0065
20	15.70	0.800	13.550	0.0065
25	15.80	0.756	13.333	0.0069
—	**15.93**	**0.734**	—	—

Table 4.1 compiles the surface tension results for the two simulation series. It can be seen that γ increases with r_c which is in agreement with other work [113, 127]. On the basis of these results, the surface tension is extrapolated to $r_c \to \infty$ by an inverse cubic function of the cut-off radius. This type of extrapolation is used as it scales the densities well with bulk densities obtained by VLE simulations for both models.

4.3.4 Comparison to Experimental Data

Results on the VLE properties of ethylene oxide from the present model as well as from the model of Wielopolski and Smith [230] were already discussed in Section 3.5.2. With the new ethylene oxide model, a much better description of the VLE behaviour is reached. In this section, the results obtained for both molecular models, given in Table 4.2, are discussed. The reference data in Table 4.2 are experimental data, where available, or calculated by phenomenological correlations [152].

Saturated densities, vapor pressure, and enthalpy of vaporization of ethylene oxide at 375 K are all described by the present model with deviations below 1 % and therefore within the experimental error given in [165]. The model of Wielopolski and Smith

Table 4.2: Results for different thermophysical properties of ethylene oxide. The number in parentheses indicates the statistical uncertainty in the last digit. The reference data given without explicit source, are calculated with correlations taken from [165].

Property	Unit	Present Model	Model of Wielopolski and Smith [230]	Experimental / Reference Data
Category 1				
saturated liquid density at 375 K	mol/l	16.86(1)	15.91(1)	16.89
saturated vapor density at 375 K	mol/l	0.554(2)	0.752(3)	0.559
second virial coefficient at 375 K	l/mol	-0.323(1)	-0.250(1)	-0.361
vapor pressure at 375 K	MPa	1.43(2)	1.92(2)	1.437
enthalpy of vaporization at 375 K	kJ/mol	19.83(2)	17.61(2)	19.95
normal boiling temperature at 101.325 kPa	K	282.6	268.8	283.5
critical density	mol/l	7.221	7.127	7.128 [101]
critical temperature	K	468.6	462.5	469.2 [101]
Category 2				
saturated liquid isobaric heat capacity at 375 K	J/(mol K)	114(3)	111(3)	101.3 [152]
saturated vapor isobaric heat capacity at 375 K	J/(mol K)	86.4(9)	83.2(7)	73.6 [152]
saturated liquid isothermal compressibility at 375 K	1/GPa	3.6(2)	4.2(3)	2.79 [152]
saturated vapor isothermal compressibility at 375 K	1/GPa	865(18)	667(13)	819 [152]
surface tension at 375 K	N/m	0.0100(7)	0.0073(5)	0.012
Category 3				
saturated liquid shear viscosity at 375 K	10^{-4} Pa s	1.4(2)	1.1(2)	1.51 [152]
saturated vapor shear viscosity at 375 K	10^{-4} Pa s	0.12(2)	0.08(2)	0.120
saturated liquid thermal conductivity at 375 K	W/(m K)	0.13(4)	0.12(3)	0.12 [152]
saturated vapor thermal conductivity at 375 K	W/(m K)	0.019(4)	0.024(5)	0.020

underpredicts saturated liquid density and enthalpy of vaporization by 5.8 % and 12 %, respectively, while vapor pressure and saturated vapor density are overpredicted by more than 30 %.

Critical properties, obtained from Equations (4.2) and (4.3), are in excellent agreement with experimental data, being within 1.3 %, for both models. The normal boiling temperature, calculated by Equation (4.4), deviates by less than 0.5 % from experimental data for the present model, while the model of Wielopolski and Smith shows larger deviations of about -5.3 %.

The second virial coefficient is calculated by direct evaluation of the intermolecular potential. Both models underpredict the experimental value at 375 K: the present model has a deviation of 3.4 %, while the model of Wielopolski and Smith has 25 %, cf. Table 4.2.

Experimental data on isobaric heat capacity and isothermal compressibility for the saturated fluid states at 375 K are not available in the literature. Instead, reference values published by Olson and Wilson [152] are used for comparison here. Isobaric heat capacities are overpredicted by both models. In the saturated liquid, the present model deviates by 13 % and the model of Wielopolski and Smith by 9.6 %. In the saturated vapor, they deviate by 18 % and 13 %, respectively. Reference values for isothermal compressibility were obtained from the Brelvi-O'Connell correlation [11, 152] for the saturated liquid and from the virial equation for the saturated vapor. Simulations for the present model yield a 29 % higher result for the liquid state and a 5.6 % higher result for the vapor state. The results from the model of Wielopolski and Smith deviate by 51 % and -19 % for the liquid and vapor, respectively.

Experimental surface tension data are available between 200 and 296 K and may be extrapolated to higher temperatures using a correlation taken from [165]. The results from the present model give deviations of -17 %, the model of Wielopolski and Smith yields -39 %.

Experimental transport properties for ethylene oxide are scarce. In fact, for shear viscosity and thermal conductivity at 375 K they are only available in the saturated vapor state. Here, the results from the present model agree with the experimental values within their statistical uncertainty, while the model of Wielopolski and Smith underpredicts the shear viscosity by approximately 33 % and overpredicts the thermal conductivity by 20 %. Olson and Wilson [152] give reference values for shear viscosity in the saturated liquid state from an extrapolation of experimental data from 223 to 282 K and for thermal conductivity from the Missenard method [130]. Simulation results obtained with the present model agree with the reference values within their statistical uncertainties and the uncertainties of the reference values proposed by [152]. Results from the model

of Wielopolski and Smith underpredict the liquid shear viscosity by 27 %, but agree for the liquid thermal conductivity with the reference value.

The example ethylene oxide shows that molecular modeling and simulation is capable to consistently reproduce and predict various thermophysical properties with a single model. The sound physical basis of the method provides confidence in the results. E.g., while the deviation from the reference value for the isothermal compressibility in the saturated vapor state is within the assumed uncertainty of 9.2 %, the one in the saturated liquid state is significantly above the assumed uncertainty of 23.1 %. This is astonishing as the densities predicted by the present model along the bubble line are in good agreement with experimental ethylene oxide data. An additional check, evaluating simulation runs at different pressures for 375 K, yields a value within the statistical uncertainty of the previous simulation result. On the other side, the Brelvi-O'Connell correlation is known to give systematic deviations to too low compressibilities for polar substances similar to ethylene oxide, like sulfur dioxide or acetone [11]. Therefore, it may be stated that molecular modeling and simulation yields more reliable results here than the standard phenomenological method does.

With the presented results, we participated in the fourth Industrial Fluid Properties Simulation Challenge. The Simulation Challenge is an international contest organized by IFPSC, an international collaboration between chemical industry, academia, and national labs (coordinated by the National Institute of Standards and Technology) [1], to compare different simulative methods and to make their capabilities public. On the AIChE Annual Meeting 2007 in Salt Lake City, UT, U.S.A., this contribution was announced Champion of the Simulation Challenge 2007 [16].

4.4 Properties of the Binary Mixture R227ea + Ethanol

Most technical processes in chemical engineering are dealing with fluid mixtures. Thus, thermophysical properties of those mixtures are needed for process development and optimization. Molecular modeling and simulation provides a straightforward route to describe mixtures on the basis of pure substance molecular models. In this section, one example is given that shows the basic theory and predictive power of the molecular approach.

For this task, the vapor pressure prediction for the binary mixture 1,1,1,2,3,3,3-heptafluoropropane (R227ea) + ethanol at 343.13 K is selected [27]. The fluorinated propane R227ea has one remaining hydrogen atom, which acts electrostatically like a positive partial charge due to the strong electronegativity of the fluorine atoms. While

R227ea does not exhibit hydrogen bonding with itself, it is a good donor in vicinity of a hydrogen bond acceptor like ethanol. Thus, the binary mixture R227ea + ethanol has a type of interaction, which is not present in the two pure substances alone. This problem was also selected by the IFPSC for their third Simulation Challenge in 2006 [15].

Reliable VLE data is easily accessible for both pure components [165]. However, for the binary mixture, only experimental bubble line data at the two isotherms 283.15 and 353.15 K are publicly available. These data were used for comparison in the following.

In the present work, both molecular modeling and simulation as well as the phenomenological Peng-Robinson equation of state (PR-EOS) [179] are employed to tackle this problem. The molecular model for R227ea as presented in Section 3.5.3 is used here, while for ethanol, the molecular model of Schnabel et al. [174] is taken.

The ethanol model of Schnabel et al. consists of three LJ sites plus three point charges. Compared to experimental data, vapor pressure, saturated liquid density and heat of vaporization, the ethanol model yield mean unsigned errors of 3.7, 0.3, and 0.9 %, respectively, in the temperature range 270 to 490 K, which is about 55 to 95 % of the critical temperature. Critical values of temperature, density and pressure also agree well with experimental data (numbers in parentheses): $T_c = 514.12$ (516.25) K, $\rho_c = 5.94$ (5.99) mol/l and $p_c = 5.89$ (6.38) MPa. Further details are given in [174].

4.4.1 Mixture Model

On the basis of existing pairwise additive pure fluid models, molecular modeling of mixtures reduces to modeling the interactions between unlike molecules. The unlike interactions can be divided in two groups here. The electrostatic interactions between point charges, dipoles, and quadrupoles represent the first group. They can be treated in a physically straightforward way, simply using the laws of electrostatics [57], which is done here.

The second group of interaction are repulsion and dispersive attraction. Since these interactions were modelled on the basis of LJ potentials, the knowledge of the unlike LJ parameters σ_{RE} and ε_{RE} is required. Unfortunately, there is no reliable framework for their determination [175]. However, the broadly used Lorentz-Berthelot combining rule [6, 112] usually provides a good starting point

$$\sigma_{RE} = (\sigma_R + \sigma_E)/2 \,, \tag{4.13}$$

and

$$\varepsilon_{RE} = \sqrt{\varepsilon_R \varepsilon_E} \,. \tag{4.14}$$

Here a simplified notation is used, summarizing the different LJ parameters of R227ea under σ_R and ε_R as well as the different LJ parameters of ethanol under σ_E and ε_E. Applying σ_{RE} and ε_{RE} as given by Equations (4.13) and (4.14) allows the prediction of mixture properties from pure fluid data alone. In many cases, these predictions are already in good agreement with experimental data [174, 175, 186, 189, 220]. But as shown there, a further improvement can generally be achieved by adjusting the unlike energy parameter to the experimental vapor pressure of the mixture.

This adjustment is skipped here, as the Lorentz-Berthelot based mixture model matches with the experimental data for 283.15 K within the (large) error bars. These high statistical uncertainties are mainly due to the calculation of the chemical potentials in the "cold", thus dense, liquid phase by Widom's insertion method, cf. Section 2.3.1. Subsequently, the molecular model is used to predict the vapor pressure of the binary mixture at 353.15 K.

4.4.2 Results and Discussion

Figure 4.7 compares the simulation results at 283.17 K with the experimental bubble line data provided by Gordon et al. [56]. Considering the somewhat too low vapor pressure of the R227ea pure substance model (8.2 %) at this temperature, it can be seen that the slope of the mixture bubble line is reasonably followed. Furthermore, at the equimolar liquid composition, simulation and experiment agree within the statistical uncertainty of 10.6 % in pressure. Therefore, it was concluded that no adjustment of the unlike LJ parameters is needed.

The PR-EOS together with the Van der Waals one-fluid mixing rule [179] is also applied to the present mixture, cf. Figure 4.7. It turns out that it is not possible to describe the experimental data with that phenomenological model. Fitting the binary interaction parameter at low R227ea molar fractions ($k_{ij} = -0.08$) yields a good description up to about $x_{R227ea} = 0.1$ mol/mol. At higher molar fractions the PR-EOS with this k_{ij} gives substantially too low vapor pressures. Increasing k_{ij} to -0.03 yields higher vapor pressures, but also a qualitatively wrong shape of the bubble line.

The molecular model is used to predict the vapor pressure at 343.15 K throughout the full composition range. This prediction was part of the third International Fluid Properties Simulation Challenge in 2006 [15]. Figure 4.8 presents the VLE data and compares it to experimental bubble line data [56], which were published after closure of the Simulation Challenge. It can be seen that the simulation results match with the experimental data within their statistical uncertainties with exception of the result at $x_{R227ea} = 0.274$ mol/mol, which also has a very large statistical uncertainty. The latter again reflects the problems in determining the chemical potentials in the liquid phase

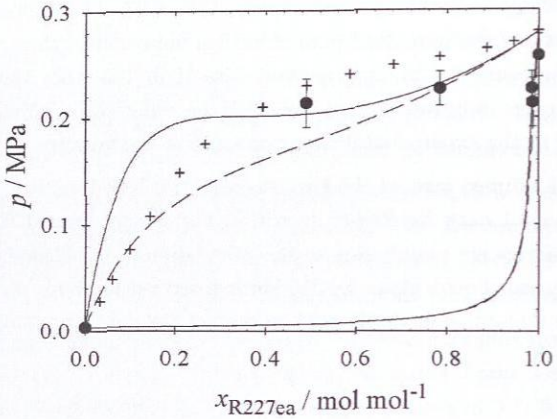

Figure 4.7: VLE of R227ea + ethanol at 283.17 K: ● present simulation data, + experimental bubble line data [56], — and – – Peng-Robinson EOS with $k_{ij} = -0.03$ and -0.08, respectively.

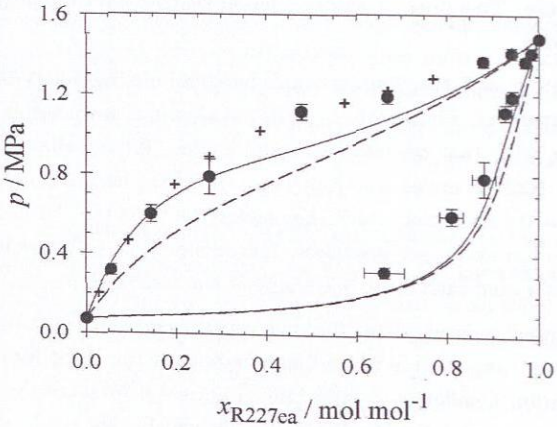

Figure 4.8: VLE of R227ea + ethanol at 343.13 K: ● present simulation data, + experimental bubble line data [56], — and – – Peng-Robinson EOS with $k_{ij} = -0.03$ and -0.08, respectively.

by Widom's method.

With the presented results at 343.15 K, this contribution was the second entry at the Simulation Challenge 2006 [15, 27].

The PR-EOS adjusted at low R227ea mole fractions at 283.17 K ($k_{ij} = -0.08$) yields too low vapor pressures at 353.15 K throughout, cf. Figure 4.8. On the other hand, adjusting the PR-EOS to simulation data at low R227ea mole fractions at 343.13 K ($k_{ij} = -0.03$) yields a qualitatively wrong shape of the bubble line, which was also seen at the low temperature, cf. Figure 4.7.

The prediction of the VLE of the binary mixture R227ea + ethanol is done here without any adjustment to mixture data. Thus, it may be stated that molecular modeling and simulation represents even complex systems inherently correct due to its sound physical basis. In this example, the molecular approach is advantageous compared to the PR-EOS, which fails even in the descriptive mode.

4.5 Properties of Humid Air

Knowledge on thermodynamic data of compressed humid air and other compressed humid gases are crucial for the design and optimization of many technical processes, e.g., humid gas turbine, compressed air energy storage, or carbon dioxide separation and sequestration. However, only little experimental data is available [64]. Of special interest is the dew point of compressed humid air, where significant deviations from ideal gas properties are reported in the literature [75, 76, 95, 159, 222, 231]. In the present section, molecular modeling and simulation is applied for predictions of thermodynamic properties of humid air [28].

For technical applications, the dew point of humid air is generally defined by the "partial pressure" of water $p_W = x_W \cdot p$ in the compressed gas at saturation, where x_W is the water mole fraction and p the total pressure. Note that this is only a formal definition of the property p_W. The partial pressure in a strictly physical sense is only defined for ideal gases.

The saturated water mole fraction at the dew point of humid air increases at constant temperature progressively with total pressure p due to an increasing influence of the intermolecular interactions in the gas phase and due to the compression of the liquid phase. This effect can be described by the vapor pressure enhancement factor f_W

$$f_W(T,p) = \frac{p_W}{p_W^0} , \tag{4.15}$$

which is the ratio of the partial pressure of water p_W to the vapor pressure of pure water p_W^0 at the same temperature T. The vapor pressure enhancement factor f_W is usually measured via the mole fraction x_W of water in the saturated gas phase either by gas-chromatography or gravimetrically after expansion. Data for f_W is very sensitive to experimental errors and uncertainties in the determination of the mole fraction. Thus, f_W data from gas-chromatography is often inconsistent. The gravimetric method is more suitable but very elaborate [225].

The dew point of compressed humid gases can also be described by the vapor concentration enhancement factor g_W [95, 231]

$$g_W(T,p) = \frac{c_W}{c_W^0} , \tag{4.16}$$

which is the ratio of the water concentration $c_W = x_W \cdot \rho$ in the saturated humid gas to the saturated vapor density of pure water c_W^0 at the same temperature T. The water concentration c_W can directly be measured by spectrometry. This was recently done by Koglbauer and Wendland [95, 96], who developed a new method to measure g_W by FTIR spectrometry. This method yields consistent data over a wide range of temperature and pressure. Data on g_W of compressed humid air [95], nitrogen, argon, and carbon dioxide [96] agree qualitatively well with literature data on f_W as far as available. However, a quantitative comparison relies on gas densities that are needed for the conversion between both enhancement factors. They are related by [95, 231]

$$g_W = f_W \frac{Z_W^0}{Z} , \tag{4.17}$$

where Z and Z_W^0 are the compressibility factors of the saturated humid gas and pure water vapor, respectively.

A comparison of the experimental g_W data for humid air by Koglbauer and Wendland with g_W values by Wiley and Fisher [231], calculated by a virial EOS model that was fitted to experimental f_W data, shows some deviations at elevated pressures, which will be discussed subsequently. Also recent humid air density data deviates from virial EOS models [64, 94]. The suitability of the virial EOS for the dew point of highly compressed humid gases has been contested elsewhere [225] and the application of empirical multiparameter EOS was suggested. But these need a large and reliable data base for their development, which is not available yet.

It can be concluded that it is important to gain insight into the behavior of compressed humid air and to determine additional thermodynamic data from an independent source such as the molecular simulation for comparison with experimental results and for the development of new models. Molecular simulation may simultaneously yield consistent

data on f_W, g_W, saturated gas density, etc.

The present work on humid air is organized in two parts. Firstly, a molecular model for dry air, proposed in an earlier work [216, 220], is assessed regarding thermal and caloric properties, i.e. density and internal energy, for temperatures up to 1000 °C and pressures up to 200 MPa. The simulation results are compared to two reference EOS recommended by the National Institute of Standards and Technology.

In the second part, the dry air model is combined with two different water models for the simulation of humid air. In addition to predictions of the density, dew point data of humid air are presented, which are calculated by simulation using a new pseudo-ensemble. The simulation data is compared to experimental data and a conclusion is drawn.

4.5.1 Dry Air Simulations

For the leading three dry air components nitrogen, oxygen, and argon, molecular models from previous work [219] are used. These models are based on the two center LJ plus symmetric point quadrupole (2CLJQ) class and have successfully been applied for the prediction of numerous binary and ternary VLE [71, 188, 213, 214, 220], the Joule-Thomson inversion curve of pure substances, natural gas mixtures, and air [216, 218] as well as transport properties [43, 44].

The parameters of the unlike LJ interactions are determined by the modified Lorentz-Berthelot rule as described in Section 3.1. The three binary interaction parameters for the dry air model are taken from prior work [219] on the VLE of the binary subsystems. No further optimizations are made in the present work, thus all mixture data presented here are strictly predictive.

To predict the VLE in the ternary mixture nitrogen + oxygen + argon, the Grand Equilibrium method is applied, cf. Section 2.4. Technical details are given in the Appendix A. Figure 4.9 shows the VLE simulation results in comparison to experimental data [137] and the results of the recent GERG-2004 EOS [103]. The simulation results are in excellent agreement with experimental data. The GERG-2004 EOS deviates by about 3 to 4 mole-% from the experimental and simulation data sets on both the bubble and dew line towards the nitrogen-rich region, which is somewhat more than the estimated uncertainty stated in [103].

The term *dry air* is used in the following for that ternary mixture at the composition $x_{N_2} = 0.781438$ mol/mol, $x_{O_2} = 0.209540$ mol/mol, and $x_{Ar} = 0.009022$ mol/mol [94, 95]. Figures 4.10 to 4.13 show simulation results for the density ρ and the residual internal energy $u^{res} = u(T,p) - u(T,p \to 0)$ for dry air along isotherms and isobars,

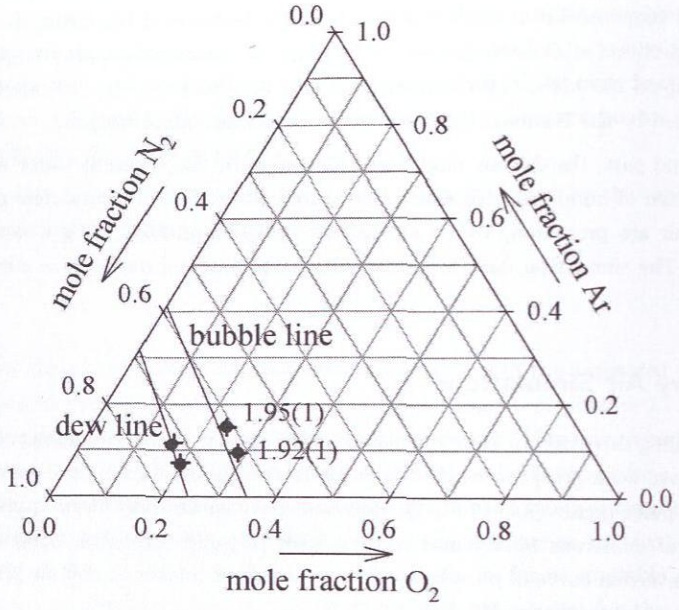

Figure 4.9: VLE of the ternary mixture nitrogen + oxygen + argon at 120 K and 1.995 MPa. Present simulation data (●) are compared to experimental data (+) [137] and the GERG-2004 EOS (—) [103]. The numbers with the simulation results give the predicted vapor pressure in MPa with the simulation uncertainty in the last digit in parentheses.

respectively. Covering state points over a wide range, reaching up to 1000 °C and 200 MPa, the simulation results are compared to two EOS of reference quality, i.e. the GERG-2004 EOS [103] and the EOS by Lemmon et al. [106].

An excellent agreement between simulation and both EOS is found. Deviations to the GERG-2004 EOS are below 1.2 % for the density and below 6 % for the residual internal energy in all cases. The largest deviations for the residual internal energy are found at 1000 °C, where the two considered EOS deviate by up to 10 % from each other. Present simulation results lie in between, however, they rather follow the trend of the EOS by Lemmon et al. [106], which was specifically developed for dry air.

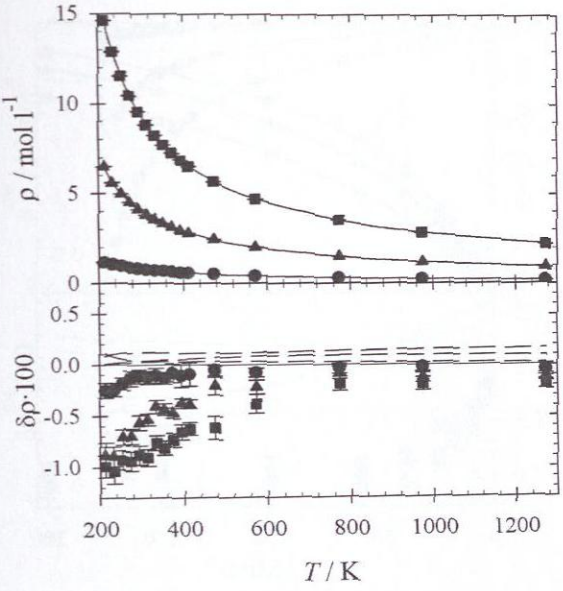

Figure 4.10: Density of dry air (top) and relative deviation to the GERG-2004 EOS [103] (bottom) along isobars. Present simulation data: ● 2 MPa, ▲ 10 MPa, and ■ 20 MPa. — GERG-2004 EOS, – – EOS by Lemmon et al. [106].

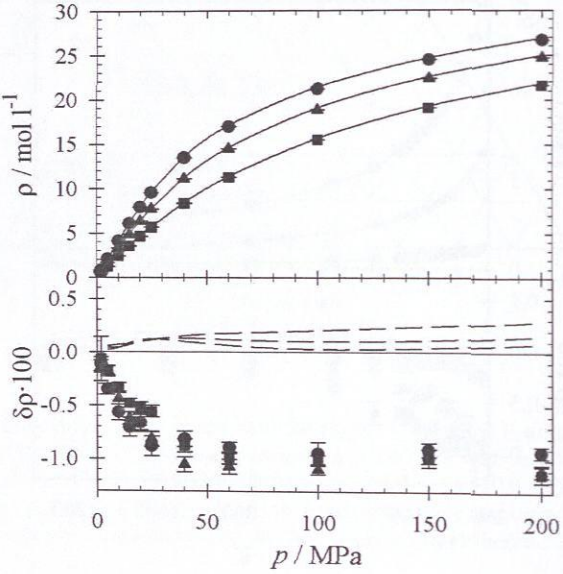

Figure 4.11: Density of dry air (top) and relative deviation to the GERG-2004 EOS [103] (bottom) along isotherms. Present simulation data: ● 293 K, ▲ 353 K, and ■ 473 K. — GERG-2004 EOS, – – EOS by Lemmon et al. [106].

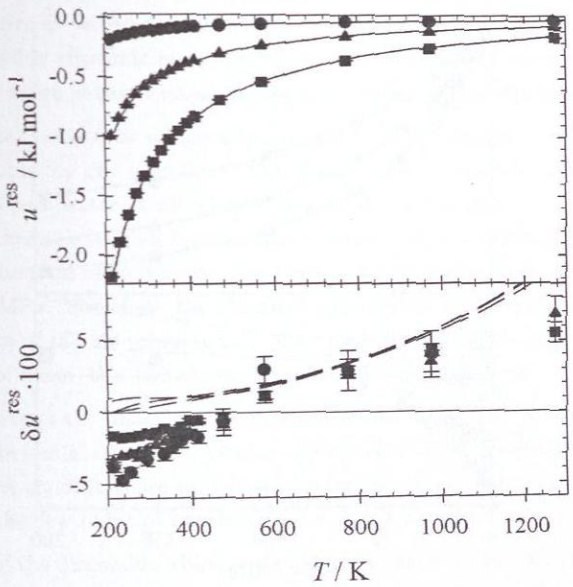

Figure 4.12: Residual internal energy of dry air (top) and relative deviation to the GERG-2004 EOS [103] (bottom) along isobars. Present simulation data: ● 2 MPa, ▲ 10 MPa, and ■ 20 MPa. — GERG-2004 EOS, – – EOS by Lemmon et al. [106].

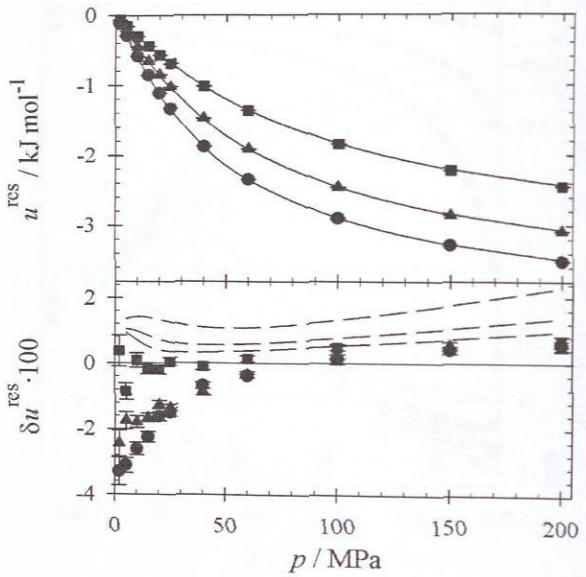

Figure 4.13: Residual internal energy of dry air (top) and relative deviation to the GERG-2004 EOS [103] (bottom) along isotherms. Present simulation data: ● 293 K, ▲ 353 K, and ■ 473 K. — GERG-2004 EOS, – – equation of state by Lemmon et al. [106].

4.5.2 Humid Air Simulations

4.5.2.1 Mollier Ensemble

A pseudo-ensemble is proposed for the direct determination of the dew point of compressed humid air by molecular simulation. This approach, named Mollier ensemble here, combines features from the well-known isobaric-isothermal (NpT) and grand-canonical (μVT) ensembles [50]. During simulation, the saturated gas phase is sampled at the specified temperature T and constant pressure p [50]. Also specifying the number of dry air molecules, i.e. keeping the number of nitrogen, oxygen, and argon constant, the water content is varied to achieve chemical equilibrium with the aqueous liquid phase. The Mollier ensemble is similar to the "osmotic" pseudo-ensemble proposed by Escobedo [37], which is based on earlier work of Mehta and Kofke [129].

The fluid phase coexistence of the mixture water + air around ambient conditions is a typical example for gas solubility. The Henry's law constants of the three gaseous components in pure water at 80 °C are: $H_{N2} \approx 10.5$ GPa, $H_{O2} \approx 5.5$ GPa, and $H_{Ar} \approx 5$ GPa [221]. Thus, the aqueous liquid phase contains only a small quantity of the gaseous components, the total mole fraction $x_{N2} + x_{O2} + x_{Ar}$ is in the order of 10^{-3} mol/mol at 80 °C and 25 MPa. Therefore, the chemical potential of liquid water is hardly affected by the presence of the air components. Note that for high temperatures, closer to the critical point of water, this assumption is not valid.

For saturated states the phase equilibrium conditions apply, i.e. temperature, pressure, and chemical potential of all components are equal in the coexisting phases, cf. Equation 2.12. These conditions are exploited to construct the Mollier ensemble which allows to determine the dew point of humid air for a specified pair of T and p.

On the basis of the discussion above, it is assumed that the chemical potential of water μ_W in the liquid is not significantly influenced by the presence of a small fraction of dry air molecules. Then, the chemical potential of liquid water can be calculated by a pure substance NpT simulation at T and p in a first step. For liquid water around ambient conditions, sophisticated simulation methods, cf. Section 2.3.2, are needed to obtain entropic properties with reasonable statistical uncertainties. In the second step, a humid air dew point simulation with a specified number of air molecules $N_{N2}+N_{O2}+N_{Ar}$ is performed, where T, p, and $\mu_W(T,p)$ are also specified. Of course, in that pseudo-ensemble, the number of water molecules N_W and the volume of the vapor phase V must be allowed to fluctuate. Here, a MC scheme is employed for that.

The chemical potential of water μ_W, taken from the pure liquid water run, is specified through insertion and deletion of water molecules during simulation of the vapor phase like in the standard μVT ensemble. The probability of insertions and deletions is then

determined by comparison between the resulting potential energy change and the desired residual chemical potential $\tilde{\mu}_{\mathrm{W}}$. Note that $\tilde{\mu}_{\mathrm{W}}$ is defined by subtracting the solely temperature dependent ideal contribution $\mu^{\mathrm{id}}(T)$ from the total chemical potential, but includes the density dependent ideal contribution $k_{\mathrm{B}}T \ln \rho$. The acceptance probability P_{acc} for a water molecule insertion writes as [50]

$$P_{acc}(N_{\mathrm{W}} \rightarrow N_{\mathrm{W}} + 1_{\mathrm{W}}) = \min\left(1,\ \frac{V}{N_{\mathrm{W}}+1} \cdot \exp\left\{\frac{\tilde{\mu}_{\mathrm{W}} + [U(N) - U(N+1_{\mathrm{W}})]}{k_{\mathrm{B}}T}\right\}\right), \tag{4.18}$$

where $U(N)$ and $U(N+1_{\mathrm{W}})$ denote the configurational energy of the system with a total number of N molecules and N plus one water molecule, respectively. The acceptance probability for the deletion of a water molecule writes accordingly [50]

$$P_{acc}(N_{\mathrm{W}} \rightarrow N_{\mathrm{W}} - 1_{\mathrm{W}}) = \min\left(1,\ \frac{N_{\mathrm{W}}}{V} \cdot \exp\left\{\frac{-\tilde{\mu}_{\mathrm{W}} + [U(N) - U(N-1_{\mathrm{W}})]}{k_{\mathrm{B}}T}\right\}\right). \tag{4.19}$$

Additionally, the pressure is controlled by sampling the volume like in the standard NpT ensemble. The probability of a volume displacement is then determined by comparison between the resulting potential energy change and the product of specified pressure and volume displacement. The acceptance probability for a volume displacement ΔV is given by [50]

$$P_{acc}(\Delta V) = \min\left(1,\ \left(\frac{V+\Delta V}{V}\right)^{N} \cdot \exp\left\{\frac{p\Delta V + [U(V+\Delta V) - U(V)]}{k_{\mathrm{B}}T}\right\}\right). \tag{4.20}$$

Experience shows that a Mollier ensemble simulation moves rapidly into the vicinity of the dew point. This process occurs well within the equilibration period. During the production period, volume and mole fraction of water fluctuate around the dew point average.

An additional facilitating approximation can be used according to the Grand Equilibrium method, cf. Section 2.4. The pressure dependence of the chemical potential for water is

$$\mu_{\mathrm{W}}(T,p) = \mu_{\mathrm{W}}(T,p_0) + \int_{p_0}^{p} \left(\frac{\partial \mu_{\mathrm{W}}}{\partial p}\right)_T \mathrm{d}p = \mu_{\mathrm{W}}(T,p_0) + \int_{p_0}^{p} v_{\mathrm{W}} \mathrm{d}p\,, \tag{4.21}$$

where p_0 is some reference pressure, say the vapor pressure of pure water, and v_{W} denotes the volume of water. The integral can be approximated by a Taylor expansion around the reference pressure by [114]

$$\mu_{\mathrm{W}}(T,p) = \mu_{\mathrm{W}}(T,p_0) + v_{\mathrm{W},0}(p-p_0) - \frac{1}{2}\beta_{T,0} \cdot v_{\mathrm{W},0}(p-p_0)^2 + \ldots\,, \tag{4.22}$$

where $v_{W,0}$ is the volume and $\beta_{T,0}$ the isothermal compressibility, respectively, of liquid water at the reference pressure p_0. These two properties are easily accessible in the NpT ensemble. The volume is simply

$$v = \frac{< V >}{N} \ , \tag{4.23}$$

where the angular brackets denote the ensemble average. The isothermal compressibility may also conveniently be obtained in the NpT ensemble from volume fluctuations

$$\beta_T = \frac{1}{k_B T} \cdot \frac{1}{< V >} \cdot \left[< V^2 > - < V >^2 \right] \ . \tag{4.24}$$

However, in prior work it was seen that a first order expansion is usually sufficient for moderate pressure extrapolations when the temperature is far below its critical value of the regarded component [217]. As a consequence, the simulation results of a single pure liquid water run can be used for dew point simulations at any given pressure p as long as the approximation above holds.

The Mollier ensemble is derived for humid air here, but may also be used for the determination of the dew point in similar systems, e.g. humid carbon dioxide. However, the application is limited to humid air systems in the present work.

4.5.2.2 Molecular Models for Water

For water, two different molecular models are regarded here. Firstly, the TIP4P model of Jorgensen et al. [85] is used. It consists of four interaction sites, one LJ site located at the oxygen nucleus and three eccentric partial charges to account for hydrogen bonding and the electrostatic interactions. All sites are situated in a plane, cf. Figure 4.14. The TIP4P model was parametrized to reproduce the VLE of pure water, the model parameters are listed in Table 4.3.

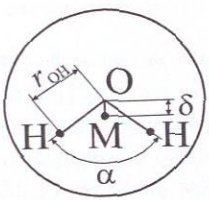

Figure 4.14: Molecular model for water. The LJ site is placed at the oxygen nucleus. The partial charges are denoted by bullets. The positive charges are located at the hydrogen nuclei, while the negative charge is shifted towards the hydrogen nuclei.

Table 4.3: Parameters of the molecular models for water, cf. Figure 4.14.

Model	r_{OH} Å	α °	δ Å	σ Å	ε/k_B K	q e
TIP4P [85]	0.9572	104.52	0.15000	3.15365	78.020	0.52000
Schnabel [171]	0.9670	104.52	0.15004	3.31500	95.646	0.52748

Despite its optimization to VLE data, the TIP4P model shows significant deviations from experimental data in vapor pressure and saturated vapor density. Thus, the water model was reparametrized by Schnabel [171], while keeping the original number of interaction sites. The optimized parameters of the water model of Schnabel are listed in Table 4.3. Simulation results obtained with this water model yield mean unsigned errors compared to experimental VLE data of 20.7, 2.9, and 8.3 % for vapor pressure, saturated liquid density, and enthalpy of vaporization, respectively, while the TIP4P model yields 42.4, 8.9, and 14.6 % [111, 171]. Graphical and numerical simulation results are given in [171].

4.5.2.3 Homogeneous Humid Air Simulations

Klingenberg and Ulbig [94] recently published experimental data on the density of humid air at different state points and different water contents. In the present work, the dry air model is combined with each of the two discussed molecular models for water to predict the density of humid air and compare it to the results from [94]. For the unlike LJ parameters, the standard Lorentz-Berthelot mixing rule is applied, i.e. no additional binary interaction parameters were introduced and ξ is set to unity for all unlike interactions with water, cf. Equations (3.2) and (3.4). Thus, present humid air simulations are fully predictive.

Table 4.4 lists the simulation results in comparison with the experimental data taken from [94]. A very good agreement is reached, yielding deviations below 2.5 % for both utilized water models. There is only a very moderate influence of the chosen water model on the quality of the results. Note that the deviations of the experimental density data from the present simulations are very similar to their deviations from EOS models [64].

4.5.2.4 Dew Point Calculations

The dew point of humid air is calculated using the Mollier ensemble for two isotherms and six pressure levels. The same two quaternary molecular models, differing only in the water model, are used as for the homogeneous humid air simulations. For comparison

Table 4.4: Density of humid air predicted by molecular simulation compared to experimental data [94].

T	p	x_W	ρ_{exp}	ρ_{sim}	$\delta\rho_{sim}$	$\Delta\rho/\rho_{exp}$	$\delta\rho_{sim}/\rho_{exp}$
K	MPa	mol/mol	mol/l	mol/l	mol/l	%	%
TIP4P water model [85]							
424.109	10.87677	0.0420	3.0201	2.980	0.006	-1.34	0.21
524.328	13.68388	0.0420	3.0035	2.965	0.008	-1.27	0.27
498.399	8.89246	0.0446	2.1244	2.074	0.009	-2.39	0.43
498.405	4.38840	0.0445	1.0636	1.042	0.002	-2.04	0.20
423.295	13.74665	0.0126	3.7270	3.697	0.008	-0.81	0.23
515.557	17.04534	0.0126	3.7078	3.702	0.009	-0.16	0.24
water model of Schnabel [171]							
424.109	10.87677	0.0420	3.0201	2.974	0.011	-1.52	0.37
524.328	13.68388	0.0420	3.0035	2.970	0.008	-1.12	0.27
498.399	8.89246	0.0446	2.1244	2.073	0.006	-2.41	0.27
498.405	4.38840	0.0445	1.0636	1.041	0.003	-2.14	0.29
423.295	13.74665	0.0126	3.7270	3.701	0.010	-0.70	0.26
515.557	17.04534	0.0126	3.7078	3.694	0.008	-0.38	0.22

with experimental data, the pressure enhancement factor f_W and the concentration enhancement factor g_W are determined, cf. Equations (4.15) and (4.16).

The equilibrium properties of pure water at the given temperature, i.e. vapor pressure p_W^σ and saturated vapor concentration c_W^0 being identical to the saturated vapor density ρ_W'', are determined in additional VLE simulations for pure water. This is done for both employed water models and the results are given in Table 4.5. Simulation details are briefly discussed in Appendix A.

Table 4.5: Vapor pressure and saturated vapor density of the utilized water models.

T	p_W^σ	ρ_W''
K	MPa	mol/l
TIP4P water model [85]		
333.15	0.045(3)	0.0169(9)
353.15	0.100(3)	0.0355(9)
water model of Schnabel [171]		
333.15	0.015(1)	0.0053(4)
353.15	0.042(2)	0.0146(7)

From the Mollier ensemble simulations, the molar fraction of water x_W and the molar density at the dew point ρ are determined. The partial pressure of water $p_W = x_W \cdot p$ and

the vapor concentration $c_W = x_W \cdot \rho$ can easily be calculated from these. Figures 4.15 and 4.16 show the results for the vapor pressure and vapor concentration enhancement factors, respectively, in comparison to literature data taken from Wiley and Fisher [231] as well as Koglbauer and Wendland [95] and results from the GERG-2004 EOS [103]. Wiley and Fisher provide experimental data on f_W taken by a gravimetric method and Koglbauer and Wendland provide experimental data on g_W taken by FTIR spectrometry. Wiley and Fisher also give results for g_W predicted with a virial EOS model, which they used to correlate their f_W data and that does not compare well to the experimental data by Koglbauer and Wendland below 80 °C (see [95]).

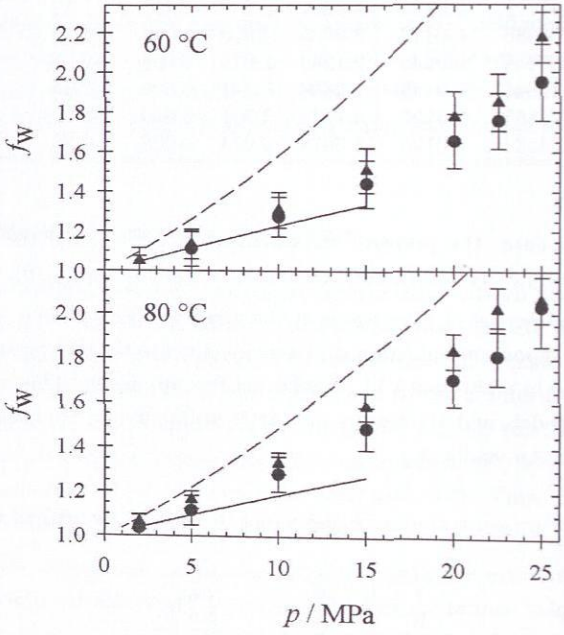

Figure 4.15: Vapor pressure enhancement factor f_W, cf. Equation (4.15). Present simulation data obtained with different water models: ● TIP4P model [85] and ■ model of Schnabel [171]. — correlation of experimental data from Wylie and Fisher [231], – – GERG-2004 EOS [103].

For both water models, the simulation data for vapor pressure enhancement factor and vapor concentration enhancement factor is in agreement with the other two data sets almost throughout within their statistical uncertainties. However, the results with the

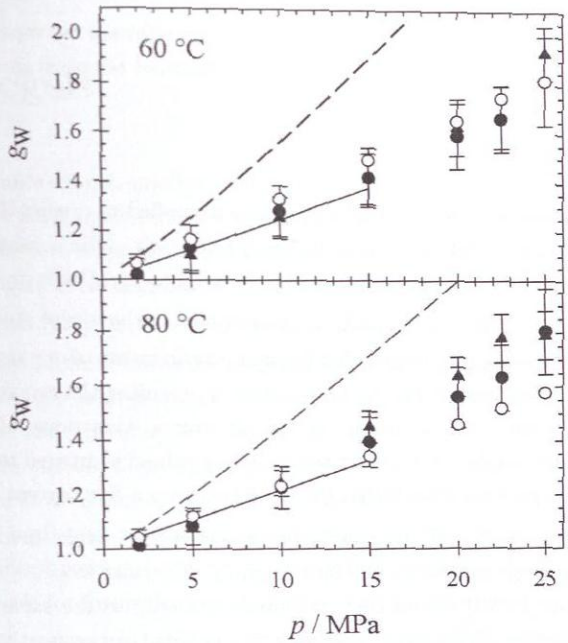

Figure 4.16: Vapor concentration enhancement factor g_W, cf. Equation (4.16). Present simulation data obtained with different water models: ● TIP4P model [85] and ■ model of Schnabel [171]. ○ experimental data from Koglbauer and Wendland [95], — correlation of experimental data from Wylie and Fisher [231], – – GERG-2004 EOS [103].

water model of Schnabel [171] yield a somewhat better agreement. In case of f_W, cf. Figure 4.15, both water models are above the correlation of Wylie and Fishers data [231]. At 60 °C, the water model of Schnabel represents experimental data within the statistical uncertainty and the TIP4P model yields too high results, while at 80 °C both water models overestimate f_W for pressures above 10 MPa, cf. Figure 4.15.

Regarding the vapor concentration enhancement factor g_W, experimental data of Koglbauer et al. [95] and the model of Wylie and Fisher [231] deviate for 60 °C. Molecular simulation yields results that are in between these data sets and agree with both within their statistical uncertainty. At 80 °C, the data sets from the two sources agree quite well with each other, while simulation predicts somewhat higher values. The results from the water model of Schnabel agree with both sources within the statistical

uncertainty, except for 25 MPa, while the TIP4P model yields too high results for g_W for pressures above 10 MPa, cf. Figure 4.16.

The results from the GERG-2004 EOS significantly overestimate the vapor pressure and vapor concentration enhancement factors for both regarded temperatures.

4.5.3 Conclusion

In this section, molecular modeling and simulation is applied to predict thermodynamic properties of humid air. In addition to densities of humid air in the homogeneous region, the dew point at 60 and 80 °C at different pressures up to 25 MPa is predicted.

For dry air, a model is taken from prior work of Vrabec et al. [219] that consists of a combination of three molecular models for the main components of dry air, i.e. nitrogen, oxygen, and argon. This molecular model is assessed regarding the ternary VLE as well as density and residual internal energy of dry air over a wide range of states in the homogeneous gaseous region. Very good results are obtained compared to experimental data and two reference EOS. Generally, the deviations are a few percent or below.

For water, two different models are employed in the present work: firstly, the TIP4P model proposed by Jorgensen et al. [85] and secondly, the water model of Schnabel [171] that is based on the TIP4P model and optimized primarily to the experimental vapor pressure of pure water. Both water models are combined subsequently with the dry air model to simulate humid air. As no further parameters are introduced, the present humid air results are fully predictive.

The humid air density is predicted at different state points and water contents. The results are compared to recent experimental data [94], yielding deviations below 2.5% at the highest water mole fraction.

Finally, the dew point of humid air is predicted using a newly proposed ensemble. This Mollier ensemble is developed in this work specifically for the determination of the dew point in humid gases. The dew point results are also expressed in terms of the vapor pressure enhancement factor f_W and vapor concentration enhancement factor g_W. Compared with experimental data, a satisfactory agreement is obtained for both water models.

With both water models, vapor pressure and vapor concentration enhancement in humid air may adequately be predicted. The water model of Schnabel yields quantitatively correct results in most cases. Compared to experimental data, molecular simulation yields significant better results than the GERG-2004 EOS [103] without any specific adjustment, which underlines the outstanding predictive capability of the method due to its sound physical basis.

5 Hydrogels

Starting from quite simple, small molecules, a benefit of molecular modeling and simulation is that also much more complex molecules can be covered with the same approach. Basically, more effort regarding simulation techniques and computing power is needed only, to investigate even macromolecules. A special class of polymers, hydrogels, are chosen for a short case study in the present work.

Hydrogels are hydrophilic, three-dimensional interlinked polymer networks, which have the ability to strongly swell or shrink. This swelling behaviour depends on the conditions like temperature and pH value, but also on the solvent [55, 62, 73, 74]. Typical solvents are water or aqueous solutions containing salts or polar solvents. The sensitivity of the swelling behaviour of hydrogels allows for a variety of applications, ranging from super absorbers used in diapers to chromatography materials for protein purification or drug release. A detailed knowledge of the thermophysical properties of hydrogels is necessary to tailor hydrogels for future high-performance applications.

Work on hydrogels in the literature is mostly of experimental nature. Only a few theoretical approaches exist, which, however, generally lack in predictive power. Thus, the ability to predict thermophysical properties of real hydrogels by molecular modeling and simulation is worthwhile studying. The aim of the present work in this area is to carry out a first case study in the field, not to reach final conclusions.

5.1 Literature Overview

Experimental work on swelling and shrinking is available for many hydrogels like polyacryl amide (PAA) [90], polyvinyl alcohol (PVA) [156], polyhydroxyethyl methacrylate (HEMA) [24, 158], and poly-n-isopropyl acrylamide (NIPAM) [67]. In case of NIPAM, the hydrogel has also been investigated regarding its swelling behaviour in different solvents like ethanol or sodium chloride solutions [74]. Furthermore, work on hydrogels in electric fields is available [108]. Hirokawa and Tanaka [67] describe two experiments which give interesting data for comparison or tuning of molecular models, cf. Figure 5.1.

To date, only few authors report on the application of molecular methods for determining properties of hydrogels. Both, MC techniques and MD simulations were used. For example, Escobedo and de Pablo performed MC simulations of hydrogels [36, 38].

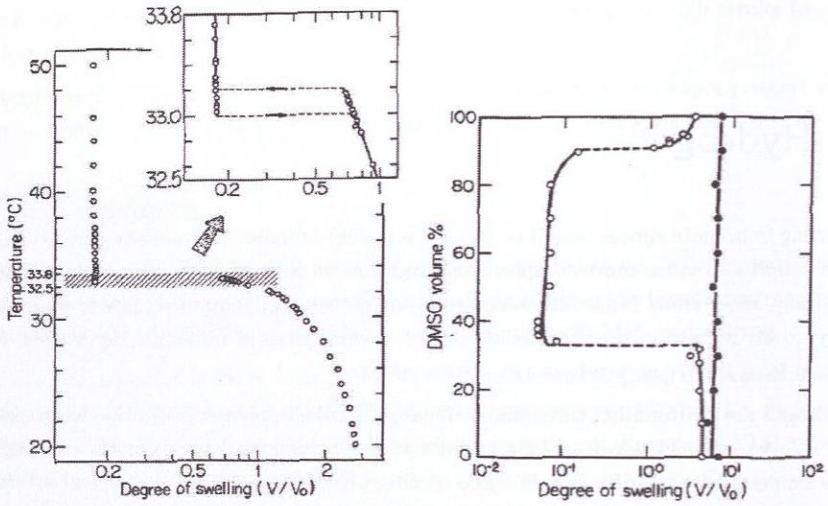

Figure 5.1: Degree of swelling (ratio of the equilibrium volume V to initial volume V_0) of hydrogels at different conditions. (left) Swelling of NIPAM hydrogel in pure water as a function of the temperature. The inset shows the hysteresis of the discontinuous volume transition in greater detail. (right) Swelling of hydrogels in a mixture of water and dimethyl sulfoxide (DMSO) as a function of the solvent composition: ○ NIPAM hydrogel, ● PAA hydrogel. The plots are taken from [67].

Therby, the hydrogel polymer networks were modeled by hard sphere chains without electrostatic interactions in a strongly simplified manner. The aim of the simulations was the development of reasonable sampling techniques and a theoretical investigation of the influence of the potential parameters of hydrogel and solvents. A description of real hydrogels and solvents was not within the scope of that work.

Netz and Dorfmüller [143, 144] simulated the behavior of a tracer particle in the vicinity of a statically preset hydrogel structure by MC. The intermolecular interactions were modeled by hard sphere potentials as well. They observed a strong variation of the diffusive properties of the tracer particle in the hydrogel compared to the bulk phase.

In contrast to these more theoretical approaches, real hydrogels were considered by MD simulations. Müller-Plathe et al. [135] and Tamai et al. [200] simulated long linear PVA hydrogel chains in aqueous solutions. They drew conclusions on the swelling of PVA hydrogels from the amount and type of hydrogen bonds formed between solvent and hydrogel. In further works, this method was extended to polyvinyl methylether and NIPAM hydrogels [197–199] and an alternative molecular model for the solvent water

[201].

Chiesi et al. [18] introduced two-dimensional covalent interlinks in their hydrogel simulation. The considered PVA hydrogel was connected with itself through the periodic boundary condition. Thus, an infinite hydrogel was simulated but without any possibility to swell or shrink due to the periodicity. Analogously to the work of Tamai et al., the behaviour of solvent molecules in the vicinity of the hydrogel was analyzed.

A realistic, three-dimensional interlinked hydrogel was simulated by Oldiges et al. [150, 151]. Hydrogel monomers were statistically arranged on a tetrahedral lattice and linked with each other. Subsequently, the residence time of a solvent mixture of water and acetonitrile in a PAA hydrogel was determined and the influence of the irregular hydrogel structure was identified.

Netz et al. [145] also investigated a PAA hydrogel of this type. They varied the number of water and hydrogel molecules within their simulation box and analyzed the residence time of hydrogen bonds in every case.

In the previously discussed publications, no realistic intermolecular potentials were applied for the MC simulations. In case of MD simulations, realistic potentials were used, which were mostly built from the well-known force fields AMBER [22] or GROMOS [153] for the polymer chains or taken from literature for the solvents.

To our knowledge, no direct simulation on the dynamics of swelling or shrinking of hydrogels was published so far. Instead, most authors try to deduce the swelling from other properties, like the amount of hydrogen bonds or the variation of diffusivity of the solvent in vicinity of the hydrogels.

5.2 Modeling Approach

The present work attempts to directly simulate the dynamics of swelling and shrinking of hydrogels. Therefore, a hydrogel cube is regarded, which is built from hydrogel monomers. By not interconnecting this cube across the simulation volume boundaries, the hydrogel cube is able to shrink or swell freely.

The simulation volume is chosen to be large enough to prevent an interaction of the hydrogel with its replicas via the periodic boundary condition. This is done by specifying the size of the simulation volume to be larger than the size of the fully swollen hydrogel plus two times the half of the cutoff radius at each side. Figure 5.2 shows an example for such an initial configuration of the observed hydrogel within the simulation volume. Subsequently, the volume is filled with solvent molecules before the simulation is started.

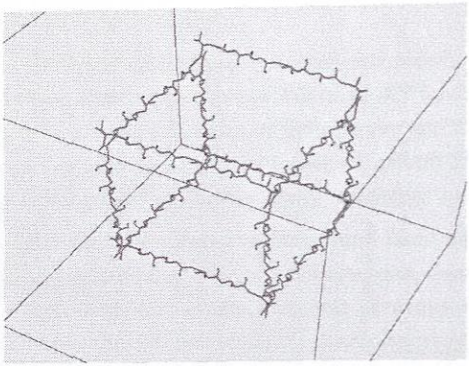

Figure 5.2: Initial configuration of a hydrogel in present simulations. The water molecules are omitted for clarity.

The hydrogel is modeled by interconnecting predefined monomers along the cuboid backchain. The regarded monomers are vinyl alcohol (C_2H_4O), acrylamide (C_3H_5NO), and isopropyl acrylamide ($C_5H_{11}NO$) for the hydrogels PVA, PAA, and NIPAM, respectively. A detailed description of the building process is given elsewhere [169]. The molecular model parameters for the bonded and non-bonded interactions are taken from the GROMOS force field [153]. The electrostatic interactions are modeled by partial charges according to the GROMOS force field. Unfortunately, the force field gives no clear route to determine the partial charges in this case. On one side, there is a standard approach using additive partial charges per atom and/or bond, while on the other side, there are optimized charges for atoms in various protein groups. For the different variants of the force field, different properties of the hydrogels were observed as discussed in the following. A further optimization of the model charges, e.g. to results from QM calculations, cf. Chapter 3, or to macroscopic thermodynamic properties, is unavoidable, but is not within the scope of the present work. Here, only some preliminary studies are presented showing the general feasibility to investigate hydrogels by molecular modeling and simulation.

Figures 5.3 and 5.4 show the sets of partial charges for the different monomers used in the present work. The first (weaker) set of partial charges, shown in Figure 5.3, is derived using the defaults implemented in the GROMOS force field. The second (stronger) set of partial charges, shown in Figure 5.4, is derived including optimizations for protein models from the GROMOS force field. A comparison of the charges on vinyl alcohol, (a) in Figures 5.3 and 5.4, with the molecular model for ethanol presented by Schnabel et al. [174], cf. Figure 5.5, demonstrates that the GROMOS force field gives in both cases significantly lower charges than an optimization to experimental VLE data on similar

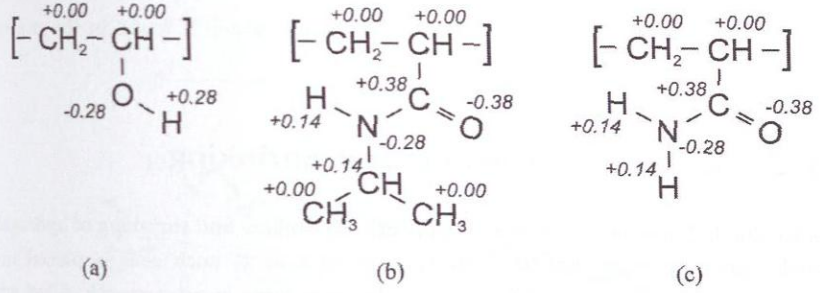

Figure 5.3: Partial charges (weak set) in terms of elementary charges e on the model monomers obtained from the GROMOS force field [153]: (a) vinyl alcohol, (b) acrylamide, and (c) isopropyl acrylamide.

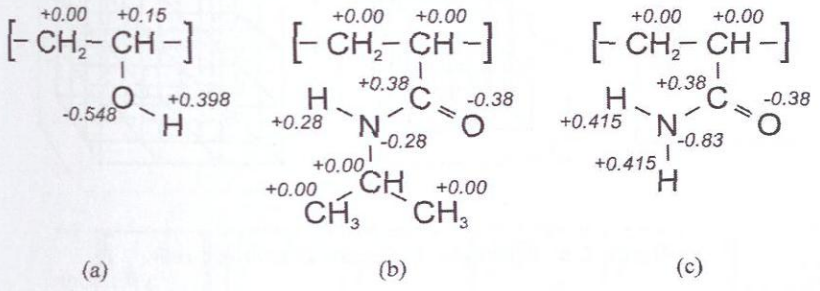

Figure 5.4: Partial charges (strong set) in terms of elementary charges e on the model monomers obtained from the GROMOS force field [153]: (a) vinyl alcohol, (b) acrylamide, and (c) isopropyl acrylamide.

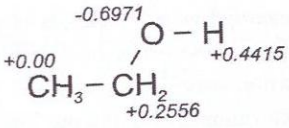

Figure 5.5: Partial charges in terms of elementary charges e on the ethanol model presented by Schnabel et al. [174].

molecules.

This may be a reason for the too low affinity to water, which is found in the present simulations described in the following section.

5.3 Simulation of Swelling and Shrinking

A direct simulation approach is used to simulate the swelling and shrinking of hydrogels. A single cuboid hydrogel cell or a combination of 8 or 27 such cells is placed in a simulation volume, cf. Figure 5.6. The simulation volume is subsequently filled with solvent molecules, mostly water, at the desired density. The simulation is run with the technical details given in Appendix A and the volume of the hydrogel cube is recorded, cf. Figure 5.7 for example.

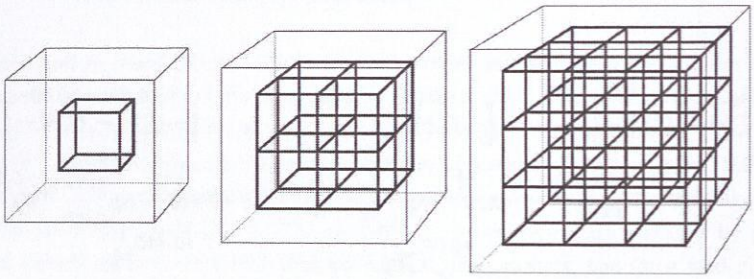

Figure 5.6: Schematic of the model hydrogel cells.

As the complete process of swelling or shrinking of a hydrogel exceeds the time scale accessible by a single molecular simulation, the process is separated along its time scale. A series of hydrogel simulations is prepared, containing the same hydrogel configuration at different initial volumes of the hydrogel cube. The different initial volumes are generated by dragging the hydrogel corners to specific positions during the equilibration period.

This series of simulations is regarded as sub-intervals of the full swelling or shrinking process. If a decreasing volume is observed, a new simulation is started with a lower initial volume until an equilibrium state is reached, and vice versa. Figure 5.8 shows such a series of simulations each running over 150 ps. The equilibrium state found here indicates shrinking.

In contrast to experimental observations, no swelling of the investigated hydrogels is found by molecular simulation here. In a single case, a stable swollen configuration is found for an eight-cell PAA hydrogel, cf. Figure 5.9. This hydrogel is modeled with

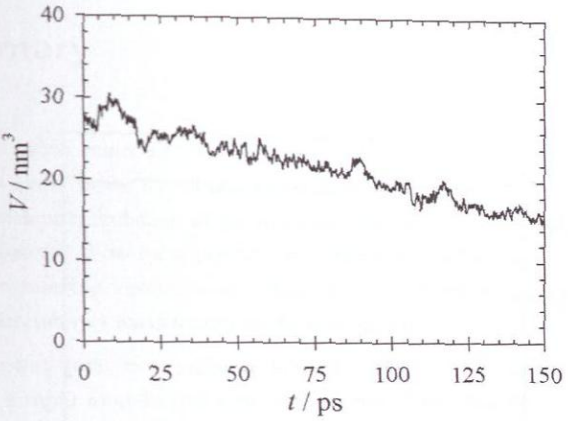

Figure 5.7: Volume transition of a PVA hydrogel in TIP4P water at 303 K.

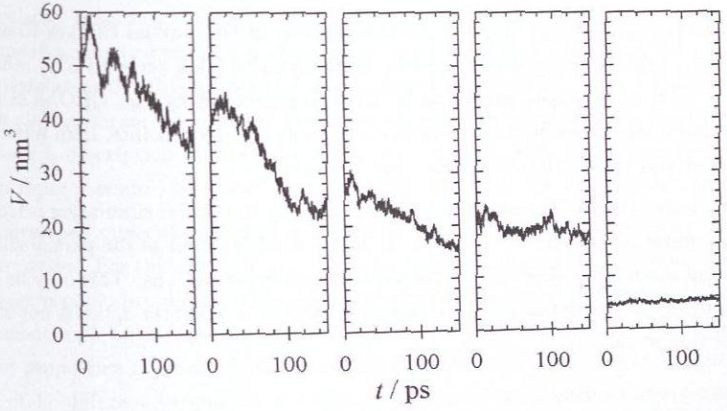

Figure 5.8: Series of simulations of a PVA hydrogel starting from different initial volumes in TIP4P water at 303 K.

the stronger set of partial charges, cf. Figure 5.4, whereas the PAA hydrogel modeled with the weaker set is stable only in the shrunken condition. Variations in temperature, hydrogel size, number of connected hydrogel cells, cf. Figure 5.6, and box size are checked and show only minor, insignificant influence.

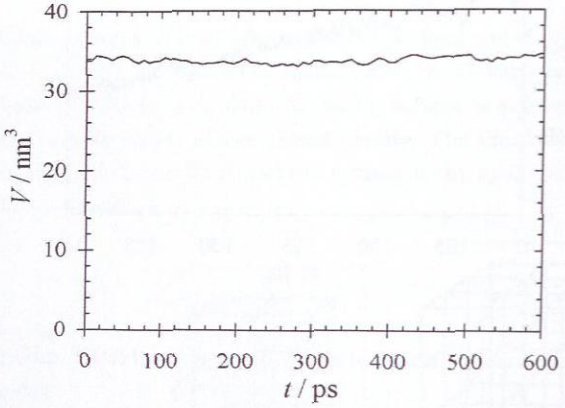

Figure 5.9: Stable swollen configuration observed for an eight-cell PAA hydrogel with stronger polarity, cf. Figure 5.4, in TIP4P water at 303 K.

This supports the assumption derived by comparison of the partial charges from the GROMOS force field to the ones obtained by adjustment to VLE properties for ethanol. The polarity of the hydrogels seems to be underrepresented by the GROMOS force field. Thus, the interactions between the hydrogel and the polar solute, here water, are underpredicted and the model hydrogels tend to shrink.

It can be concluded that an investigation of hydrogels by molecular simulation is feasible applying the presented methods. However, a detailed adjustment of the partial charges of the hydrogel models is necessary to yield quantitative predictions. This may be done analogously to the model development strategy presented in Chapter 3, but is not within the scope of this work.

6 Summary

Starting in the 1950s, molecular modeling and simulation became a tool not only for a qualitative but quantitative determination of thermophysical properties. With the same models, a consistent calculation of microscopic and macroscopic properties is possible. Recent developments allow for a prediction of these properties with accuracies that are valuable for engineering applications. However, a disadvantage of the method is the scarcity of quantitatively satisfactory molecular models.

Within the present work, two goals are followed: Firstly, a parametrization strategy is developed for a rapid modeling of new substances. This strategy relies on the use of results of quantum mechanical calculations in the parametrization process. Secondly, molecular modeling and simulation is applied to predict a variety of thermophysical properties of different substances and mixtures. In an outlook, the application of molecular modeling and simulation to hydrogels is presented.

New molecular models are developed for at total 13 different pure substances from different substance classes. These are iso-butane, cyclohexane, formaldehyde, dimethyl ether, sulfur dioxide, dimethyl sulfide, thiophene, hydrogen cyanide, acetonitrile, nitromethane, ammonia, ethylene oxide, and 1,1,1,2,3,3,3-heptafluoropropane. For their parametrization, a combination of quantum mechanics and optimization to experimental VLE data is used. This allows the development of physically sound molecular models, which yield accurate microscopic and macroscopic thermophysical properties. In almost all cases, a description of the experimental VLE data with deviations below 5, 1, and 5 % in vapor pressure, saturated liquid density, and enthalpy of vaporization is achieved.

The developed molecular models are subsequently used to predict further thermophysical properties. For the example ammonia, an application to the prediction of microscopic and macroscopic properties with the same molecular model is presented. An excellent agreement with both experimental radial distribution functions as well as thermal and caloric properties from a reference quality EOS is found. In case of ethylene oxide, a total of 17 different properties are calculated including transport properties and surface tension. Again, a very good agreement with experimental and reference data was seen. These examples underline the excellent transferability of molecular models for the prediction of various thermophysical properties.

An application to mixtures is presented for the binary mixture heptafluoropropane

(R227ea) and ethanol as well as for the quaternary system humid air. In the binary mixture R227ea + ethanol, special unlike intermolecular interactions are present. These cause, e.g., the Peng-Robinson EOS to fail in describing the experimental VLE data. Molecular modeling and simulation is able to predict the phase coexistence correctly in a strictly predictive manner. The vapor pressure predicted from pure component's data alone agrees well with experimental data over the full composition range.

Properties of humid air are discussed in Section 4.5. For dry air, modeled as the ternary system nitrogen + oxygen + argon, thermophysical properties are predicted covering a wide range of states with accuracies comparable or better than recommended EOS. Also the density of humid air at elevated pressures was calculated, which agrees with experimental data within a maximum deviation of 3 %. For the determination of the dew point of humid air, a new pseudo-ensemble is developed. With this Mollier ensemble, the dew point is predicted, being in good agreement with experimental results.

An outlook to the application of molecular modeling and simulation to hydrogels is given as the conclusion of this work. For simplicity, predefined force fields from the literature are used here. The method allows a direct evaluation of the swelling properties of hydrogels and thus opens a new route for an optimal design of hydrogels. For quantitative predictions, an adjustment of the molecular models is unavoidable, but is not in the scope of this work.

With the presented simulation results, namely the prediction of vapor pressure of the binary mixture R227ea + ethanol and the calculation of 17 different thermophysical properties of ethylene oxide, we participated in the third and fourth International Fluid Properties Simulation Challenge in 2006 and 2007. The Simulation Challenge is an annual contest in the field of molecular modeling and simulation announced by a collaboration between industry and academia coordinated by the National Institute of Standards and Technology (NIST). After being the second entry on the mixture R227ea + ethanol in 2006, the contribution on the properties of ethylene oxide was announced Champion of the Simulation Challenge in 2007.

In summary, it may be stated that molecular modeling and simulation definitely opens new perspectives for the correlation and prediction of thermophysical properties. In contrast to many phenomenological correlations, molecular modeling and simulation yields an approach for a consistent description of different properties by a single (molecular) model. The method can be applied to small and large molecules as well as to mixtures. However, there is still a considerable amount of work to be done. Additional molecular models must be developed for various pure substances and mixtures that are both accurate and simple. And, of course, molecular modeling and simulation must further be applied to technical problems in process engineering, to establish the method for industrial use.

Appendix

A Simulation Details

A.1 Molecular Models of Real Fluids

All molecular models presented in this work are optimized to experimental VLE data of the pure fluids. For the optimization, correlations to experimental vapor pressure, saturated liquid density, and enthalpy of vaporization taken from [165] are used. The optimization procedure, which is applied here, is outlined in Section 3.3.

The Grand Equilibrium method [217] is employed throughout this work to calculate VLE data on the basis of the models at seven to thirteen temperatures from 50 to 97 % of the critical temperature during the optimization process, cf. Appendix B. For the liquid, usually MD simulations are performed in the isobaric-isothermal (NpT) ensemble using isokinetic velocity scaling [3] and Andersen's barostat [5]. There, the number of molecules is 864 throughout and the time step is 0.5 to 3 fs. The length of the time step depends on the molecular weight and the magnitude of the intermolecular interactions and is shorter for lighter and stronger interacting molecules, e.g. ammonia. Starting from a face centered cubic lattice as initial configuration, the fluids are equilibrated over 25 000 time steps with the first 5 000 time steps in the canonical (NVT) ensemble. The production run time span is 150 000 to 200 000 time steps with a membrane mass of 10^9 kg/m^4. In standard cases, Widom's insertion method [228] is used to calculate the chemical potential by inserting up to 4 000 test molecules every production time step.

In cases, where Widom's insertion method yields large statistical uncertainties for the chemical potential, i.e. at high densities for strongly interacting molecules, MC simulations are performed in the NpT ensemble for the liquid. Then, the chemical potential is calculated by the gradual insertion method [147, 212], cf. Section 2.3.2. Here, the number of molecules is typically 500. Starting from a face centered cubic lattice, 15 000 MC cycles are performed for equilibration and 50 000 for production, each cycle containing 500 translation moves, 500 rotation moves, and 1 volume move. Every 50 cycles, 5000 fluctuating state change moves, 5000 fluctuating particle translation and rotation moves, and 25000 biased particle translation/rotation moves are performed, to determine the chemical potential. These computationally demanding simulations yield the

chemical potential in dense and strong interacting liquids with high accuracy, leading to reasonable uncertainties in the VLE.

For the corresponding vapor, MC simulations in the pseudo-μVT ensemble are performed. The simulation volume is adjusted to lead to an average number of 500 molecules in the vapor phase. After 1 000 initial NVT MC cycles, starting from a face centered cubic lattice, 10 000 equilibration cycles in the pseudo-μVT ensemble are performed. The length of the production run is typically 50 000 cycles, in selected cases up to 100 000. One cycle is defined here to be a number of attempts to displace and rotate molecules equal to the actual number of molecules plus three insertion and three deletion attempts.

The cut-off radius is set to at least 17.5 Å throughout and a center of mass cut-off scheme is employed. Within the cut-off radius, all interactions are calculated explicitly. LJ long-range interactions beyond the cut-off radius are corrected employing angle averaging as proposed by Lustig [116]. Electrostatic interactions are approximated by a resulting molecular dipole and corrected using the reaction field method [3].

Statistical uncertainties of the simulated values are estimated by a block averaging method [49]. The total uncertainty of combined results is calculated from the uncertainties of the individual factors using the error propagation law.

A.2 Applications in Process Engineering

Thermal and Caloric Properties of Ammonia For the simulations of ammonia in the homogeneous region, MD simulations are performed in the NpT ensemble using isokinetic velocity scaling [3] and Anderson's barostat [5]. There, the number of molecules is 864 and the time step is 0.58 fs. The simulations are equilibrated over 120 000 time steps with the first 20 000 time steps in the canonical (NVT) ensemble. The production runs go over 300 000 time steps with a membrane mass of 10^9 kg/m^4.

For the radial distribution functions, a MD simulation is performed with 500 molecules. Intermolecular site-site distances are divided in 200 slabs from 0 to 13.5 Å and summed up for 50 000 time steps.

Isobaric Heat Capacity and Isothermal Compressibility of Ethylene Oxide For the calculation of isobaric heat capacity c_p and isothermal compressibility β_T of ethylene oxide, MD simulations in the NpT ensemble are performed at the saturated state points with $N = 1372$ throughout. Starting from a face centered cubic lattice, 55 000 equilibration steps are made, followed by 300 000 production time steps of 2.5 fs for liquid phases and 500 000 production time steps for vapor phases.

For the calculation of β_T in the vapor phase, it is crucial to choose the correct membrane mass of Anderson's barostat. Too high values lead to volume oscillations with a large wavelength and consequently to large statistical uncertainties (10^5 kg/m^4) or even wrong results (10^8 kg/m^4) for β_T, cf. Figure A.1. Here, a membrane mass of $5 \cdot 10^3$ kg/m^4 for the present model and $2.5 \cdot 10^3$ kg/m^4 for the model of Wielopolski and Smith [230] are chosen.

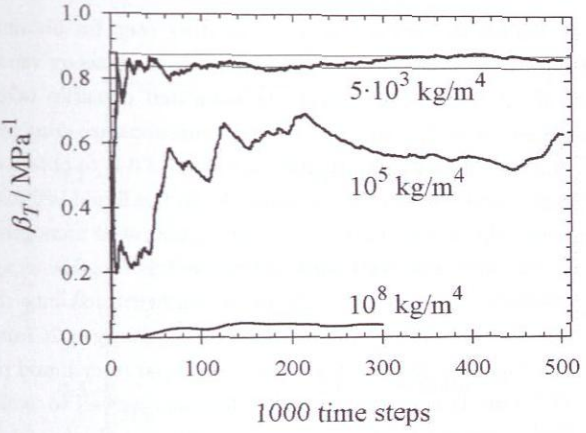

Figure A.1: Running average of the isothermal compressibility β_T for the present model for different membrane mass parameters of Anderson's barostat in the saturated vapor at 375 K. Horizontal lines indicate the statistical uncertainty.

Transport Properties of Ethylene Oxide *Equilibrium* MD simulations are performed in the NVT ensemble with $N = 500$ at the saturated densities from VLE calculations. The cut-off radius is set to 17.5 Å throughout and long-range corrections are applied as described in Section A.1. Liquid state simulations are equilibrated for 50 000 time steps and 300 000 time steps for production are performed with 1.25 fs. During the production phase, 3 000 autocorrelation functions (ACF) are evaluated. To sample independent ACF, the time span between two consecutive functions is set to 0.13 ps. After this period, the normalized ACF decayed to far less than $1/e \approx 0.368$, cf. Figure A.2. Thus, their statistical independence may be assumed and a new ACF is evaluated. The time span of the ACF is set to 6.4 ps, as the integral showed stationary behaviour within the statistical uncertainty, cf. Figure A.3, which is calculated by a block averaging method

[48].

For the vapor phase much longer ACF must be evaluated, as they show a significant long time behaviour due to the low density. The length of the ACF is set to 50 ps. The time span between two ACF is kept at 0.13 ps, as this is adequate also in the vapor state. To sample the ACF with a higher resolution, the time step of the simulation is reduced to 0.65 fs. A total of 4 500 ACF are evaluated, leading to a production period of 1 000 000 time steps.

Surface Tension of Ethylene Oxide As a preparatory step for obtaining an adequate initial configuration, a homogeneous liquid and a homogeneous vapor phase are simulated independently in a cuboidal volume at saturated densities taken from the homogeneous VLE simulations, cf. Table B.1. Both simulations are done by MD in the NVT ensemble starting from a lattice for 10 000 time steps of 3 fs to obtain equilibrated vapor and liquid phases, where the number of molecules in the liquid is 5 324 and in the vapor is 2 048. The molecular configurations of these equilibrated homogeneous phases are then used to construct an initial configuration for the inhomogeneous system. This is done by putting a cube of length l from the liquid configuration into the center of the inhomogeneous system and adding a cuboidal volume of length $2l$ from the vapor configuration on both sides of the liquid. Note that the preparatory liquid phase is simulated in a volume with exactly a size l in x and y direction as well to avoid molecular overlaps over the periodic boundary. The system size is chosen to be $l = 66$ Å, the liquid contained approximately 2 900 molecules and the vapor 400 molecules (present model of ethylene oxide) or 600 molecules (model of Wielopolski and Smith [230]). Molecular overlaps between the phases are avoided and relative positions as well as velocities are conserved within each phase. Starting from such initial configurations, MD simulations of inhomogeneous systems have a mechanical stability which is satisfactory.

Planar interface VLE calculations are carried out in the isokinetic NVT ensemble with 200 000 equilibration time steps, followed by a production phase of 1 500 000 time steps. To adequately simulate the VLE directly, it is usually necessary to account for the inhomogeneity of the fluid through long-range corrections. For the dispersive interaction, being modelled here by the LJ potential, often significant long-range contributions both to the dynamics of the system and to the thermodynamic properties have to be considered [113]. Several correction schemes have been proposed in the literature [79, 177] to address this issue. Also for the dipolar interaction expressions for long-range contributions are available, e.g., based on Ewald summation technique [127]. However, in the present work, a brute force approach is preferred to the programming effort, simulating both molecular models for different (large) cut-off radii between 12 and 25 Å. They are chosen to be up to 6.8-fold of the largest LJ size parameter σ. Simulations by Mecke

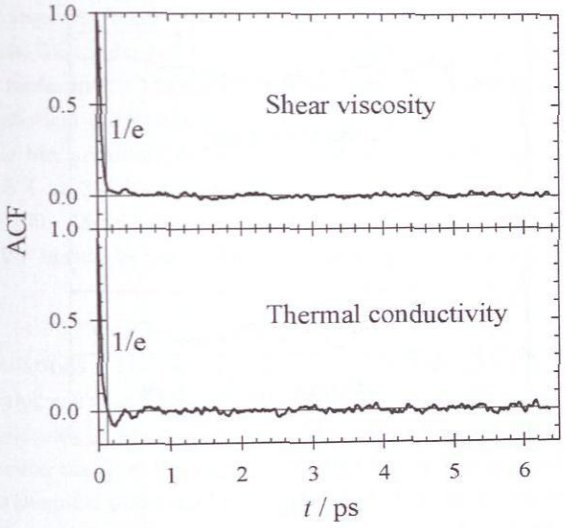

Figure A.2: Normalized autocorrelation functions (ACF) for shear viscosity and thermal conductivity for the present model of ethylene oxide, *cf.* *Table* 3.5, in the saturated liquid at 375 K. The vertical line denotes $t = 0.13$ ps, where both ACF have decayed far below $1/e \approx 0.368$.

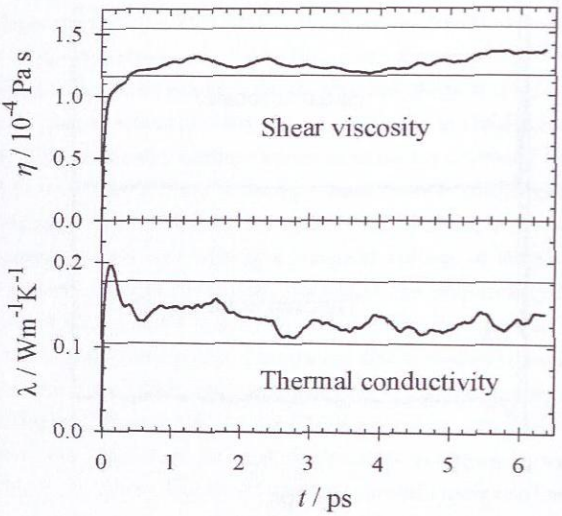

Figure A.3: Shear viscosity and thermal conductivity as integrated over the respective autocorrelation functions for the present model of ethylene oxide, cf. Table 3.5, in the saturated liquid at 375 K. The vertical lines indicate statistical uncertainties.

et al. [128] suggest that for $r_c \geq 6.5\sigma$ long-range contributions only play a little role. From the simulation results the behaviour at *infinite cut-off radius* is extrapolated.

Binary Mixture R227ea + Ethanol For the determination of the binary VLE of the mixture R227ea + ethanol, the same methods are applied as described above for the VLE of pure fluids. The number of molecules in the liquid runs is 1372 throughout and the time step is 1.7 fs. Following an equilibration over 21 000 time steps with the first 1 000 time steps in the canonical (NVT) ensemble, the production run goes over 600 000 time steps with a membrane mass of 10^8 kg/m^4 for the liquid. Widom's insertion method [65, 228] is used to calculate the chemical potentials and the partial molar volumes in the liquid by inserting 5488 test molecules every time step for each component. At all state points, four independent liquid simulation runs with slightly different initial densities are performed. The four resulting data sets are averaged to obtain results with lower statistical uncertainties. It has to be pointed out that the simulation effort is considerable but necessary for this mixture to achieve vapor pressure error bars in the range of 5 % at 343.13 K. The number of molecules for vapor phase simulations is on average 700. After 1 000 initial NVT MC cycles, 10 000 equilibration cycles in the pseudo-μVT ensemble are performed. The length of the production run is 300 000 cycles.

Dry Air Simulations The ternary VLE in the mixture nitrogen + oxygen + argon is calculated analogously to the binary mixture R227ea + ethanol described above. The number of molecules is 864 throughout. The production period is 200 000 time steps with a membrane mass of 10^8 kg/m^4. Widom's insertion method [228] is applied to determine the chemical potential by inserting 3 200 test molecules of every species every production time step. For the corresponding vapor, MC simulations in the pseudo-μVT ensemble are performed. The simulation volume is adjusted to lead to an average number of 500 molecules in the vapor phase, while the length of the production run is 100 000 cycles.

For the homogeneous dry air simulations, MD is applied with the same technical details as used for the saturated liquid runs, except the insertion of test molecules. The results are thoroughly checked to avoid any drifts over the simulation course.

Properties of Humid Air The homogeneous humid air simulations, cf. Table 4.4, are done by MD simulations. For production, 200 000 time steps of 1.18 fs are performed in the NpT ensemble.

For the determination of the dew points of humid air, pure liquid water simulations are done with both regarded molecular water models at the desired temperature and

the corresponding vapor pressure of water. The MC method is applied and gradual insertion is used to calculate the chemical potential of water [212]. Starting from a face centered cubic lattice containing 864 water molecules, 15 000 Monte Carlo cycles are performed for equilibration and 50 000 for production, each cycle containing 864 translation moves, 864 rotation moves, and 1 volume move. Every 50 cycles 5 000 fluctuating state change moves, 5 000 fluctuating particle translation and rotation moves, and 25 000 biased particle translation and rotation moves are performed, to measure the chemical potential.

The corresponding vapor phase at the dew point is determined by MC simulations in the proposed Mollier ensemble, cf. Section 4.5.2.1. The number of number of molecules of the dry air components nitrogen, oxygen, and argon in the vapor phase is set to 2000. In case of low water mole fractions, the dry air molecules are increased to 4 000 for improved statistics. Again, starting from a face centered cubic lattice, 15 000 Monte Carlo cycles are performed for equilibration and 50 000 for production, each cycle containing N translation moves, N rotation moves, 1 volume move as well as 2 insertion and 2 deletion attempts of a water molecule, where N is the actual particle number.

A.3 Hydrogels

All hydrogel simulations are performed with MD using the GROMACS simulation package [184]. The hydrogel polymer itself contained 1 000 to 12 000 interaction sites depending on the type, cuboid size, and number of hydrogel cuboids regarded. The hydrogel is solvated in a simulation volume with periodic boundary conditions, where the size of the simulation volume is chosen to prevent an interaction of the hydrogel cuboid with its own replicas. The simulation volume is filled with solvent molecules, mostly water, at the experimental density yielding 8 000 to 25 000 solvent molecules.

After some energy minimization loops to avoid molecular overlaps from the initialization, the system is equilibrated for about 100 ps in the NVT ensemble with a time step of 1 fs. The corners of the hydrogel cube are fixed in space during equilibration to keep the hydrogen volume constant. In the subsequent production period, these constraints are turned off to allow swelling or shrinking. Production runs went over 100 to 500 ps.

During production, the hydrogel volume is recorded by calculating the average distance between the hydrogel backchain atoms and the center of mass of the hydrogel. The volume is reported in this work as the volume of a sphere with a radius equal to that average distance.

B Numerical Simulation Results

Table B.1: VLE data of the modeled substances: present simulation data compared to correlations of experimental data [165] or reference EOS [202] (in case of ammonia) for vapor pressure, saturated densities, and enthalpy of vaporization. The number in parentheses indicates the statistical uncertainty in the last digit.

T	p_σ^{sim}	p_σ^{exp}	ρ'_{sim}	ρ'_{exp}	ρ''_{sim}	$\Delta h_{\mathrm{v}}^{\mathrm{sim}}$	$\Delta h_{\mathrm{v}}^{\mathrm{exp}}$
K	MPa	MPa	mol/l	mol/l	mol/l	kJ/mol	kJ/mol
iso-butane							
150			12.15(1)	12.149			
200			11.28(1)	11.325			
270	0.14(1)	0.140	9.98(1)	10.050	0.067(6)	20.80(3)	20.811
300	0.37(2)	0.370	9.37(1)	9.420	0.164(7)	19.10(3)	19.006
320	0.59(2)	0.633	8.88(2)	8.955	0.254(8)	17.80(4)	17.591
335	0.87(2)	0.906	8.54(2)	8.575	0.37 (1)	16.72(4)	16.375
350	1.30(3)	1.258	8.10(3)	8.159	0.58 (1)	15.16(6)	14.980
365	1.74(3)	1.701	7.69(3)	7.688	0.79 (1)	13.76(6)	13.325
380	2.21(3)	2.252	7.05(5)	7.113	1.03 (2)	11.89(9)	11.240
390	2.77(3)	2.689	6.59(9)	6.609	1.44 (2)	9.9 (1)	9.408
cyclohexane							
300			9.13(0)	9.174			
330	0.02(1)	0.046	8.80(0)	8.831	0.013(3)	31.49(1)	31.339
360	0.12(1)	0.121	8.45(0)	8.476	0.041(4)	29.89(1)	29.589
390	0.27(2)	0.267	8.09(1)	8.101	0.088(5)	28.19(2)	27.646
415	0.51(2)	0.467	7.77(1)	7.767	0.165(7)	26.50(3)	25.828
440	0.75(2)	0.763	7.41(1)	7.404	0.240(7)	24.78(3)	23.758
460	1.08(2)	1.085	7.12(1)	7.083	0.343(6)	23.18(4)	21.853
480	1.48(2)	1.496	6.76(3)	6.723	0.478(7)	21.27(5)	19.647
500	2.01(2)	2.012	6.38(2)	6.305	0.68 (1)	18.99(7)	17.027
515	2.44(2)	2.478	5.97(3)	5.935	0.85 (1)	16.92(9)	14.675
535	3.29(2)	3.223	5.44(6)	5.280	1.31 (2)	13.1 (1)	10.566

continued on next page

continued from previous page

T	p_σ^{sim}	p_σ^{exp}	ρ'_{sim}	ρ'_{exp}	ρ''_{sim}	$\Delta h_{\mathrm{v}}^{\mathrm{sim}}$	$\Delta h_{\mathrm{v}}^{\mathrm{exp}}$
K	MPa	MPa	mol/l	mol/l	mol/l	kJ/mol	kJ/mol
formaldehyde							
250	0.103(1)	0.085	27.81(3)	27.50	0.053(1)	22.41(4)	23.30
300	0.582(2)	0.549	24.83(4)	24.40	0.273(3)	19.49(5)	20.80
330	1.327(6)	1.271	22.69(4)	22.30	0.617(7)	17.22(5)	18.90
350	1.99 (7)	2.058	21.11(5)	20.60	0.95 (7)	15.6 (2)	17.30
370	3.03 (7)	3.180	18.92(7)	18.70	1.53 (8)	13.2 (2)	15.30
385	4.12 (7)	4.298	16.7 (1)	16.90	2.24 (9)	10.9 (2)	13.20
390	4.49 (9)	4.732	15.8 (2)	16.20	2.5 (1)	10.2 (3)	12.20
dimethyl ether							
160			18.25(1)	18.209			
200			17.17(1)	17.189			
280	0.32(3)	0.335	14.79(1)	14.844	0.15(1)	19.90(1)	19.896
300	0.64(3)	0.623	14.11(1)	14.156	0.29(1)	18.57(2)	18.623
320	1.09(2)	1.065	13.39(1)	13.401	0.49(1)	17.11(2)	17.124
335	1.53(4)	1.523	12.80(2)	12.772	0.70(1)	15.86(2)	15.806
350	2.18(3)	2.110	12.11(3)	12.067	1.02(1)	14.29(4)	14.262
365	2.83(3)	2.843	11.27(3)	11.242	1.36(2)	12.65(5)	12.391
380	3.86(3)	3.742	10.31(7)	10.196	2.09(3)	10.1 (1)	9.950
390	4.57(3)	4.444	9.6 (2)	9.215	2.69(4)	8.3 (1)	7.625
sulfur dioxide							
240	0.04(1)	0.032	23.945(3)	23.664	0.018(4)	26.40(1)	26.197
255	0.09(1)	0.069	23.327(3)	23.085	0.043(4)	25.53(1)	25.375
270	0.15(1)	0.136	22.694(3)	22.488	0.069(4)	24.71(1)	24.521
285	0.24(1)	0.247	22.043(4)	21.869	0.106(6)	23.85(1)	23.623
300	0.40(4)	0.417	21.357(8)	21.222	0.17 (1)	22.88(1)	22.667
330	1.03(3)	1.013	19.88 (1)	19.816	0.44 (1)	20.57(1)	20.511
360	2.09(3)	2.098	18.17 (2)	18.190	0.90 (2)	17.83(3)	17.867
390	3.85(4)	3.873	15.98 (4)	16.166	1.80 (3)	14.20(7)	14.354
405	5.17(3)	5.095	14.53 (6)	14.855	2.66 (3)	11.50(7)	11.967
dimethyl sulfide							
250			14.385(3)	14.390			
302	0.070(2)	0.075	13.448(7)	13.492	0.028(1)	26.43(1)	27.607
333	0.210(5)	0.208	12.865(8)	12.906	0.080(2)	25.02(2)	25.917
363	0.47 (1)	0.465	12.233(8)	12.288	0.169(4)	23.41(2)	24.086
383	0.74 (1)	0.735	11.809(7)	11.841	0.261(5)	22.27(2)	22.726
403	1.11 (2)	1.109	11.32 (1)	11.355	0.387(7)	20.95(2)	21.216
428	1.74 (2)	1.758	10.68 (1)	10.673	0.609(7)	19.07(3)	19.034
453	2.59 (2)	2.662	9.95 (2)	9.857	0.93 (1)	16.85(5)	16.336
478	3.68 (3)	3.889	9.01 (2)	8.770	1.39 (2)	14.01(8)	12.580

continued on next page

continued from previous page

T	p_σ^{sim}	p_σ^{exp}	ρ'_{sim}	ρ'_{exp}	ρ''_{sim}	$\Delta h_{\mathrm{v}}^{\mathrm{sim}}$	$\Delta h_{\mathrm{v}}^{\mathrm{exp}}$
K	MPa	MPa	mol/l	mol/l	mol/l	kJ/mol	kJ/mol
thiophene							
270	0.0009(1)	0.002	12.83 (2)	12.967	0.0004(1)	34.13(7)	35.956
285	0.0033(2)	0.005	12.62 (2)	12.763	0.0014(1)	33.46(6)	35.270
300	0.0101(8)	0.012	12.398(6)	12.555	0.0041(3)	32.72(2)	34.562
325	0.029 (2)	0.033	12.068(6)	12.199	0.0110(9)	31.67(2)	33.329
348	0.076 (5)	0.075	11.732(6)	11.859	0.027 (2)	30.59(2)	32.127
383	0.19 (3)	0.209	11.257(8)	11.315	0.063 (9)	29.06(2)	30.148
418	0.53 (2)	0.476	10.699(6)	10.728	0.166 (5)	27.02(2)	27.939
464	1.18 (2)	1.139	9.88 (1)	9.866	0.359 (6)	24.09(3)	24.532
493	1.94 (2)	1.813	9.33 (2)	9.238	0.599 (8)	21.76(5)	21.928
530	3.17 (2)	3.068	8.42 (3)	8.264	1.03 (1)	18.06(7)	17.653
551	4.20 (3)	4.031	7.86 (5)	7.530	1.46 (2)	15.2 (1)	14.240
hydrogen cyanide							
273	0.030(1)	0.035	26.21(3)	26.548	0.0141(4)	28.78(4)	27.778
295	0.078(3)	0.088	25.11(4)	25.354	0.035 (1)	27.30(4)	27.060
315	0.169(5)	0.180	24.01(5)	24.217	0.074 (2)	25.76(5)	26.336
358	0.66 (1)	0.640	21.52(8)	21.536	0.292 (6)	21.86(7)	24.451
388	1.43 (3)	1.326	19.52(7)	19.367	0.69 (1)	18.41(8)	22.697
406	2.09 (4)	1.966	17.9 (8)	17.859	1.08 (2)	16.0 (1)	21.323
420	2.69 (3)	2.626	16.3 (1)	16.504	1.44 (3)	14.1 (1)	19.953
430	3.43 (3)	3.207	15.5 (1)	15.373	2.05 (3)	12.1 (1)	18.690
435	3.70 (3)	3.538	14.0 (3)	14.726	2.31 (3)	10.7 (2)	17.909
acetonitrile							
270	0.0015(1)	0.003	19.71(1)	19.636	0.0007(1)	38.87(8)	34.302
300	0.0074(3)	0.013	18.90(2)	18.871	0.0032(1)	36.78(7)	32.952
327	0.029 (1)	0.040	18.20(3)	18.151	0.0112(6)	34.88(7)	31.641
360	0.088 (3)	0.119	17.25(2)	17.223	0.033 (1)	32.42(6)	29.886
400	0.294 (5)	0.352	16.05(2)	16.003	0.109 (2)	29.09(6)	27.459
420	0.51 (1)	0.558	15.47(4)	15.341	0.190 (4)	27.27(8)	26.078
436	0.76 (3)	0.782	14.78(1)	14.777	0.289 (9)	25.31(5)	24.866
450	1.00 (4)	1.032	14.25(2)	14.253	0.38 (1)	23.98(5)	23.705
464	1.27 (9)	1.341	13.65(3)	13.693	0.48 (3)	22.58(5)	22.427
490	2.08 (4)	2.101	12.42(3)	12.515	0.85 (2)	19.20(9)	19.603
505	2.69 (3)	2.673	11.52(5)	11.707	1.18 (2)	16.7 (1)	17.549
510	2.73 (5)	2.889	11.06(6)	11.405	1.16 (2)	16.5 (1)	16.753
518	3.14 (4)	3.263	10.37(7)	10.871	1.37 (2)	15.0 (1)	15.308

continued on next page

continued from previous page

T	p_σ^{sim}	p_σ^{exp}	ρ'_{sim}	ρ'_{exp}	ρ''_{sim}	$\Delta h_{\mathrm{v}}^{\mathrm{sim}}$	$\Delta h_{\mathrm{v}}^{\mathrm{exp}}$
K	MPa	MPa	mol/l	mol/l	mol/l	kJ/mol	kJ/mol
nitromethane							
290	0.001(1)	0.003	18.82(2)	18.669	0.0003(1)	44.05(4)	38.511
353	0.026(1)	0.050	17.25(2)	17.239	0.0092(4)	39.62(5)	35.812
390	0.105(3)	0.160	16.32(3)	16.331	0.035 (1)	36.78(7)	33.983
430	0.33 (1)	0.435	15.27(2)	15.270	0.107 (3)	33.47(5)	31.716
471	0.92 (2)	1.003	14.13(3)	14.058	0.301 (6)	29.29(8)	28.931
500	1.56 (2)	1.670	13.12(4)	13.083	0.525 (8)	25.98(9)	26.518
530	2.70 (4)	2.694	11.93(5)	11.899	0.99 (2)	21.5 (1)	23.347
560	4.09 (6)	4.211	10.4 (1)	10.345	1.64 (3)	16.7 (2)	18.696
ammonia (new model)							
240	0.13(1)	0.102	40.26(1)	40.032	0.0665(1)	24.12(1)	23.314
280	0.60(2)	0.551	36.98(2)	36.939	0.281 (1)	21.56(1)	21.073
315	1.65(4)	1.637	33.76(3)	33.848	0.744 (2)	18.96(2)	18.573
345	3.37(4)	3.457	30.45(4)	30.688	1.55 (1)	16.19(3)	15.795
363	5.22(5)	5.101	28.17(6)	28.368	2.56 (2)	13.93(5)	13.654
375	6.37(6)	6.485	26.18(7)	26.502	3.17 (3)	12.48(6)	11.891
385	7.88(5)	7.845	24.05(9)	24.608	4.27 (5)	10.49(9)	10.078
ethylene oxide							
235	0.010(3)	0.009	21.61(1)	21.54	0.00525(1)	27.33(1)	28.17
270	0.06 (1)	0.058	20.56(1)	20.54	0.02610(2)	25.85(1)	26.49
305	0.23 (1)	0.222	19.44(1)	19.45	0.1077 (2)	24.10(1)	24.62
340	0.61 (1)	0.627	18.21(1)	18.26	0.2380 (6)	22.25(1)	22.49
375	1.43 (2)	1.437	16.86(1)	16.89	0.554 (2)	19.83(2)	19.95
390	1.94 (2)	1.956	16.21(1)	16.23	0.752 (3)	18.64(2)	18.68
410	2.80 (2)	2.849	15.18(2)	15.24	1.110 (5)	16.76(3)	16.73
445	5.06 (3)	5.088	12.91(6)	12.92	2.27 (3)	12.2 (1)	11.91
R227ea							
205.7		0.006	10.278(3)	10.107			25.716
261.8	0.10(2)	0.125	9.133(4)	9.017	0.0467(1)	23.98(1)	22.022
280.5	0.24(2)	0.256	8.72 (1)	8.604	0.1140(3)	22.21(2)	20.553
299.2	0.42(2)	0.472	8.24 (1)	8.151	0.1897(5)	20.40(2)	18.888
317.9	0.79(2)	0.801	7.72 (1)	7.641	0.371 (1)	18.10(3)	16.939
327	1.02(2)	1.012	7.42 (1)	7.364	0.485 (2)	16.85(4)	15.841
336.6	1.33(2)	1.279	7.14 (2)	7.041	0.665 (5)	15.36(5)	14.528
344.1	1.55(2)	1.521	6.84 (2)	6.758	0.79 (1)	14.16(6)	13.348
355.3	1.85(2)	1.948	6.22 (2)	6.257	0.93 (1)	12.41(6)	11.174

Table B.2: VLE of the binary mixture R227ea + Ethanol at 283.13 and 343.13 K: present simulation data compared to experimental data on vapor pressure. The number in parentheses indicate the statistical uncertainty in the last digit.

T K	x_{R227ea} mol/mol	p MPa	p_{exp} MPa	y_{R227ea} mol/mol
283.15	0	0.003(1)	0.003	
	0.490	0.21 (2)	0.230	0.99 (1)
	0.785	0.23 (2)	0.256	0.985(4)
	1	0.26 (2)	0.280	
343.15	0	0.072(8)	0.073	
	0.056	0.32 (3)	0.322	0.66 (4)
	0.145	0.60 (4)	0.617	0.81 (3)
	0.274	0.79 (9)	0.886	0.88 (3)
	0.478	1.12 (4)	1.097	0.93 (1)
	0.668	1.19 (3)	1.222	0.94 (1)
	0.878	1.37 (2)	1.366	0.970(2)
	0.940	1.41 (3)	1.422	0.983(1)
	1	1.48 (3)	1.487	

Table B.3: Present simulation data on the VLE of the ternary mixture nitrogen + oxygen + argon at 120 K. The numbers in parentheses indicate the statistical uncertainty in the last digits.

x_{N2} mol/mol	x_{O2} mol/mol	x_{Ar} mol/mol	p MPa	y_{N2} mol/mol	y_{O2} mol/mol	y_{Ar} mol/mol
0.6193	0.2857	0.0950	1.92(1)	0.733(3)	0.197(2)	0.070(2)
0.6126	0.2365	0.1509	1.95(1)	0.728(3)	0.160(2)	0.112(2)

Table B.4: Dew point, vapor concentration enhancement factor g_W, and vapor pressure enhancement factor f_W of humid air: Present simulation data compared to experimental data from Koglbauer and Wendland [95] and correlation from Wylie and Fisher [231]. The numbers in parentheses indicate the statistical uncertainty in the last digits.

T	p	ρ	x_W	$g_{W,sim}$	g_W [95]	g_W [231]	$f_{W,sim}$	f_W [231]
K	MPa	mol/l	mol/mol					
TIP4P water model [85]								
333.15	2.0	0.7223(2)	0.0238(2)	1.02(6)	1.0648	1.050	1.05(7)	1.046
	5.0	1.7992(7)	0.0103(1)	1.10(7)	1.1642	1.122	1.13(8)	1.115
	10.0	3.557(1)	0.00594(8)	1.25(8)	1.3288	1.246	1.30(9)	1.227
	15.0	5.231(2)	0.00456(9)	1.42(10)	1.4897	1.377	1.51(11)	1.332
	20.0	6.799(3)	0.00403(7)	1.63(12)	1.6509		1.78(13)	
	22.5	7.538(3)	0.00373(8)	1.67(13)	1.7460		1.85(14)	
	25.0	8.239(3)	0.0040(1)	1.93(11)	1.8178		2.18(13)	
353.15	2.0	0.6814(2)	0.0529(4)	1.02(4)	1.0408	1.048	1.06(4)	1.038
	5.0	1.6925(6)	0.0232(2)	1.10(4)	1.1204	1.110	1.16(4)	1.094
	10.0	3.334(1)	0.0132(2)	1.24(5)	1.2312	1.217	1.33(5)	1.185
	15.0	4.899(2)	0.0105(2)	1.45(6)	1.3405	1.328	1.58(6)	1.268
	20.0	6.367(3)	0.0091(2)	1.64(7)	1.4590		1.83(8)	
	22.5	7.064(3)	0.0089(2)	1.78(9)	1.5178		2.02(10)	
	25.0	7.730(4)	0.0082(2)	1.79(9)	1.5752		2.06(10)	
water model of Schnabel [171]								
333.15	2.0	0.7219(2)	0.0075(1)	1.02(8)	1.0648	1.050	1.00(8)	1.046
	5.0	1.7983(5)	0.00333(4)	1.13(9)	1.1642	1.122	1.11(9)	1.115
	10.0	3.555(1)	0.00191(2)	1.28(10)	1.3288	1.246	1.27(10)	1.227
	15.0	5.226(2)	0.00144(2)	1.42(12)	1.4897	1.377	1.44(12)	1.332
	20.0	6.798(3)	0.00124(2)	1.59(13)	1.6509		1.65(14)	
	22.5	7.531(4)	0.00117(2)	1.66(14)	1.7460		1.76(14)	
	25.0	8.232(4)	0.00117(4)	1.82(18)	1.8178		1.95(19)	
353.15	2.0	0.6800(2)	0.0217(2)	1.01(6)	1.0408	1.048	1.03(6)	1.038
	5.0	1.6902(5)	0.0094(1)	1.08(7)	1.1204	1.110	1.12(7)	1.094
	10.0	3.330(1)	0.00538(7)	1.23(8)	1.2312	1.217	1.28(8)	1.185
	15.0	4.895(2)	0.00416(7)	1.39(9)	1.3405	1.328	1.49(9)	1.268
	20.0	6.361(3)	0.00358(8)	1.56(11)	1.4590		1.70(12)	
	22.5	7.050(4)	0.00338(8)	1.63(12)	1.5178		1.81(13)	
	25.0	7.720(4)	0.0034(1)	1.80(16)	1.5752		2.03(17)	

References

[1] Industrial Fluid Properties Simulation Collective. http://fluidproperties.org/.

[2] J. Ahrendts, H. D. Baehr. *Die thermodynamischen Eigenschaften von Ammoniak.* VDI-Forschungsheft Nr. 596, VDI-Verlag, Düsseldorf (1979).

[3] M. P. Allen, D. J. Tildesley. *Computer Simulation of Liquids.* Clarendon Press, Oxford (1987).

[4] H. E. Alper, F. Abu-Awwad, P. Politzer. Molecular dynamics simulations of liquid nitromethane. *J. Phys. Chem. B* **103** (1999) 9738–9742.

[5] H. C. Andersen. Molecular dynamics simulations at constant pressure and/or temperature. *J. Chem. Phys.* **72** (1980) 2384–2393.

[6] D. Berthelot. Sur le Mélange des Gaz. *Compt. Rend. Ac. Sc.* **126** (1898) 1703–1706.

[7] S. Bock, E. Bich, E. Vogel. A new intermolecular potential energy surface for carbon dioxide from ab initio calculations. *Chem. Phys.* **257** (2000) 147–156.

[8] E. Bourasseau, M. Haboudou, A. Boutin, A. H. Fuchs. New optimization method for intermolecular potentials: Optimization of a new anisotropic united atoms potential for olefins: Prediction of equilibrium properties. *J. Chem. Phys.* **118** (2003) 3020–3034.

[9] E. Bourasseau, P. Ungerer, A. Boutin. Prediction of equilibrium properties of cyclic alkanes by Monte Carlo simulation - new anisotropic united atoms intermolecular potential - new transfer bias method. *J. Phys. Chem. B* **106** (2002) 5483–5491.

[10] E. Bourasseau, P. Ungerer, A. Boutin, A. H. Fuchs. Monte Carlo simulation of branched alkanes and long chain n-alkanes with anisotropic united atoms intermolecular potential. *Mol. Sim.* **28** (2002) 317–336.

[11] S. W. Brelvi, J. P. O'Connell. Corresponding states correlations for liquid compressibility and partial molal volumes of gases at infinite dilution in liquids. *AIChE J.* **18** (1972) 1239–1243.

[12] C. M. Breneman, K. B. Wiberg. Determining atom-centered monopoles from molecular electrostatic potentials. The need for high sampling density in formamide conformational analysis. *J. Comput. Chem.* **11** (1990) 361–373.

[13] B. R. Brooks, R. E. Bruccoleri, B. D. Olafson, D. J. States, S. Swaminathan, M. Karplus. CHARMM: A program for molecular energy, minimization, and dynamics calculations. *J. Comp. Chem.* **4** (1983) 187–217.

[14] R. Car, M. Parrinello. Unified approach for molecular dynamics and density-functional theory. *Phys. Rev. Lett.* **55** (1985) 2471–2472.

[15] F. H. Case, J. Brennan, A. Chaka, K. D. Dobbs, D. G. Friend, D. Frurip, P. A. Gordon, J. Moore, R. D. Mountain, J. Olson, R. B. Ross, M. Schiller, V. K. Shen. The third industrial fluid properties simulation challenge. *Fluid Phase Equilib.* **260** (2007) 153–163.

[16] F. H. Case, J. Brennan, A. Chaka, K. D. Dobbs, D. G. Friend, P. A. Gordon, J. D. Moore, R. D. Mountain, J. D. Olson, R. B. Ross, M. Schiller, V. K. Shen, E. A. Stahlberg. The fourth industrial fluid properties simulation challenge. *Fluid Phase Equilib.* **274** (2008) 2–9.

[17] J. Chang, S. I. Sandler. Interatomic Lennard-Jones potentials of linear and branched alkanes calibrated by Gibbs ensemble simulations for vapor-liquid equilibria. *J. Chem. Phys.* **121** (2004) 7474–7483.

[18] E. Chiesi, F. Cavalieri, G. Paradossi. Supercooled water in PVA matrixes. II. A molecular dynamics study and comparison with QENS results. *J. Chem. Phys. B* **109** (2005) 8091–8096.

[19] L. E. Chirlian, M. Miller Francl. Atomic charges derived from electrostatic potentials: A detailed study. *J. Comput. Chem.* **8** (1987) 894–905.

[20] I. Cibulka, L. Hnědkovský, T. Tagaki. P-ρ-T data of liquids: Summarization and evaluation. 3. Ethers, ketones, aldehydes, carboxylic acids, and esters. *J. Chem. Eng. Data* **42** (1997) 2–26.

[21] P. Cieplak, J. Caldwell, P. A. Kollman. Molecular mechanical models for organic and biological systems going beyond the atom centered two body additive approximation: aqueous solution free energies of methanol and n-methylacetamide, nucleic acid base and amide hydrogen bonding and chloroform/water partition coefficients of the nucleic acid bases. *J. Comp. Chem.* **22** (2001) 1048–1057.

[22] W. D. Cornell, P. Cieplak, C. I. Bayly, I. R. Gould, K. M. Merz, D. M. Ferguson, D. C. Spellmeyer, T. Fox, J. W. Caldwell, P. A. Kollman. A second generation force field for the simulation of proteins, nucleic acids, and organic molecules. *J. Am. Chem. Soc.* **117** (1995) 5179–5197.

[23] T. E. Daubert. Vapor-liquid critical properties of elements and compounds. 5. Branched alkanes and cycloalkanes. *J. Eng. Chem. Data* **41** (1996) 365–372.

[24] S. De, N. Aluru, B. Johnson, W. Crone, D. Beebe, J. Moore. Equilibrium swelling and kinetics of pH-responsive hydrogels: models, experiments and simulations. *J. Microelectromech. Sci.* **11** (2002) 544–555.

[25] J. Delhommelle, C. Tschirwitz, P. Ungerer, G. Granucci, P. Millie, D. Pattou, A. H. Fuchs. Derivation of an optimized potential model for phase equilibria (OPPE) for sulfides and thiols. *J. Phys. Chem. B* **104** (2000) 4745–4753.

[26] M. T. Devanney. *Ethylene Oxide.* CEH Report, SRI Consulting, Menlo Park (2007).

[27] B. Eckl, Y.-L. Huang, J. Vrabec, H. Hasse. Vapor pressure of R227ea + ethanol at 343.13 K by molecular simulation. *Fluid Phase Equilib.* **260** (2007) 177–182.

[28] B. Eckl, T. Schnabel, J. Vrabec, M. Wendland, H. Hasse. Thermophysical properties of dry and humid air by molecular simulation including dew point calculations with the Mollier ensemble. *Ind. Eng. Chem. Res.* **48** (2009) 10 110–10 119.

[29] B. Eckl, J. Vrabec, H. Hasse. On the application of force fields for predicting a wide variety of properties: Ethylene oxide as an example. *Fluid Phase Equilib.* **274** (2008) 16–26.

[30] B. Eckl, J. Vrabec, H. Hasse. An optimised molecular model for ammonia. *Mol. Phys.* **106** (2008) 1039–1046.

[31] B. Eckl, J. Vrabec, H. Hasse. A set of molecular models based on quantum mechanical ab initio calculations and thermodynamic data. *J. Phys. Chem. B* **112** (2008) 12 710–12 721.

[32] R. Eggenberger, S. Gerber, H. Huber, M. Welker. A new ab initio potential for the neon dimer and its application in molecular dynamics simulations of the condensed phase. *Mol. Phys.* **82** (1994) 689–699.

[33] E. Ermakova, J. Solca, H. Huber, M. Welker. Argon in condensed phase: Quantitative calculations of structural, thermodynamic, and transport properties from pure theory. *J. Chem. Phys.* **102** (1995) 4942–4951.

[34] J. R. Errington, A. Z. Panagiotopoulos. A fixed point charge model for water optimized to the vapor-liquid coexistence properties. *J. Phys. Chem. B* **102** (1998) 7470–7475.

[35] J. R. Errington, A. Z. Panagiotopoulos. New intermolecular potential models for benzene and cyclohexane. *J. Chem. Phys.* **111** (1999) 9731–9738.

[36] F. A. Escobedo, J. J. de Pablo. Simulation and theory of the swelling of athermal gels. *J. Chem. Phys.* **106** (1997) 793–810.

[37] F. A. Escobedo. Novel pseudoensembles for simulation of multicomponent phase equilibria. *J. Chem. Phys.* **108** (1998) 8761–8772.

[38] F. A. Escobedo, J. J. de Pablo. Molecular simulation of polymeric networks and gels: phase behavior and swelling. *Phys. Rep.-Rev. Sec. Phys. Lett.* **318** (1999) 86–112.

[39] A. Eucken. Über das Wärmeleitvermögen, die spezifische Wärme und die innere Reibung der Gase. *Phys. Z.* **14** (1913) 324–332.

[40] D. J. Evans, W. B. Streett. Transport properties of homonuclear diatomics. 2. Dense fluids. *Mol. Phys.* **36** (1978) 161–176.

[41] R. Faller, H. Schmitz, O. Biermann, F. Müller-Plathe. Automatic parameterization of force fields for liquids by simplex optimization. *J. Comput. Chem.* **20** (1999) 1009–1017.

[42] G. A. Fernández, J. Vrabec, H. Hasse. A molecular simulation study of shear and bulk viscosity and thermal conductivity of simple real fluids. *Fluid Phase Equilib.* **221** (2004) 157–163.

[43] G. A. Fernández, J. Vrabec, H. Hasse. Self-diffusion and binary Maxwell-Stefan diffusion coefficients of quadrupolar real fluids from molecular simulation. *Int. J. Thermophys.* **26** (2005) 1389–1407.

[44] G. A. Fernández, J. Vrabec, H. Hasse. Shear viscosity and thermal conductivity of quadrupolar real fluids from molecular simulation. *Mol. Sim.* **31** (2005) 787–793.

[45] G. A. Fernández, J. Vrabec, H. Hasse. Shear viscosity and thermal conductivity of dipolar real fluids from equilibrium molecular dynamics simulation. *Cryogenics* **46** (2006) 711–717.

[46] G. A. Fernández, J. Vrabec, H. Hasse. Transport properties of anisotropic polar fluids: 1. Quadrupolar interaction. *Fluid Phase Equilib.* **249** (2006) 120–130.

[47] G. A. Fernández, J. Vrabec, H. Hasse. Transport properties of anisotropic polar fluids: 2. Dipolar interaction. *Fluid Phase Equilib.* **249** (2006) 131–139.

[48] D. Fincham, N. Quirke, D. J. Tildesley. Computer simulation of molecular liquid mixtures. 1. A diatomic Lennard-Jones model mixture for CO_2/C_2H_6. *J. Chem. Phys.* **84** (1986) 4535–4546.

[49] H. Flyvbjerg, H. G. Petersen. Error estimates on averages of correlated data. *J. Chem. Phys.* **91** (1989) 461–466.

[50] D. Frenkel, B. Smit. *Understanding Molecular Simulation: From Algorithms to Applications.* Academic Press, San Diego (2002).

[51] M. Frisch, G. Trucks, H. Schlegel, G. Scuseria, M. Robb, J. Cheeseman, J. Montgomery, Jr., T. Vreven, K. Kudin, J. Burant, J. Millam, S. Iyengar, J. Tomasi, V. Barone, B. Mennucci, M. Cossi, G. Scalmani, N. Rega, G. Petersson, H. Nakatsuji, M. Hada, M. Ehara, K. Toyota, R. Fukuda, J. Hasegawa, M. Ishida, T. Nakajima, Y. Honda, O. Kitao, H. Nakai, M. Klene, X. Li, J. Knox, H. Hratchian, J. Cross, V. Bakken, C. Adamo, J. Jaramillo, R. Gomperts, R. Stratmann, O. Yazyev, A. Austin, R. Cammi, C. Pomelli, J. Ochterski, P. Ayala, K. Morokuma, G. Voth, P. Salvador, J. Dannenberg, V. Zakrzewski, S. Dapprich, A. Daniels, M. Strain, O. Farkas, D. Malick, A. Rabuck, K. Raghavachari, J. Foresman, J. Ortiz, Q. Cui, A. Baboul, S. Clifford, J. Cioslowski, B. Stefanov, G. Liu, A. Liashenko, P. Piskorz, I. Komaromi, R. Martin, D. Fox, T. Keith, M. Al-Laham, C. Peng, A. Nanayakkara, M. Challacombe, P. Gill, B. Johnson, W. Chen, M. Wong, C. Gonzalez, J. Pople. *Gaussian 03.* Gaussian Inc., Wallingford, CT (2004).

[52] S. L. Garrison, S. I. Sandler. On the use of *ab initio* interaction energies for the accurate calculation of thermodynamic properties. *J. Chem. Phys.* **117** (2002) 10 571–10 580.

[53] S. L. Garrison, S. I. Sandler. An accurate acetylene intermolecular potential for phase behavior predictions from quantum chemistry. *J. Phys. Chem. B* **108** (2004) 18 972–18 979.

[54] S. L. Garrison, S. I. Sandler. A potential from quantum chemistry for thermodynamic property predictions for methanethiol. *J. Chem. Phys.* **123** (2005) 054 506.

[55] G. Gerlach, M. Günther, J. Sorber, G. Suchanek, K.-F. Arndt, A. Richter. Chemical and pH sensors based on the swelling behavior of hydrogels. *Sens. Actuators, B* **111–112** (2005) 555–561.

[56] P. A. Gordon, M. Schiller, C.-P. C. Kao, S. Bair, D. G. Friend. Benchmarks for the Third Industrial Fluid Properties Simulation Challenge. *Fluid Phase Equilib.* **260** (2007) 164–168.

[57] C. G. Gray, K. E. Gubbins. *Theory of Molecular Fluids. 1. Fundamentals.* Clarendon Press, Oxford (1984).

[58] M. S. Green. Markoff random processes and the statistical mechanics of time-dependent phenomena. 2. Irreversible processes in fluids. *J. Chem. Phys.* **22** (1954) 398–413.

[59] E. Guàrdia, R. Pinzón, J. Casulleras, M. Orozco, F. J. Luque. Comparison of different three-site interaction potentials for liquid acetonitrile. *Mol. Sim.* **26** (2001) 287–306.

[60] K. E. Gubbins. In K. Singer. *Statistical Mechanics, Vol. 1.* The Chemical Society, Burlington House, London (1973).

[61] L. Haar. Thermodynamic properties of ammonia. *J. Phys. Chem. Ref. Data* **7** (1978) 635–792.

[62] I. S. Han, M.-H. Han, J. Kim, S. Lew, Y. J. Lee, F. Horkay, J. J. Magda. Constant-volume hydrogel osmometer: A new device concept for miniature biosensors. *Biomacromol.* **3** (2002) 1271–1275.

[63] J. M. Hermida-Raón, M. A. Ríos. A new intermolecular polarizable potential for a formaldehyde dimer. Application to liquid simulations. *J. Phys. Chem. A* **102** (1998) 10 818–10 827.

[64] S. Herrmann, H.-J. Kretzschmar, V. Teske, E. Vogel, P. Ulbig, R. Span, D. Gatley. Determination of thermodynamic and transport properties of humid air for power-cycle calculations. *PTB Report* (2009).

[65] D. M. HEYES. Chemical potential, partial enthalpy and partial volume of mixtures by NpT molecular dynamics. *Mol. Sim.* **8** (1992) 227–238.

[66] A. HINCHLIFFE, D. G. BOUNDS, M. L. KLEIN, I. R. MCDONALD, R. RIGHINI. Intermolecular potentials for ammonia based on SCF-MO calculations. *J. Chem. Phys.* **74** (1981) 1211–1216.

[67] Y. HIROKAWA, T. TANAKA. Volume transition in a nonionic gel. *J. Chem. Phys.* **81** (1984) 6379–6380.

[68] J. O. HIRSCHFELDER, C. F. CURTISS, R. B. BIRD. *Molecular Theory of Gases and Liquids.* John Wiley & Sons, New York (1967).

[69] M. HLOUCHA, U. K. DEITERS. Monte Carlo simulations of acetonitrile with an anisotropic polarizable molecular model. *Mol. Phys.* **90** (1997) 593–597.

[70] M. HLOUCHA, A. K. SUM, S. I. SANDLER. Computer simulation of acetonitrile and methanol with ab initio-based pair potentials. *J. Chem. Phys.* **113** (2000) 5401–5406.

[71] Y.-L. HUANG, J. VRABEC, H. HASSE. Prediction of ternary vapor-liquid equilibria for 33 systems by molecular simulation. *Fluid Phase Equilib.* **287** (2009) 62–69.

[72] H. HUBER, A. DYSON, B. KIRCHNER. Calculation of bulk properties of liquids and supercritical fluids from pure theory. *Chem. Soc. Rev.* **28** (1999) 121–133.

[73] A. HÜTHER, G. MAURER. Swelling of n-isopropyl acrylamide hydrogels in aqueous solutions of poly(ethylene glycol). *Fluid Phase Equilib.* **226** (2004) 321–332.

[74] A. HÜTHER, B. SCHÄFER, X. XU, G. MAURER. Phase equilibria of hydrogel systems. *Phys. Chem. Chem. Phys.* **4** (2002) 835–844.

[75] R. W. HYLAND. Correlation of the second interaction virial coefficients and enhancement factors for moist air. *J. Res. Natl. Bur. Stand. A* **79** (1975) 551–560.

[76] R. W. HYLAND, A. WEXLER. The enhancement of water vapor in carbon dioxide-free air at 30, 40, and 50 °C. *J. Res. Natl. Bur. Stand. A* **77** (1973) 115–131.

[77] R. W. IMPEY, M. L. KLEIN. A simple intermolecular potential for liquid ammonia. *Chem. Phys. Lett.* **104** (1984) 579–582.

[78] J.-P. JALKANEN, R. MAHLANEN, T. A. PAKKANEN, R. L. ROWLEY. Ab initio potential energy surfaces of the propane dimer. *J. Chem. Phys.* **116** (2002) 1303–1312.

[79] J. Janeček. Long range corrections in inhomogeneous simulations. *J. Phys. Chem. B* **110** (2006) 6264–6269.

[80] J. R. Jones. The determination of molecular fields. (I) From the variation of the viscosity of a gas with temperature. *Proc. Roy. Soc. (London)* **106A** (1924) 441–462.

[81] J. R. Jones. The determination of molecular fields. (II) From the equation of state of a gas. *Proc. Roy. Soc. (London)* **106A** (1924) 463–477.

[82] W. L. Jorgensen. Transferable intermolecular potential functions for water, alcohols, and ethers: Application to liquid water. *J. Am. Chem. Soc.* **103** (1981) 335–340.

[83] W. L. Jorgensen. Intermolecular potential functions and Monte Carlo simulations for liquid sulfur compounds. *J. Phys. Chem.* **90** (1986) 6379–6388.

[84] W. L. Jorgensen, J. M. Briggs. Monte Carlo simulations of liquid acetonitrile with a three-site model. *Mol. Phys.* **63** (1988) 547–558.

[85] W. L. Jorgensen, J. D. Chandrasekhar, R. W. Madura, R. W. Impey, M. L. Klein. Comparison of simple potential functions for simulating liquid water. *J. Chem. Phys.* **79** (1983) 926–935.

[86] W. L. Jorgensen, M. Ibrahim. Structure and properties of liquid ammonia. *J. Amer. Chem. Soc.* **102** (1980) 3309–3315.

[87] W. L. Jorgensen, J. D. Madura, C. J. Swenson. Optimized intermolecular potential functions for liquid hydrocarbons. *J. Am. Chem. Soc.* **106** (1984) 6638–6646.

[88] W. L. Jorgensen, D. S. Maxwell, J. Tirado-Rives. Development and testing of the OPLS all-atom force field on conformational energetics and properties of organic liquids. *J. Am. Chem. Soc.* **118** (1996) 11 225–11 236.

[89] F. Juárez-Guerra, J. L. Rivera, A. Zúñiga Moreno, L. A. Galicia-Luna, J. L. Rico, J. Lara. Molecular modeling of thiophene in the vapor-liquid equilibrium. *Sep. Sci. Technol.* **41** (2006) 261–281.

[90] N. Kayaman, E. Hamurcu, N. Uyanik, B. Baysal. Interpenetrating hydrogel networks based on polyacrylamide and poly(itaconcid acid): synthesis and characterization. *Macromol. Chem. Phys.* **200** (1999) 231–238.

[91] M. H. Ketko, J. J. Potoff. Effect of partial charge parameterization on the phase equilibria of dimethyl ether. *Mol. Sim.* **22** (2007) 769–776.

[92] M. H. KETKO, J. RAFFERTY, J. I. SIEPMANN, J. J. POTOFF. Development of the TraPPE-UA force field for ethylene oxide. *Fluid Phase Equilib.* **274** (2008) 44–49.

[93] A. KLAMT. Conductor-like screening model for real solvents - a new approach to the quantitative calculation of solvation phenomena. *J. Phys. Chem.* **99** (1995) 2224–2235.

[94] G. KLINGENBERG, P. ULBIG. Isochoric $p\rho T$ measurements on dry and humid air. *J. Chem. Eng. Data* **52** (2007) 1413–1419.

[95] G. KOGLBAUER, M. WENDLAND. Water vapor concentration enhancement in compressed humid air measured by Fourier transform infrared spectroscopy. *J. Chem. Eng. Data* **52** (2007) 1672–1677.

[96] G. KOGLBAUER, M. WENDLAND. Water vapor concentration enhancement in compressed humid nitrogen, argon, and carbon dioxide measured by Fourier transform infrared spectroscopy. *J. Chem. Eng. Data* **53** (2008) 77–82.

[97] T. KRISTÓF, J. LISZI. Alternative implementations of the Gibbs ensemble Monte Carlo calculation. *Chem. Phys. Lett.* **261** (1996) 620–624.

[98] T. KRISTÓF, J. LISZI. Application of a new Gibbs ensemble Monte Carlo method to site-site interaction model fluids. *Mol. Phys.* **90** (1997) 1031–1034.

[99] T. KRISTÓF, J. VORHOLZ, J. LISZI, B. RUMPF, G. MAURER. A simple effective pair potential for the molecular simulation of the thermodynamic properties of ammonia. *Mol. Phys.* **97** (1999) 1129–1137.

[100] R. KUBO. Statistical-mechanical theory of irreversible processes. 1. General theory and simple applications to magnetic and conduction problems. *J. Phys. Soc. Jpn.* **12** (1957) 570–586.

[101] A. P. KUDCHADKER, G. H. ALANI, B. J. ZWOLINSKI. Critical constants of organic substances. *Chem. Rev.* **68** (1968) 659–735.

[102] A. P. KUDCHADKER, A. AMBROSE, C. TSONOPOULOS. Vapor-liquid critical properties of elements and compounds. 7. Oxygen compounds other than alkanols and cycloalkanols. *J. Chem. Eng. Data* **46** (2001) 457–479.

[103] O. KUNZ, R. KLIMEK, W. WAGNER, M. JASCHKE. *The GERG-2004 Wide-Range Reference Equation of State for Natural Gases and Other Mixtures.* Fortschr.-Ber. VDI Reihe 6 Nr. 557, VDI-Verlag, Düsseldorf (2004).

[104] A. R. LEACH. *Molecular Modeling. Principles and Application.* Prentice-Hall, Englewood Cliffs, 2nd edn. (2001).

[105] E. W. LEMMON, M. L. HUBER, M. O. MCLINDEN. REFPROP, NIST Standard Reference Database 23, Version 8.0. Physical and Chemical Properties Division, National Institute of Standards and Technology, Boulder (2006).

[106] E. W. LEMMON, R. T. JACOBSEN, S. G. PENONCELLO, D. G. FRIEND. Thermodynamic properties of air and mixtures of nitrogen, argon, and oxygen from 60 to 1000 K at pressures to 2000 MPa. *J. Phys. Chem. Ref. Data* **29** (2000) 331–385.

[107] K. LEONHARD, U. K. DEITERS. Monte Carlo simulations of nitrogen using an ab initio potential. *Mol. Phys.* **100** (2002) 2571–2585.

[108] H. LI, Z. YUAN, T. NG, H. LEE, K. LAM, Q. WANG, S. WU, J. FU, J. HANES. Constitutive model development and micro-structural topology optimisation for Nafion hydrogel membranes with ionic clustering. *J. Biomater. Sci. Poly. Edn.* **14** (2003) 1181–1196.

[109] X. LI, L. ZHAO, T. CHENG, L. LIU, H. SUN. One force field for predicting multiple thermodynamic properties of liquid and vapor ethylene oxide. *Fluid Phase Equilib.* **274** (2008) 36–43.

[110] B. LIN, J. W. HALLEY. Molecular dynamics model of dimethyl ether. *J. Phys. Chem.* **99** (1995) 16 474–16 478.

[111] M. LÍSAL, W. R. SMITH, I. NEZBEDA. Accurate vapour-liquid equilibrium calculations for complex systems using the reaction Gibbs Ensemble Monte Carlo simulation method. *Fluid Phase Equilib.* **181** (2001) 127–146.

[112] H. A. LORENTZ. Über die Anwendung des Satzes vom Virial in der kinetischen Theorie des Gase. *Ann. Phys.* **12** (1881) 127–136.

[113] A. LOTFI, J. VRABEC, J. FISCHER. Orthobaric densities from simulations of the liquid vapour interface. *Mol. Sim.* **5** (1990) 233–243.

[114] A. LOTFI, J. VRABEC, J. FISCHER. Vapour liquid equilibria of the Lennard-Jones fluid from the NpT plus test particle method. *Mol. Phys.* **76** (1992) 1319–1333.

[115] N. LUBNA, G. KAMATH, J. J. POTOFF, N. RAI, J. I. SIEPMANN. Transferable potentials for phase equilibria. 8. United-atoms description for thiols, sulfides, disulfides, and thiophene. *J. Phys. Chem. B* **109** (2005) 24 100–24 107.

[116] R. LUSTIG. Angle-average for the powers of the distance between two seperated vectors. *Mol. Phys.* **65** (1988) 175–179.

[117] R. LUSTIG. Personal communication (2002).

[118] A. MACKERELL, J. WIÓRKIEWICZ-KUCZERA, M. KARPLUS. An all-atom empirical energy function for the simulation of nucleic acids. *J. Am. Chem. Soc.* **117** (1995) 11 946–11 975.

[119] K. N. MARSH, C. L. YOUNG, D. W. MORTON, D. AMBROSE, C. TSONOPOULOS. Vapor-liquid critical properties of elements and compounds. 9. Organic compounds containing nitrogen. *J. Chem. Eng. Data* **51** (2006) 305–314.

[120] M. MARTIN. Comparison of the AMBER, CHARMM, COMPASS, GROMOS, OPLS, TraPPE and UFF force fields for prediction of vapor-liquid coexistence curves and liquid densities. *Fluid Phase Equilib.* **248** (2006) 50–55.

[121] M. MARTIN, J. SIEPMANN. Novel configurational-bias Monte Carlo method for branched molecules. Transferable potentials for phase equilibria. 2. United-atom description of branched alkanes. *J. Phys. Chem. B* **103** (1999) 4508–4517.

[122] M. G. MARTIN, J. I. SIEPMANN. Transferable potentials for phase equilibria. 1. United-atom description of n-alkanes. *J. Phys. Chem. B* **102** (1998) 2569–2577.

[123] J. F. MATHEWS. The critical constants of inorganic substances. *Chem. Rev.* **72** (1972) 71–100.

[124] J. E. MAYER. The statistical mechanics of condensing systems. I. *J. Chem. Phys.* **5** (1937) 67–73.

[125] J. E. MAYER. Statistical mechanics of condensing systems. V. Two-component systems. *J. Phys. Chem.* **43** (1939) 71–95.

[126] J. E. MAYER, M. G. MAYER. *Statistical Mechanics.* John Wiley and Sons, New York (1940).

[127] M. MECKE, J. FISCHER, J. WINKELMANN. Molecular dynamics simulation of the liquid-vapor interface of dipolar fluids under different electrostatic boundary conditions. *J. Chem. Phys.* **114** (2001) 5842–5852.

[128] M. MECKE, J. WINKELMANN, J. FISCHER. Molecular dynamics simulation of the liquid-vapor interface: The Lennard-Jones fluid. *J. Chem. Phys.* **107** (1997) 9264–9270.

[129] M. Mehta, D. A. Kofke. Coexistence diagrams of mixtures by molecular simulation. *Chem. Eng. Sci.* **49** (1994) 2633–2645.

[130] F.-A. Missenard. Methode additive pour la determination de la chaleur molaire des liquides. *Compt. Rend.* **260** (1965) 5521–5523.

[131] D. Möller, J. Fischer. Vapour liquid equilibrium of a pure fluid from test particle method in combination with NpT molecular dynamics simulation. *Mol. Phys.* **69** (1990) 463–473.

[132] D. Möller, J. Fischer. Vapour liquid equilibrium of a pure fluid from test particle method in combination with NpT molecular dynamics simulation. *Mol. Phys.* **75** (1992) 1461–1462.

[133] R. D. Mountain. A polarizable model for ethylene oxide. *J. Phys. Chem. B* **109** (2005) 13 352–13 355.

[134] T. J. Müller, S. Roy, W. Zhao, A. Maass, D. Reith. Economic simplex optimization for broad range property prediction: Strengths and weaknesses of an automated approach for tailoring of parameters. *Fluid Phase Equilib.* **274** (2008) 27–35.

[135] F. Müller-Plathe, W. van Gunsteren. Solvation of poly(vinyl alcohol) in water, ethanol and an equimolar water-ethanol mixture: structure and dynamics studied by molecular simulation. *Polymer* **38** (1997) 2259–2268.

[136] P. K. Naicker, A. K. Sum, S. I. Sandler. Ab initio potential and phase equilibria predictions for hydrogen chloride. *J. Chem. Phys.* **118** (2003) 4086–4093.

[137] G. B. Narinskii. Investigation of the vapor-liquid equilibrium in the system oxygen-argon-nitrogen. I. Experimental data. *Zh. Fiz. Khim.* **43** (1969) 408–412.

[138] M. S. Narkhede, B. Wang, J. L. Adcock, W. A. van Hook. Vapor pressures, liquid molar volumes, vapor non-ideality, and critical properties of some partially fluorinated ethers ($CF_3OCF_2CF_2H$, CF_3OCF_2H, and CF_3OCH_3), some perfluoroethers ($CF_3OCF_2OCF_3$, c-$CF_2OCF_2OCF_2$, and c-$CF_2CF_2CF_2O$), and of CHF_2Br and CF_3CFHCF_3. *J. Chem. Thermodyn.* **24** (1992) 1065–1075.

[139] A. H. Narten. Liquid-ammonia – molecular correlation-functions from X-ray-diffraction. *J. Chem. Phys.* **66** (1977) 3117–3120.

[140] A. E. Nasrabad, U. K. Deiters. Prediction of thermodynamic properties of krypton by Monte Carlo simulation using ab initio interaction potentials. *J. Chem. Phys.* **119** (2003) 947–952.

[141] A. E. Nasrabad, R. Laghaei, U. K. Deiters. Prediction of the thermophysical properties of pure neon, pure argon, and the binary mixtures neon-argon and argon-krypton by Monte Carlo simulation using ab initio potentials. *J. Chem. Phys.* **121** (2004) 6423–6434.

[142] S. K. Nath, J. J. de Pablo. Simulation of vapour-liquid equilibria for branched alkanes. *Mol. Phys.* **98** (2000) 231–238.

[143] P. Netz, T. Dorfmüller. Computer simulation studies of anomalous diffusion in gels: structural properties and probe-size dependence. *J. Chem. Phys.* **103** (1995) 9077–9082.

[144] P. Netz, T. Dorfmüller. Computer simulation studies of diffusion on gels: model structures. *J. Chem. Phys.* **107** (1997) 9221–9233.

[145] P. Netz, T. Dorfmüller. Computer simulation studies on the polymer-induced modification of water properties in polyacrylamide hydrogels. *J. Phys. Chem. B* **102** (1998) 4875–4886.

[146] B. Neubauer, A. Boutin, B. Tavitan, A. H. Fuchs. Gibbs ensemble simulations of vapour-liquid phase equilibria of cyclic alkanes. *Mol. Phys.* **97** (1999) 769–776.

[147] I. Nezbeda, J. Kolafa. A new version of the insertion particle method for determinig the chemical potential by Monte Carlo simulation. *Mol. Sim.* **5** (1991) 391–403.

[148] I. Nezbeda, J. Slovak. Can Lennard-Jones particles with four bonding sites realistically model water? *Chem. Phys. Lett.* **260** (1996) 336–340.

[149] A. M. Nikitin, A. P. Lyubartsev. New six-site acetonitrile model for simulations of liquid acetonitrile and its aqueous mixtures. *J. Comput. Chem.* **28** (2007) 2020–2026.

[150] C. Oldiges, T. Tönsing. Local structure and dynamic properties of molecules in anisotropic liquids extracted from molecular dynamics simulations. The case of acetonitrile in polyacrylamide hydrogels. *Phys. Chem. Chem. Phys.* **2** (2000) 5630–5639.

[151] C. Oldiges, T. Tönsing, K. Wittler. Molecular dynamics simulation of structural, mobility effects between dilute aqueous CH_3CN solution and crosslinked PAA. *Phys. Chem. Chem. Phys.* **4** (2002) 5135–5141.

[152] J. D. Olson, L. C. Wilson. Benchmarks for the fourth industrial fluid properties simulation challenge. *Fluid Phase Equilib.* **274** (2008) 10–15.

[153] C. Oostenbrink, A. Villa, A. E. Mark, W. F. V. Gunsteren. A biomolecular force field based on the free enthalpy of hydration and solvation: The GROMOS force-field parameter sets 53A5 and 53A6. *J. Comput. Chem.* **25** (2004) 1656–1676.

[154] A. Z. Panagiotopoulos. Direct determination of phase coexistence properties of fluids by Monte Carlo simulation in a new ensemble. *Mol. Phys.* **61** (1987) 813–826.

[155] A. Z. Panagiotopoulos, N. Quirke, M. Stapleton, D. J. Tildesley. Phase equilibria by simulation in the Gibbs ensemble. Alternative derivation, generalization, and application to mixture and membrane equilibria. *Mol. Phys.* **63** (1988) 527–545.

[156] G. Paradossi, E. Cavalieri, E. Chiessi, V. Ponassi, V. Martorana. Tailoring of physical and chemical properties of macro- and microhydrogels based on telechelic PVA. *Biomacromol.* **3** (2002) 1255–1262.

[157] J. Pérez-Pellitero, P. Ungerer, A. D. Mackie. An anisotropic united atoms (AUA) potential for thiophenes. *J. Phys. Chem. B* **111** (2007) 4460–4466.

[158] K. Plunkett, M. Kraft, Q. Yu, J. Moore. Swelling kinetics of disulfide cross-linked microgels. *Macromol.* **36** (2003) 3960–3966.

[159] F. Pollitzer, E. Strebel. Über den Einfluss indifferenter Gase auf die Sattdampfkonzentration von Flüssigkeiten. *Z. Phys. Chem.* **111** (1924) 768–785.

[160] A. Poncela, A. M. Rubio, J. J. Freire. Determination of the potential parameters of a site model from calculations of second virial coefficients of linear and branched alkanes. *Mol. Phys.* **91** (1997) 189–201.

[161] M. L. P. Price, D. Ostrovsky, W. L. Jorgensen. Gas-phase and liquid-state properties of esters, nitriles, and nitro compounds with the OPLS-AA force field. *J. Comput. Chem.* **22** (2001) 1340–1352.

[162] R. C. Reid, J. M. Prausnitz, T. K. Sherwood. *The Properties of Gases and Liquids.* McGraw-Hill, New York, 3rd edn. (1977).

[163] M. Ribeiro. Molecular Dynamics Simulation of Liquid Sulfur Dioxide. *J. Phys. Chem. B* **110** (2006) 8789–8797.

[164] M. Ricci, M. Nardone, F. Ricci, C. Andreani, A. Soper. Microscopic structure of low temperature liquid ammonia: A neutron diffraction experiment. *J. Chem. Phys.* **102** (1995) 7650–7655.

[165] R. L. Rowley, W. V. Wilding, J. L. Oscarson, Y. Yang, N. A. Zundel, T. E. Daubert, R. P. Danner. DIPPR® Data Compilation of Pure Compound Properties. Design Institute for Physical Properties, AIChE, New York (2006).

[166] J. S. Rowlinson, B. Widom. *Molecular Theory of Capillary.* Oxford University Press, New York (1982).

[167] R. Sadus. *Molecular Simulation of Fluids: Theory, Algorithms, and Object-Orientation.* Elsevier, Amsterdam (1999).

[168] S. I. Sandler, M. Castier. Computational quantum mechanics: An underutilized tool in thermodynamics. *Pure Appl. Chem.* **79** (2007) 1345–1359.

[169] C. Schauz. *Molekulare Simulation von Hydrogelen.* Diploma Thesis, University of Stuttgart (2007).

[170] M. W. Schmidt, K. K. Baldridge, J. A. Boatz, S. T. Elbert, M. S. Gordon, J. H. Jensen, S. Koseki, N. Matsunaga, K. A. Nguyen, S. Shujun, T. L. Windus, M. Dupuis, J. A. Montgomery. General atomic and molecular electronic structure system. *J. Comput. Chem.* **14** (1993) 1347–1363.

[171] T. Schnabel. *Molecular Modeling and Simulation of Hydrogen Bonding Pure Fluids and Mixtures.* Logos Verlag, Berlin (2008).

[172] T. Schnabel, M. Cortada, J. Vrabec, S. Lago, H. Hasse. Molecular model for formic acid adjusted to vapor-liquid equilibria. *Chem. Phys. Lett.* **435** (2007) 268–272.

[173] T. Schnabel, A. Srivastava, J. Vrabec, H. Hasse. Hydrogen bonding of methanol in supercritical CO_2: Comparison between ^{1}H-NMR spectroscopic data and molecular simulation results. *J. Phys. Chem. B* **111** (2007) 9871–9878.

[174] T. Schnabel, J. Vrabec, H. Hasse. Henry's law constants of methane, nitrogen, oxygen and carbon dioxide in ethanol from 273 to 498 K: Prediction from molecular simulation. *Fluid Phase Equilib.* **233** (2005) 134–143.

[175] T. Schnabel, J. Vrabec, H. Hasse. Unlike Lennard-Jones parameters for vapor-liquid equilibria. *J. Mol. Liq.* **135** (2007) 170–178.

[176] T. SCHNABEL, J. VRABEC, H. HASSE. Molecular simulation study of hydrogen bonding mixtures and new molecular models for mono- and dimethylamine. *Fluid Phase Equilib.* **263** (2008) 144–159.

[177] V. K. SHEN, R. D. MOUNTAIN, J. R. ERRINGTON. Comparative study of the effect of tail corrections on surface tension determined by molecular simulation. *J. Phys. Chem. B* **111** (2007) 6198–6207.

[178] S. V. SHEVKUNOV, A. A. MARTINOVSKII, P. N. VORONTSOV-VELYAMINOV. Calculation of the critical sizes and properties of microdrops using the Monte-Carlo method in a generalized ensemble. *High Temp. Phys. (USSR)* **26** (1988) 246–254.

[179] J. M. SMITH, H. C. VAN NESS, M. M. ABBOTT. *Introduction to chemical engineering thermodynamics.* McGraw-Hill, New York, 5th edn. (1996).

[180] F. SOKOLIC, Y. GUISSANI, B. GUILLOT. Computer simulation of liquid sulfur dioxide: comparison of model potentials. *J. Phys. Chem.* **89** (1985) 3023–3026.

[181] F. SOKOLIC, Y. GUISSANI, B. GUILLOT. Molecular dynamics simulations of thermodynamic and structural properties of liquid SO_2. *Mol. Phys.* **56** (1985) 239–253.

[182] D. C. SORESCU, B. M. RICE, D. L. THOMPSON. Molecular dynamics simulations of liquid nitromethane. *J. Phys. Chem. A* **105** (2001) 9336–9346.

[183] R. SPENCE, W. WILD. The vapour pressure curve of formaldehyde, and some related data. *J. Chem. Soc.* **1** (1935) 506–509.

[184] D. V. D. SPOEL, E. LINDAHL, B. HESS, G. GROENHOF, A. E. MARK, H. J. C. BERENDSEN. GROMACS: Fast, flexible, and free. *J. Comput. Chem.* **26** (2005) 1701–1718.

[185] W. A. STEELE. In H. J. M. HANLEY. *Transport phenomena in fluids.* Marcel Dekker, New York and London (1969).

[186] J. STOLL. *Molecular Models for the Prediction of Thermophysical Properties of Pure Fluids and Mixtures.* Fortschr.-Ber. VDI Reihe 3 Nr. 836, VDI-Verlag, Düsseldorf (2005).

[187] J. STOLL, J. VRABEC, H. HASSE. Comprehensive study of the vapour-liquid equilibria of the two-centre Lennard-Jones plus point dipole fluid. *Fluid Phase Equilib.* **209** (2003) 29–53.

[188] J. Stoll, J. Vrabec, H. Hasse. A set of molecular models for carbon monoxide and halogenated hydrocarbons. *J. Chem. Phys.* **119** (2003) 11 396–11 407.

[189] J. Stoll, J. Vrabec, H. Hasse. Vapor-liquid equilibria of mixtures containing nitrogen, oxygen, carbon dioxide, and ethane. *AIChE J.* **49** (2003) 2187–2198.

[190] J. Stoll, J. Vrabec, H. Hasse, J. Fischer. Comprehensive study of the vapour-liquid equilibria of the two-centre Lennard-Jones plus point quadrupole fluid. *Fluid Phase Equilib.* **179** (2001) 339–362.

[191] A. J. Stone, M. Alderton. Distributed multipole analysis. Methods and applications. *Mol. Phys.* **100** (2002) 221–233.

[192] J. M. Stubbs, J. J. Potoff, J. I. Siepmann. Transferable potentials for phase equilibria. 6. United-atom description for ethers, glycols, ketones, and aldehydes. *J. Phys. Chem. B* **108** (2004) 17 596–17 605.

[193] A. K. Sum, S. I.Sandler. Prediction of the phase behavior of acetonitril and methanol with ab initio pair potentials. I. Pure components. *J. Chem. Phys.* **116** (2002) 7627–7636.

[194] A. K. Sum, S. I. Sandler. Prediction of the phase behavior of acetonitril and methanol with ab initio pair potentials. II. The mixture. *J. Chem. Phys.* **116** (2002) 7637–7644.

[195] A. K. Sum, S. I. Sandler, P. K. Naicker. Ab initio potentials and phase equilibria predictions of halogenated compounds. *Fluid Phase Equilib.* **199** (2002) 5–13.

[196] H. Sun. COMPASS: An ab initio force-field optimized for condensed-phase applications — Overview with details on alkene and benzene compounds. *J. Phys. Chem. B* **102** (1998) 7338–7364.

[197] Y. Tamai, H. Tanaka. Molecular dynamic study of polymer-water interaction in hydrogels: 1. Hydrogen-bond structure. *Macromol.* **29** (1996) 6750–6760.

[198] Y. Tamai, H. Tanaka. Molecular dynamic study of polymer-water interaction in hydrogels: 2. Hydrogen-bond dynamics. *Macromol.* **29** (1996) 6761–6769.

[199] Y. Tamai, H. Tanaka. Molecular dynamic study of water in hydrogels. *Mol. Sim.* **16** (1996) 359–374.

[200] Y. Tamai, H. Tanaka. Dynamic properties of supercooled water in poly(vinyl alcohol) hydrogel. *Chem. Phys. Lett.* **285** (1998) 127–132.

[201] Y. Tamai, H. Tanaka. Structure and dynamics of poly(vinyl alcohol) hydrogel. *Mol. Sim.* **21** (1999) 283–301.

[202] R. Tillner-Roth, F. Harms-Watzenberg, H. D. Baehr. Eine neue Fundamentalgleichung für Ammoniak. *DKV-Tagungsbericht* **20** (1993) 167–181.

[203] B. Trout. *Car-Parinello Methods in Chemical Engineering: Their Scope and Potential.* Academic Press, San Diego (2001).

[204] C. Tsonopoulos, D. Ambrose. Vapor-liquid critical properties of elements and compounds. 8. Organic sulfur, silicon, and tin compounds (C+H+S, Si, and Sn). *J. Chem. Eng. Data* **46** (2001) 480–485.

[205] S. Tsuzuki, T. Uchimaru, M. Mikami, K. Tanabe. Intermolecular interaction potential of the carbon dioxide dimer. *J. Chem. Phys.* **109** (1998) 2169–2175.

[206] H. Ulrich. *Raw Materials for Industrial Polymers.* Hanser, München (1988).

[207] P. Ungerer, A. Boutin, A. H. Fuchs. Direct calculation of bubble points by Monte Carlo simulation. *Mol. Phys.* **97** (1999) 523–539.

[208] P. Ungerer, J. Delhommelle, A. Boutin, B. Rousseau, A. H. Fuchs. Optimization of the anisotropic united atoms intermolecular potential for n-alkanes. *J. Chem. Phys.* **112** (2000) 5499–5510.

[209] M. Venkatraj, C. Bratschi, H. Huber, R. J. Gdanitz. Monte Carlo simulations of vapor-liquid equilibria of neon using an accurate ab initio pair potential. *Fluid Phase Equilib.* **218** (2004) 285–289.

[210] P. S. Vogt, R. Liapine, B. Kirchner, A. Dyson, H. Huber, G. Marcelli, R. J. Sadus. Molecular simulation of the vapour-liquid coexistence of neon and argon using ab inito potentials. *Phys. Chem. Chem. Phys.* **3** (2001) 1297–1302.

[211] J. Vrabec, J. Fischer. Vapor-liquid equilibria of the ternary mixture CH_4+C_2H_6+CO_2 from molecular simulation. *AIChE J.* **43** (1996) 212–217.

[212] J. Vrabec, H. Hasse. Grand Equilibrium: vapour-liquid equilibria by a new molecular simulation method. *Mol. Phys.* **100** (2002) 3375–3383.

[213] J. Vrabec, Y.-L. Huang, H. Hasse. Molecular models for 267 binary mixtures validated by vapor-liquid equilibria: a systematic approach. *Fluid Phase Equilib.* **279** (2009) 120–135.

[214] J. Vrabec, G. K. Kedia, U. Buchhauser, R. Meyer-Pittroff, H. Hasse. Thermodynamic models for vapor-liquid equilibria of nitrogen+oxygen+carbon dioxide at low temperatures. *Cryogenics* **49** (2009) 72–79.

[215] J. VRABEC, G. K. KEDIA, G. FUCHS, H. HASSE. Comprehensive study on vapour-liquid coexistence of the truncated and shifted Lennard-Jones fluid including planar and spherical interface properties. *Mol. Phys.* **104** (2006) 1509–1527.

[216] J. VRABEC, G. K. KEDIA, H. HASSE. Prediction of Joule-Thomson inversion curves for pure fluids and one mixture by molecular simulation. *Cryogenics* **45** (2005) 253–258.

[217] J. VRABEC, M. KETTLER, H. HASSE. Chemical potential of quadrupolar two-centre Lennard-Jones fluids by gradual insertion. *Chem. Phys. Lett.* **356** (2002) 431–436.

[218] J. VRABEC, A. KUMAR, H. HASSE. Joule-Thomson inversion curves of mixtures by molecular simulation in comparison to advanced equations of state: natural gas as an example. *Fluid Phase Equilib.* **258** (2007) 34–40.

[219] J. VRABEC, J. STOLL, H. HASSE. A set of molecular models for symmetric quadrupolar fluids. *J. Phys. Chem. B* **105** (2001) 12 126–12 133.

[220] J. VRABEC, J. STOLL, H. HASSE. Molecular models of unlike interactions in fluid mixtures. *Mol. Sim.* **31** (2005) 215–221.

[221] K. WATANABE. *Guideline on the Henry's Constant and Vapor-Liquid Distribution Constant for Gases in H_2O and D_2O at High Temperatures.* The International Association for the Properties of Water and Steam, Kyoto (2004).

[222] T. J. WEBSTER. The effect on water pressure of superimposed air pressure. *J. Soc. Chem. Ind.* **69** (1950) 343–346.

[223] S. WEINER, P. KOLLMAN, D. NGUYEN, D. CASE. An all atom force field for simulations of proteins and nucleic acids. *J. Comp. Chem.* **7** (1986) 230–252.

[224] M. WELKER, G. STEINEBRUNNER, J. SOLCA, H. HUBER. Ab initio calculation of the intermolecular potential energy surface of $(CO_2)_2$ and first applications in simulations of fluid CO_2. *Chem. Phys.* **213** (1996) 253–261.

[225] M. WENDLAND, G. KOGLBAUER. Need of thermophysical data for the design and optimization of thermal processes. In: G. G. M. STOFFELS, T. H. VAN DER MEER, A. A. VAN STEENHOVEN (Eds.). *Proceedings 5th European Thermal-Sciences Conference.* Eindhoven (2008).

[226] J. T. WESCOTT, P. KUNG, S. K. NATH. Vapour-liquid coexistence properties and critical points of two branched alkanes series. *Fluid Phase Equilib.* **208** (2003) 123–139.

[227] C. D. WICK, J. M. STUBBS, N. RAI, J. I. SIEPMANN. Transferable potentials for phase equilibria. 7. Primary, secondary, and tertiary amines, nitroalkanes and nitrobenzene, nitriles, amides, pyridine, and pyrimidine. *J. Phys. Chem. B* **109** (2005) 18 974–18 982.

[228] B. WIDOM. Some topics in the theory of fluids. *J. Chem. Phys.* **39** (1963) 2808–2812.

[229] B. WIDOM. Potential distribution theory and the statistical mechanics of fluids. *J. Phys. Chem. B* **86** (1982) 869–872.

[230] P. A. WIELOPOLSKI, E. R. SMITH. Molecular-dynamics studies of dielectric behavior and orientational correlations of liquid ethylene-oxide. *Mol. Phys.* **54** (1985) 467–478.

[231] R. G. WYLIE, R. S. FISHER. Molecular interaction of water vapor and air. *J. Chem. Eng.* **41** (1996) 133–142.

[232] J. YANG, Y. REN, A.-M. TIAN, H. SUN. COMPASS force field for 14 inorganic molecules, He, Ne, Ar, Kr, Xe, H_2, O_2, N_2, NO, CO, CO_2, NO_2, CS_2, and SO_2, in liquid phases. *J. Phys. Chem. B* **104** (2000) 4951–4957.

Die Reihen der Fortschritt-Berichte VDI:

1 Konstruktionstechnik / Maschinenbau
2 Fertigungstechnik
3 Verfahrenstechnik
4 Bauingenieurwesen
5 Grund- und Werkstoffe / Kunststoffe
6 Energietechnik
7 Strömungstechnik
8 Mess-, Steuerungs- und Regelungstechnik
9 Elektronik/Mikro- und Nanotechnik
10 Informatik / Kommunikation
11 Schwingungstechnik
12 Verkehrstechnik / Fahrzeugtechnik
13 Fördertechnik / Logistik
14 Landtechnik / Lebensmitteltechnik
15 Umwelttechnik
16 Technik und Wirtschaft
17 Biotechnik / Medizintechnik
18 Mechanik / Bruchmechanik
19 Wärmetechnik / Kältetechnik
20 Rechnerunterstützte Verfahren (CAD, CAM, CAE CAQ, CIM ...)
21 Elektrotechnik
22 Mensch-Maschine-Systeme

ISBN 978-3-18-391203-2